Antarctic glacial history inferred from cosmogenic-nuclide measurements in rocks

Perry Spector

A dissertation
submitted in partial fulfillment of the
requirements for the degree of

Doctor of Philosophy

University of Washington

2018

Reading Committee:

John Stone, Chair

Howard Conway

Bernard Hallet

Program Authorized to Offer Degree:

Earth and Space Sciences

University of Washington

Abstract

Antarctic glacial history inferred from cosmogenic-nuclide measurements in rocks

Perry Spector

Chair of the Supervisory Committee:
Dr. John Stone
Earth and Space Sciences

This dissertation describes three research projects on the glacial history of Antarctica using measurements of cosmogenic-nuclides in glacial deposits and bedrock surfaces.

The first chapter investigates the deglaciation chronology of the Ross Sea following the last ice age. Abrupt thinning of glaciers in the southern Transantarctic Mountains occurred ~9-8 kyr B.P. This coincided with deglaciation of the Scott Coast, ~800 km to the north. At the end of this period the grounding line was located near Shackleton Glacier, indicating that most of the central and western Ross Sea deglaciated in less than 2 kyr. The rapidity of this event appears to have been influenced by unstable grounding-line retreat into deep marine basins and, potentially, enhanced melting at the marine margin. Because the majority of the deglaciation occurred during the early Holocene, the Ross Sea sector could not have significantly contributed or responded to rapid sea-level rise during Meltwater Pulse 1A.

The second chapter discusses sites in West Antarctica for subglacial drilling to test for past ice-sheet collapse. It has been hypothesized that marine-based portions of the WAIS deglaciated during past warm interglacial periods. Measurements of cosmogenic nuclides in subglacial bedrock surfaces therefore have the potential to establish whether and when this

occurred. However, because most of the bedrock revealed by ice-sheet collapse would remain below sea level, shielded from the cosmic-ray flux, drill sites for subglacial sampling must be located in areas where thinning of the residual ice sheet would expose presently subglacial bedrock surfaces. In this chapter I discuss the criteria and considerations for choosing drill sites where subglacial samples will provide maximum information about WAIS extent during past interglacial periods. I evaluate candidate sites in West Antarctica and find that sites located adjacent to the large marine basins of West Antarctica will be most diagnostic of past ice-sheet collapse. There are important considerations for drill-site selection on the kilometer scale that can only be assessed by field reconnaissance. As a case study of these considerations, I describe reconnaissance at sites in West Antarctica, focusing on the Pirrit Hills, where in the summer of 2016-2017, an 8 m bedrock core was retrieved from below 150 m of ice.

The third chapter investigates the glacial history of three isolated groups of nunataks in West Antarctica. The objectives of this chapter are to examine (i) the development and preservation of alpine landscapes, and (ii) past variations in ice thickness on timescales ranging from thousands to millions of years. Alpine landscapes were carved during the mid-Miocene and have since remained exceptionally well preserved. A trimline at the Pirrit Hills is an extension of a prominent trimline that occurs throughout the Ellsworth Mountains to the north. At the divide, ice levels have rarely, if ever, been higher than present, but they appear to have been lower for prolonged periods in the past. Midway between the divide and the grounding line, ice levels have repeatedly been ~300-400 m higher than present, as occurred during the last ice age. Ice levels here also appear to have been lower than present during past interglacial periods.

TABLE OF CONTENTS

LIST OF FIGURES

LIST OF TABLES

Table Number Page

ACKNOWLEDGMENTS

Numerous individuals and organizations have supported this research over the past 8 years. I thank my advisor, John Stone, for his guidance, support, and camaraderie, both in Antarctica and in Seattle. I owe many thanks to my committee, Twit Conway, Bernard Hallet, and Paul Quay for their advice and for helpful discussions. I also thank Greg Balco, David Pollard, Christine Siddoway, Brenda Hall, Cameron Lewis, Maurice Conway, and Seth Campbell for their support in various aspects of this research.

I am grateful for my fellow grad students, past and present, who have been a source of friendship and learning. I am indebted to the members of the Colorado College Geology Dept. for giving me the opportunity to teach there during the course of my PhD. I thank Danielle Lemmon, Mika Usher, Taryn Black, Jessica Badgeley, and Michael Weyna for help in the lab and the field. I acknowledge financial support from the National Science Foundation Graduate Research Fellowship Program and the UW Dept. of Earth and Space Sciences.

Finally, thanks to my friends and family, and, in particular, Jess.

Chapter 1

INTRODUCTION

The motivation for this research comes from several aspects of Antarctic glacial history where our knowledge is deficient. One controversy is the source of Meltwater Pulse 1A, a ∼9-20 m rise in global mean sea level that occurred ∼14.6 kyr B.P. in a time period of a few hundred years. Attempts to infer the origin of this meltwater from coastal sea-level records suggest that Antarctica was a large contributor [e.g. Clark et al., 2002]. However, most geological and glaciological studies from Antarctica find no evidence for significant ice loss at this time [Bentley et al., 2014, and references therein]. This debate has persisted, in part due to insufficient chronological constraints on Antarctic deglaciation. One of the most important areas is the large Ross embayment, which was filled with grounded ice to near the continental shelf edge during the last ice age. Most constraints in the Ross Sea region are limited to the seafloor north of the modern ice shelf and sites along the NW coast. As a result, the timing and pattern of grounding-line retreat in large areas of this embayment are minimally constrained.

A second question is whether large-scale deglaciation (so-called "collapse") occurred in West Antarctica during warm periods of the past. Theoretical work shows that the West Antarctic Ice Sheet (WAIS) is vulnerable to collapse because it overlies deep marine basins in a configuration that facilitates runaway grounding-line retreat [Weertman, 1974; Schoof, 2007]. Increasing ice loss is presently occurring in the Amundsen Sea sector of the WAIS, and ice-sheet models suggest that an incipient collapse may be underway [e.g. Joughin et al., 2014]. Knowledge of whether and under what climate conditions the WAIS deglaciated in the past would be invaluable for understanding its present and future stability. There are several lines of evidence which collectively suggest that the WAIS has been smaller than present within the past ~1 Myr [see reviews in Dutton et al., 2015; Alley et al., 2015]. However, much of this evidence is indirect, inferential, or poorly dated, precluding robust estimates of the timing and magnitude of past deglaciations.

A third area in which we have limited knowledge is the history of the WAIS prior to the last ice age. Direct evidence of former ice thickness and extent is scarce because much of it has either been erased by subsequent glaciations or remains concealed below the present-day ice sheet. As a result, our understanding of earlier ice-sheet configurations is largely derived from paleoclimate records and ice-sheet models forced by these records [e.g. Pollard and DeConto, 2009]. Although these reconstructions provide plausible depictions of ice-sheet evolution, they have little meaning unless they can be shown to agree with observations of past ice-sheet change.

Chapter 2 addresses the first question by describing deglaciation records from southern Transantarctic Mountain glaciers, which delivered ice to the central Ross Sea. Abrupt thinning of these glaciers in the early Holocene coincided with deglaciation of the Scott Coast, ~800 km to the north, and ended with the Ross Sea grounding line near Shackleton Glacier. This deglaciation removed grounded ice from most of the central and western Ross Sea in less than 2 kyr. This occurred thousands of years after Meltwater Pulse 1A, demonstrating that the Ross Sea sector did not significantly contribute to sea-level rise at that time.

Chapter 3 does not answer the question of whether the WAIS collapsed in the past, but it lays out a framework for how to address this question by measuring cosmogenic nuclides in subglacial bedrock surfaces. Cosmogenic-nuclide concentrations in a bedrock core retrieved from below the full thickness of the Greenland Ice Sheet require periods of prolonged exposure during the Pleistocene when the ice sheet was largely absent [Nishiizumi, 1996; Schaefer et al., 2016]. In contrast, bedrock from below thick portions of the WAIS would not be capable of providing equivalent information because the bed in these areas is located far below sea level and would remain submerged, shielded from the cosmic-ray flux, if the ice sheet collapsed. Establishing whether the marine-based portions of the WAIS disappeared in the past will therefore require drilling through adjacent thinner portions of the ice sheet into subglacial highlands that would be exposed by ice thinning during collapse events. Chapter 3 discusses the criteria and considerations for choosing drill sites where subglacial samples will provide maximum information about WAIS extent during past interglacial periods. I evaluate candidate sites in West Antarctica, and find that sites located adjacent to the large marine basins of West Antarctica will be most diagnostic of past ice-sheet collapse.

Chapter 4 addresses the third question by providing direct observational constraints on the configuration of the WAIS prior to the last ice age. I present glacial-geologic observations and cosmogenic-nuclide measurements from three isolated groups of nunataks in West Antarctica. These sites lie along an approximate flowline running from the divide to midway down the flank of the ice sheet, allowing ice-thickness changes along this transect to be compared. Because these sites are located at high altitudes in areas of slow-flowing ice, bedrock surfaces have remained exceptionally well preserved for hundreds of thousands, and in many cases millions, of years. As a result cosmogenic-nuclide measurements on these surfaces provide information about the long-term history of exposure and ice cover. Ice levels at the divide have rarely, if ever, been higher than present in the past several million years. They have, however, been lower for prolonged intervals, likely during Pleistocene glacial periods as well as times prior to the Pleistocene. Midway between the divide and the grounding line, ice levels have repeatedly been $\sim$300-400 m higher than present, as occurred during the last ice age. Ice levels here have likely been lower than present during Pleistocene interglacial periods.

Chapter 2

RAPID EARLY-HOLOCENE DEGLACIATION IN THE ROSS SEA, ANTARCTICA

Perry Spector, John Stone, Seth G. Cowdery, Brenda Hall,
Howard Conway, and Gordon Bromley

Originally published in Geophysical Research Letters

ABSTRACT

Deglaciation of the Ross Sea following the last ice age provides an important opportunity to examine the stability of marine ice sheets and their susceptibility to changing environmental conditions. Insufficient chronology for Ross Sea deglaciation has helped sustain (i) the theory that this region contributed significantly to Meltwater Pulse 1A (MWP-1A) and (ii) the idea that Ross Sea grounding-line retreat occurred in a "swinging gate" pattern hinged north of Roosevelt Island. We present deglaciation records from southern Transantarctic Mountain glaciers, which delivered ice to the central Ross Sea. Abrupt thinning of these glaciers 9 - 8 kyr B.P. coincided with deglaciation of the Scott Coast, ~800 km to the north, and ended with the Ross Sea grounding line near Shackleton Glacier. This deglaciation removed grounded ice from most of the central and western Ross Sea in less than 2 kyr. The Ross Sea Sector neither contributed nor responded significantly to MWP-1A.

2.1 Introduction

The West Antarctic Ice Sheet (WAIS) is regarded as vulnerable to unstable retreat because much of it rests below sea level on a bed that deepens inland [Weertman, 1974; Schoof, 2007].

The ice sheet likely collapsed during at least one Pleistocene interglacial period [Scherer et al., 1998], and an incipient collapse may be underway in the Amundsen Sector [Joughin et al., 2014; Rignot et al., 2014]. This potential instability emphasizes the importance of understanding how marine ice sheets receded in the past. The Antarctic Ice Sheet has been identified as a significant source of Meltwater Pulse 1A (MWP-1A), [e.g. Clark et al., 2002], an abrupt ∼9 - 20 m eustatic sea-level rise 14.6 kyr before present (BP) [Liu et al., 2016; Lambeck et al., 2014; Deschamps et al., 2012; Peltier et al., 2015]. Attention has turned to the large Ross and Weddell marine embayments as possible Antarctic source areas; however, most geological and glaciological studies argue against a large Antarctic contribution from either sector [Bentley et al., 2014, and references therein]. In the case of the Ross Sea, most chronological constraints come from the seafloor north of the Ross Ice Shelf and deposits along the NW coast (Figure 2.1), leaving the deglacial history of the southern Ross Embayment largely unknown.

An enduring paradigm of Ross Sea deglaciation is the “swinging gate” model, in which the grounding line retreated along the Transantarctic Mountains while hinged north of Roosevelt Island (Figure 2.1) until ∼3 kyr B.P. [Stuiver, 1981; Conway et al., 1999; Martín et al., 2006]. This depiction arose primarily from constraints in the western Ross Embayment north of Hatherton Glacier (Figure 2.1). Detailed seafloor mapping has since revealed geomorphic evidence for a complex recession north of the modern ice shelf, in which periods of grounding-line stability were interrupted by episodes of rapid retreat [Anderson et al., 2014; Halberstadt et al., 2016]. Although attempts to date the retreat in the central and eastern Ross Sea have been inconclusive [Anderson et al., 2014], retreat ages in the western Ross Sea show that final deglaciation of the Scott Coast region occurred ∼8.6 - 7 kyr B.P. (see section 2.4.3).

Here we present deglaciation records based on ^{10}Be exposure ages of glacial deposits for Beardmore, Shackleton, and Scott Glaciers in the southern Transantarctic Mountains (Figure 2.1). We show that the grounding line had reached the mouths of Beardmore and Shackleton Glaciers by ∼8 kyr B.P. (Figure 2.1). Combined with previously published constraints from the Scott Coast region, the data demonstrate that most of the central and western Ross Sea became ice free in an episode of rapid grounding-line retreat in the early Holocene.

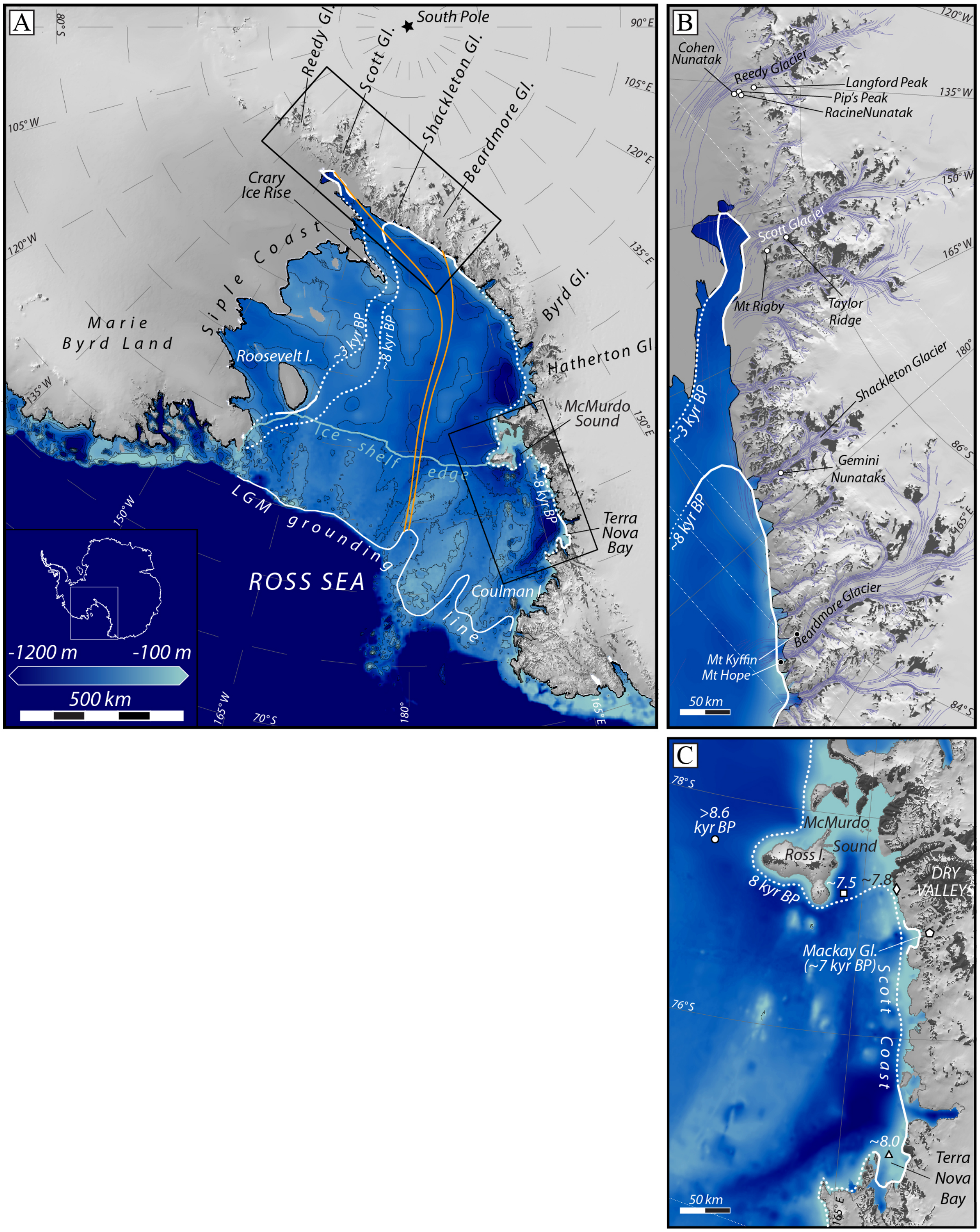

Figure 2.1: See caption on next page.

Figure 2.1: (a) The Ross Sector of Antarctica, showing rock and ice surfaces [Liu et al., 2001] and marine bathymetry [Fretwell et al., 2013]. Black rectangles show the locations of (b) a map of the southern Transantarctic Mountains and our field sites and (c) a map of the Scott Coast region. Orange lines represent inferred locations of flowlines from Scott and Beardmore Glaciers. These flowlines are schematic and are drawn to obey the provenance of till near the LGM grounding line [Licht et al., 2014]. The LGM grounding line is from Halberstadt et al. [2016]. In Figures 2.1a-c, white contours (solid where constrained by observations; dotted where inferred) represent the grounding-line chronology based on results presented here from the southern Transantarctic Mountains, from Roosevelt Island [Conway et al., 1999; Martín et al., 2006], and from the Scott Coast region. Because Crary Ice Rise is thought to have regrounded ∼1.1 kyr B.P. [Bindschadler et al., 1990], the grounding line may have been inboard of this location during the late Holocene. In the Scott Coast region (Figure 2.1c), the timing of final deglaciation is constrained by the following studies: Baroni and Hall [2004] (diamond), Hall et al. [2004] (triangle), Jones et al. [2015] (pentagon), Licht et al. [1996] (square), and McKay et al. [2016] (circle).

2.2 Field sites and methods

Beardmore, Shackleton, and Scott Glaciers flow through the southern Transantarctic Mountains and deliver ice to the central Ross Sea. Provenance studies indicate a similar flow pattern during the last ice age [Anderson et al., 2014; Licht et al., 2005, 2014; Farmer et al., 2006]. These glaciers transported rocks quarried upstream to ablation zones along their margins in the Transantarctic Mountains, depositing small lateral moraines and thin debris sheets during the glacial maximum and scattered erratics during deglaciation (Figures 2.4 - 2.12).

We sampled deposits on Taylor Ridge and Mount Kyffin (Figures 2.1b, 2.6, and 2.12) that mark the maximum ice age thickness of the lower reaches of Scott and Beardmore Glaciers, respectively. At the mouths of these glaciers, Mount Rigby and Mount Hope were both overrun during the glacial maximum but their summits emerged early in the deglaciation. We collected elevation transects of lightly weathered glacial erratics on these mountains to chronicle Ross Sea deglaciation at the mouths of Scott and Beardmore Glaciers (Figures 2.4 and 2.9). We found no fresh glacial deposits on mountains at the mouth of Shackleton Glacier, but we sampled a short elevation transect of fresh erratics from Gemini Nunataks, a pair of small peaks ~25 km upstream from the glacier mouth (Figure 2.8). The low relief of this site (~50 m) only constrains the final thinning of Shackleton Glacier.

For rock freshly eroded from the glacier bed, transported to the surface, and stranded by thinning ice, the subsequent buildup of cosmic ray-produced ^{10}Be records the time since initial exposure in the ablation zone. Details of the exposure-dating technique are described in the supporting information. Localized ablation zones are found on Antarctic glaciers, commonly in areas exposed to descending and warming katabatic winds. Ablation in these areas brings englacial debris to the glacier surface and ultimately results in deposition. During times when the glacier surfaces were stable or changing slowly, such as the Last Glacial Maximum (LGM), cobbles may have been exposed hundreds or thousands of years before physical deposition on bedrock [Ackert Jr et al., 2011]. In this case, exposure ages from a deposit are likely to span the period of stable ice thickness rather than date their final deposition. At times of rapid thinning, predepositional exposure is unlikely to be more than a few hundred years, less than the uncertainty of the exposure age.

Potential exposure-dating complications in Antarctica include shielding by snow cover, post-depositional disturbance by periglacial processes, and recycling of rock from older deposits. To avoid disturbance and snow cover, we sampled isolated erratics resting directly on windswept bedrock surfaces or on the surface of older, consolidated glacial deposits. To minimize the effect of recycling and prior exposure, we sampled only fresh, glacially worked erratics. Nonetheless, our samples include several rocks with substantially older exposure ages than other rocks collected nearby (Figure 2.2). In such cases, because we can eliminate the possibility of postdepositional erosion, disturbance, and cover by snow or till, we interpret the younger age as dating deposition and the older apparent age as the result of prior exposure. With allowance for these few cases of prior exposure and recycling, transects at all three sites show monotonically decreasing exposure ages with decreasing altitude (Figure 2.2).

Beryllium-10 production rates by spallation are based on the global calibration data set by Borchers et al. [2016], adjusted for altitude and latitude using the scaling scheme by Lal

[1991] and the relationship between Antarctic air pressure and elevation [Stone, 2000]. Some recent production rate calibrations suggest lower values than that of Borchers et al. [2016]. Using other combinations of high-latitude calibration data sets and scaling schemes would increase exposure ages by 1 - 6%, which would not substantially affect the findings of this research.

2.3 Results

2.3.1 Glacial maximum in the Southern Ross Sea

At Taylor Ridge, 20 km upstream from the mouth of Scott Glacier, a lateral moraine at 1200 m marks the maximum elevation of ice during the LGM. The depositional limit consists of scattered boulders and perched cobbles resting stably on an older, heavily weathered glacial deposit (Figure 2.12). Apparent exposure ages of the LGM deposits range from 19.4 ± 0.6 to 16.4 ± 0.3 kyr B.P. (Figure 2.2b). At Mount Kyffin, ∼10 km upstream from the mouth of Beardmore Glacier, the upper limit of an ablation till at ∼1050 m marks the maximum elevation of LGM glacier ice. The deposit is ice-cored in places and consists of relatively unweathered cobbles and boulders overlying older glacial deposits and felsenmeer surfaces (Figures 2.6 and 2.7). Here we primarily sampled boulders resting on other much larger, stable, boulders. Exposure ages range from 52.3 ± 1.4 to 16.7 ± 0.5 kyr B.P. (Figure 2.2d). The two oldest ages are artifacts of prior exposure; the spread of the remaining ages from 22.5 to 16.7 kyr B.P. may represent a prolonged glacial maximum or lesser degrees of prior exposure. In either case, these highstands were sustained at both sites until ∼17 - 16 kyr B.P. and possibly later, given that we may not have collected the youngest rocks at each site.

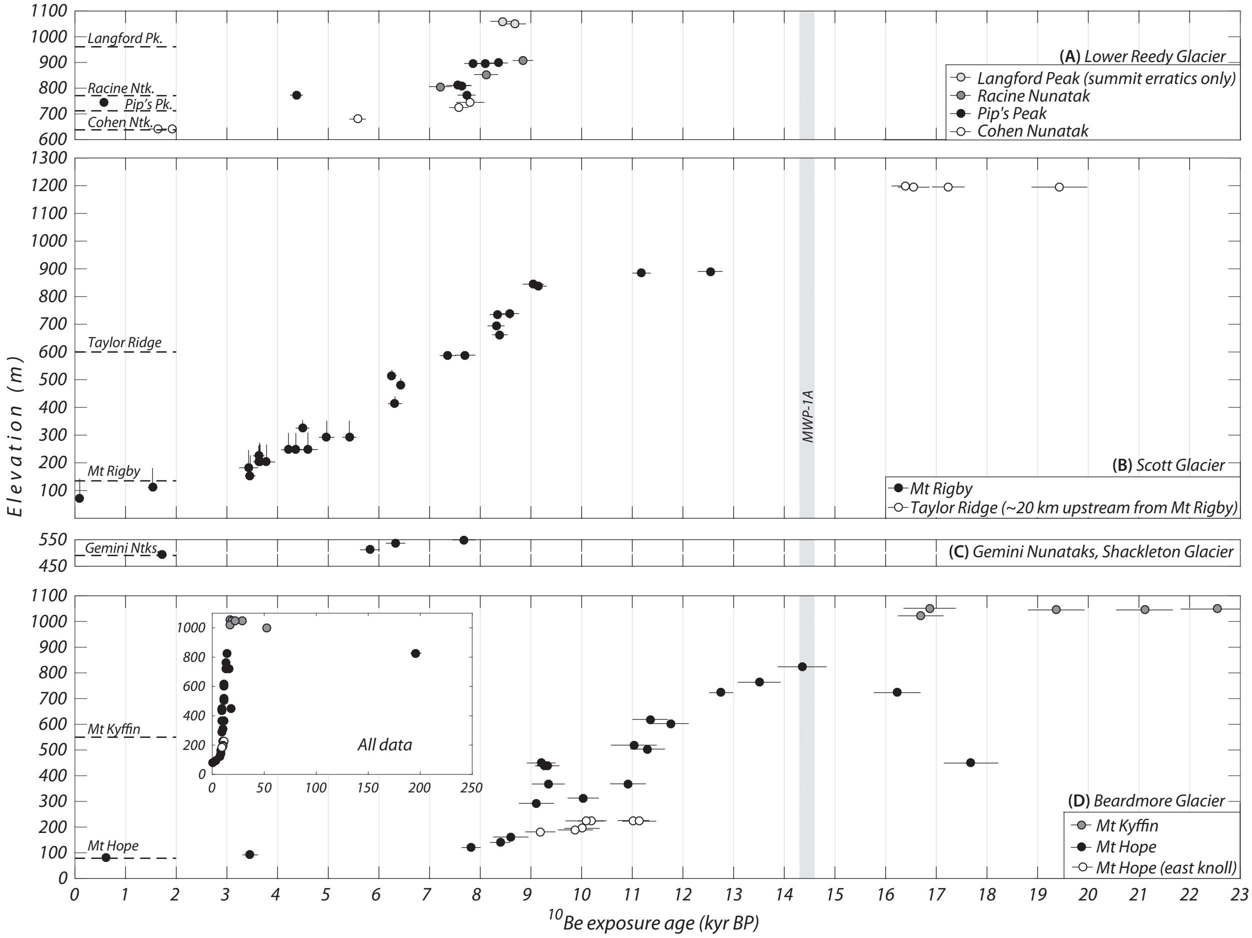

Figure 2.2: Exposure ages of glacial deposits, plotted versus elevation. See Figure 2.1 for site locations. (a) Lower Reedy Glacier nunataks [Todd et al., 2010]. (b) Mount Rigby and Taylor Ridge at Scott Glacier. (c) Gemini Nunataks at Shackleton Glacier. (d) Mount Hope and Mount Kyffin at Beardmore Glacier. Inset shows the apparent exposure ages of all samples from these sites. For Figures 2.2a-d, the modern glacier surface elevations are represented by horizontal dashed lines, and the gray vertical bar represents the timing of MWP-1A [Carlson and Clark, 2012]. See supporting information for discussion of sample elevations in Figures 2.2b-d.

During the LGM, Scott Glacier ice descending from 1200 m at Taylor Ridge must have covered Mount Rigby (893 m), located at the glacier mouth (Figure 2.1b) by significantly less than 300 m. Mount Rigby remained ice-covered until 12.5 ± 0.3 kyr B.P. (Figure 2.2b). Minimal thinning occurred between the onset of deglaciation at Taylor Ridge and the emergence of Mount Rigby's summit, spanning the period of MWP-1A. Across the mouth of Beardmore Glacier from Mount Kyffin, Mount Hope (836 m) remained ice covered until 14.4 ± 0.5 kyr B.P. (Figure 2.2d). No more than ∼200 m of thinning, and potentially much less, could have occurred at Beardmore Glacier during the MWP-1A interval.

2.3.2 Rapid Thinning of Southern Ross Sea Glaciers

Scott Glacier

Below the summit of Mount Rigby, exposure ages decrease with elevation and record rapid thinning of Scott Glacier at ∼8.4 and ∼6.3 kyr B.P. (Figure 2.2b). After the second of these events, the ice surface gradually lowered over the next ∼3 kyr to near the modern glacier level. The two lowest and youngest samples from Mount Rigby come from an ablation hollow in the surrounding, near-stagnant debris field, below modern glacier level (Figure 2.9). This area northeast of Mount Rigby apparently stagnated between ∼3.5 and ∼1.5 kyr B.P. (Figure 2.2b) and has since ablated by tens of meters; exposure of these two samples was not connected to further lowering of the glacier surface.

Beardmore Glacier

Erratics from Mount Hope's southeast ridge record gradual thinning of the margin of Beardmore Glacier to an elevation of 440 m by ∼9.3 kyr B.P. (Figure 2.2d). The ice surface then abruptly dropped ∼280 m over the next 700 ± 200 years to within 80 m of the modern glacier level. Five samples from the Mount Hope transect are clearly older than samples collected nearby at similar elevations, and these older ages are interpreted to be the result of prior exposure. We also collected erratics from a small knoll on the east side of Mount Hope (Figure 2.4). Ages there are consistently 1 - 2 kyr older than the elevation transect described above (Figure 2.2d). It appears that this part of the mountain was exposed earlier than the southeast ridge. This may have resulted from higher ablation (due to its northerly aspect or wind circulation around the peak) or from the propensity for ice to flow past the sharp southeast ridge rather than divert into the lee of the ridge. The same effects keep the modern Ross Ice Shelf surface ~80 m lower north of the peak than below the southeast ridge.

Shackleton Glacier

At Shackleton Glacier, our deglaciation record only extends ~50 m above the modern ice (Figures 2.2c and 2.8), but it reveals that the highest point on Gemini Nunataks became exposed 7.7 ± 0.2 kyr B.P., indicating near-complete deglaciation of lower Shackleton Glacier by this time (Figure 2.2c).

Reedy Glacier

Small nunataks at the mouth of Reedy Glacier (Langford Peak, Racine Nunatak, Cohen Nunatak, and Pip's Peak), which are ~130 km upstream of the modern Siple Coast grounding line (Figure 2.1b), record the last stages of ice thinning farther along the Transantarctic Mountains. Data from Todd et al. [2010], which have been recalculated to be consistent with samples presented in this paper, show that the summits of these nunataks became ice free ~8.8 - 7.8 kyr B.P., and except for Cohen Nunatak, their lower slopes were exposed within the following few thousand years, establishing the modern ice surface at these sites (Figure 2.2a). Deglaciation of these peaks overlapped with rapid ice thinning at Mount Hope and Mount Rigby.

2.4 Discussion

2.4.1 Relation between grounding-line retreat and upstream thinning

Deglaciation at the mouths of four major outlet glaciers described in section 2.3 was largely confined to the early Holocene and included abrupt events that removed hundreds of meters of ice in periods on the order of ∼1 kyr. The thinning records provide information about grounding-line retreat in the Ross Sea, discussed below in section 2.4.2. Establishment of present-day ice levels on lower Beardmore, Shackleton, and Scott Glaciers (Figure 2.2) requires the grounding line to have arrived at these sites, bringing ice at the glacier mouths to flotation

Prior to this time, we expect glacier thinning to be coupled to grounding-line retreat farther downstream. Modern analogues of this behavior come from recent observations and numerical modeling, which show that changes at the grounding line of deep marine basins beneath Pine Island and Thwaites Glaciers cause rapid thinning over decadal time scales hundreds of kilometers upstream [Payne et al., 2004; Favier et al., 2014; Joughin et al., 2014]. Further, a model of Holocene retreat of Mackay Glacier located along the Scott Coast (Figure 2.1c) was used to simulate progressive thinning of the glacier as the grounding line retreated from a location 85 km downstream [Jones et al., 2015]. Model results indicate (i) hundreds of meters of thinning occurs on decadal timescales; (ii) thinning does not significantly lag grounding-line retreat; and (iii) thinning accelerates when grounding-line retreat accelerates over reverse bed slopes [Jones et al., 2015].

The majority of the seafloor over which ice from southern Transantarctic Mountains flowed is concealed beneath the modern Ross Ice Shelf (Figure 2.1) but is presumed to be covered by deformable glaciomarine sediment [Alley et al., 1989] as found near Ross Island [Naish et al., 2009; McKay et al., 2016] and at a site in the southern Ross Sea [Webb et al., 1979]. Drill cores and seismic reflection profiles collected seaward of the modern ice shelf show that the floor of the central Ross Sea consists of older, more consolidated sediments and localized bedrock outcrops [Halberstadt et al., 2016]. Despite this evidence for a more resistive bed in the north central Ross Sea, ice from Scott and Beardmore Glaciers maintained a low surface slope of $<10^3$ during the LGM, extending more than 1000 km to the grounding line from elevations of ∼1000 m at the glacier mouths (Figures 2.1 and 2.2). Such gradients, typical of modern ice streams, require either a slippery, low-resistance bed [Waddington et al., 2005; Parizek and Alley, 2004] or lightly grounded ice, which would have allowed rapid upstream propagation of changes at the grounding line.

2.4.2 Grounding-line constraints

Scott and Beardmore Glaciers maintained their LGM thicknesses until sometime between ∼16.7 and ∼14.4 kyr B.P. (Figures 2.2b and 2.2d), consistent with ^{14}C dates on foraminifera in marine sediment above till in the northern Ross Sea, near the maximum extent of grounded ice [Licht, 2004]. Thereafter, the upper flanks of Mount Rigby and Mount Hope were exposed gradually (Figures 2.2b and 2.2d), implying slow grounding-line retreat in the central Ross Sea prior to ∼9.3 kyr B.P. Over the next 700 ± 200 years, ice thinned by 200 - 300 m at both sites, indicating rapid grounding-line incursion into the southern Ross Sea. This episode brought the grounding line close to the mouth of Beardmore Glacier, where ice stood within 80 m of its present level by ∼8.6 kyr B.P. Further retreat lowered Beardmore Glacier to its modern level by ∼7.8 kyr B.P. and brought the grounding line close to the mouth of Shackleton Glacier by ∼7.7 kyr B.P. Scott Glacier, however, remained 400 - 500 m thicker than present at this time. Rapid thinning at Mount Rigby ∼6.3 kyr B.P. (Figure 2.2b) implies a second episode of rapid grounding-line recession, which was likely limited to the region south of Crary Ice Rise (Figure 2.1). The inference that this second recession involved only a small portion of the ice sheet is further supported by the fact that ice at lower Reedy Glacier did not thin at this time, in contrast to the rapid retreat that occurred ∼9 - 8 kyr B.P. (Figure 2.2a). Subsequent thinning at Mount Rigby gradually brought ice to the modern glacier level from ~6.3 to 3.4 kyr B.P. At the end of this period, the Ross Sea grounding line was likely close to its present position between the mouths of Reedy and Scott Glaciers (Figure 2.1).

2.4.3 Synchronous deglaciation of the Central and Western Ross Sea

Arrival of the grounding line at the mouths of Beardmore and Shackleton Glaciers ~9 - 8 kyr B.P. coincided with final deglaciation of the Scott Coast region, ~800 km north along the Transantarctic Mountains (Figure 2.1). This indicates that much of the ice in the central and western Ross Sea was evacuated in a single brief period of deglaciation and grounding-line retreat ~9 - 8 kyr B.P., thereby ruling out the earlier conception of gradual and progressive grounding-line retreat along the Transantarctic Mountains [Conway et al., 1999].

The deglaciation history of the Scott Coast and northern Ross Sea is largely based on radiocarbon ages and is summarized below. Where necessary, published ^{14}C dates have been recalibrated using IntCal13 and Marine13 ^{14}C calibration curves [Reimer et al., 2013] and Southern Ocean marine reservoir corrections [Hall et al., 2010]. We do not rely on ^{14}C measurements on acid-insoluble organic material, as these commonly contain pre-Quaternary carbonaceous material derived from glacial or marine sediment upstream [Andrews et al., 1999]. Apparent ages of acid-insoluble organic matter are therefore often thousands of years older than the depositional age of the sediment. Previously published exposure ages have been recalculated to be consistent with samples presented in this paper.

Relative sea level curves from McMurdo Sound and Terra Nova Bay (Figure 2.1c) suggest final removal of grounded ice shortly before ~7.8 and ~8.0 kyr B.P., respectively [Baroni and Hall, 2004; Hall et al., 2004]. These ages agree with limiting ages from ice-dammed lakes in Taylor Valley [Hall and Denton, 2000] and with dates of the oldest postglacial marine shells retrieved from the McMurdo region [Licht et al., 1996; Kellogg et al., 1990]. Exposure ages from near the mouth of Mackay Glacier, which flows across the Scott Coast, indicate rapid thinning to near-modern levels ~7 kyr B.P. [Jones et al., 2015]. Carbon-14 ages of foraminifera in marine sediment recovered ~60 km east of Ross Island indicate open-water conditions there by 8.6 ± 0.25 kyr B.P. [McKay et al., 2016]. This is older than deglaciation ages from farther to the west and may imply that the grounding line retreated shoreward, resulting in open-water conditions at the core site before sites closer to the coast became ice free [McKay et al., 2016; Lee et al., 2017]. Taken together, these ages indicate that grounded ice withdrew from the Scott Coast region between ~8.6 and 7 kyr B.P. Within the uncertainties of the dating methods, this was synchronous with grounding-line retreat past the mouths of Beardmore and Shackleton Glaciers, indicating that grounded ice disappeared from much of the central and western Ross Sea in a period of less than 2 kyr.

2.4.4 Controls on rapid deglaciation ~9 - 8 kyr B.P.

Rapid deglaciation occurred despite stabilizing conditions of falling relative sea level. By this time, the glacio-isostatic effects of unloading grounded ice around the Ross Embayment exceeded eustatic sea level rise, as shown by relative sea level curves from the Scott Coast [Baroni and Hall, 2004; Hall et al., 2004]. The stabilizing effect should have increased southward, because isostatic rebound increased toward the ice sheet interior [Peltier, 2004]. Thus, two factors most likely influenced rapid deglaciation in the southern Ross Embayment: (i) enhanced melting at the grounding line and (ii) retreat into deep marine troughs to the south. Although increased ocean heat transport to the marine ice margin may have significantly affected the mass balance, as presently seen in the Amundsen Sea [Alley et al., 2015], this cannot be verified at present because proxy records of Ross Sea water temperature do not yet exist. Troughs in the western Ross Sea coalesce southward into a deep basin offshore of the Transantarctic Mountains (Figure 2.1). Because the discharge of marine-based ice sheets increases nonlinearly with ice thickness at the grounding line [Weertman, 1974; Schoof, 2007], the recession may have accelerated as the grounding line moved into this basin. This applies whether retreat progressed rapidly southward along the mountain front or shoreward from the central Ross Sea (Figure 2.1). The latter scenario is supported by (i) ^{14}C ages of foraminifera in marine sediment retrieved from ~60 km east of Ross Island [McKay et al., 2016], which predate deglaciation ages from farther west along the Scott Coast (Figure 2.1c), and (ii) seafloor geomorphic features in the central Ross Sea [Halberstadt et al., 2016] and near Ross Island [Lee et al., 2017], which also indicate shoreward grounding-line retreat.

2.4.5 Sea level contribution

Our results indicate that the Ross Sector's contribution to sea level peaked ~9 - 8 kyr B.P. Sea level records from sites far from the isostatic influence of ice sheets show large and rapid rises at this time [Khan et al., 2015, and references therein]; however, a large portion of this meltwater likely came from the final stages of Northern Hemisphere deglaciation [Peltier et al., 2015]. Data-constrained ice sheet models indicate that the Ross Sector only contributed 3 - 4 m to sea level during the entire deglaciation [Briggs et al., 2014; Whitehouse et al., 2012]. We show that much of this meltwater was released 5 - 6 kyr after MWP-1A, which indicates that the Ross Sector did not significantly contribute to this event. These same models suggest that the total Antarctic sea level contribution during the last deglaciation was ~7 - 14 m [Briggs et al., 2014; Whitehouse et al., 2012; Stuhne and Peltier, 2015; Golledge et al., 2012], less than most estimates of MWP-1A sea level rise [e.g. Liu et al., 2016; Lambeck et al., 2014; Deschamps et al., 2012; Peltier et al., 2015. Geologic data from around the continent show deglaciation continuing into the late Holocene, long after MWP-1A. None of this evidence is consistent with an Antarctic source for the enormous volume of meltwater released to the oceans in a few hundred years during MWP-1A.

After ~9 - 8 kyr B.P., the Ross Sector ceased contributing significantly to global sea level rise. As discussed in section 4.2, rapid thinning at Mount Rigby ~6.3 kyr B.P. was likely related to an episode of grounding-line recession that only removed a small portion of the grounded ice in the Ross Sea.

2.5 Conclusions

We present ice-thinning records from the southern Transantarctic Mountains that constrain the chronology and pattern of grounding-line recession in the Ross Sea. In conjunction with deglaciation constraints from the Scott Coast region, these data reveal an episode of rapid recession in the early Holocene that removed grounded ice from much of the central and western Ross Sea. In contrast, previous reconstructions of Ross Sea deglaciation, based almost exclusively on geologic constraints from the northern Ross Sea, have been forced to infer gradual retreat in the southern Ross Sea [e.g., Conway et al., 1999; Anderson et al., 2014.

During the MWP-1A episode, the Ross Sector neither contributed nor responded significantly to global sea level rise; rather, much of the Ross Sea deglaciated ∼9 - 8 kyr B.P., several thousand years after MWP-1A. Because we can rule out other factors, this episode of rapid retreat was likely influenced by enhanced melting at the grounding line and/or unstable retreat into deep marine basins.

2.6 Acknowledgments

Support for this work was provided by U.S. National Science Foundation (NSF) grants 0636818 and 0838818 and the United States Antarctic Program. P.S. received funding from the NSF Graduate Research Fellowship Program. We thank Maurice Conway and Lesley Urasky for assistance in the field, Joy Laydbak and Marcus Gladden for assistance with sample preparation, and Robert Finkel, Dylan Rood, Susan Zimmerman, and Tom Brown for accelerator analyses. Additionally, we thank Andrew Hein, Joanne Johnson, and an anonymous reviewer for constructive feedback. The data described in this paper are included in the supporting information.

2.7 Supplementary information

2.7.1 Sample Elevation Details

Sample elevations are based on drift-corrected barometric measurements, bench-marked to a network of geodetic GPS observations. Elevation accuracy is typically ± 3-4 m based on repeat measurements.

Age-elevation data in Figure 2.2 are plotted at the present elevation of each sample. However, because (i) ice-surface elevations decrease downstream, and (ii) our transects on Mt Rigby, Gemini Nunataks, and Mt Hope span up to 8 km in the along-flow direction of the glaciers (Figure 2.3), presenting the data in this way risks plotting samples exposed simultaneously at the up- and downstream ends of the transects at different elevations. To account for this, we project sample elevations along flowlines to a common point on each transect using the surface slopes of the glacier. Beardmore, Shackleton, and Scott Glaciers were likely close to their present slopes when low elevation samples were deposited in the past few thousand years. Older, higher-elevation samples were likely deposited when the glaciers had lower slopes and grounding lines were hundreds of kilometers downstream. Thus, projections using the modern glacier gradients as well as hypothetical flat glaciers (i.e. no slope) results in upper and lower bounds on sample elevations when projected to a common point.

At Mt Rigby, we projected along an approximately NW-SE transect to the summit (-85.5408°, -154.6323°), using the modern glacier slope of 0.015. At Gemini Nunataks, samples were projected along a roughly N-S transect to the highest elevation sample (-84.7064°, -176.6104°) using the modern glacier slope of 0.02. At Mt Hope, the flow direction of Beardmore Glacier likely rotated slightly to the east as the mountain emerged during deglaciation. Thus, we projected Mt Hope samples along an approximately NNE-SSW transect to the highest-elevation sample (-83.5134°, 171.2863°), using the modern glacier slope of 0.017. Samples from Mt. Kyffin and Taylor Ridge were not projected because, at each site, they were collected within a short distance of each other.

The results of these projections are shown in Figures 2.2 and 2.3. In both figures, the actual sample elevations are represented by dots, and the projected elevations are represented by vertical lines in Figure 2.2 and by crosses in 2.3. At Gemini Nunataks and Mt Hope, the differences between the actual sample elevations and the projected elevations using the modern glacier slopes are less than 7 m and 16 m, respectively, and are not visible in Fig. 2. At Mt Rigby, the maximum elevation difference is +73 m. Note that actual sample elevations were used to calculate exposure ages.

2.7.2 Sample Preparation and ^{10}Be Measurements

Samples were prepared for ^{10}Be/^{9}Be measurements at the University of Washington Cosmogenic Nuclide Laboratory. We crushed and sieved samples at 250-500 μm and purified quartz using surfactants and etching with dilute HF [Kohl and Nishiizumi, 1992]. Following HF dissolution, we separated Be using ion-exchange chromatography [Ditchburn and Whitehead, 1994], and measured Be isotope ratios at the Lawrence Livermore National Laboratory Center for Accelerator Mass Spectrometry (LLNL-CAMS). Isotope ratios were measured relative to the ICN 01-5-4 Be standard, assigned a ^{10}Be/^{9}Be ratio of 2.851×10^{-12} [Nishiizumi et al., 2007]. Complete procedural blanks, including ^{10}Be added with the Be carrier were $<$ 15,000 atoms ^{10}Be.

2.7.3 Exposure Ages and Production Rates

Beryllium-10 exposure ages were calculated using the CRONUS calculator version 2.3 [Balco et al., 2008]. Beryllium-10 production rates by spallation are based on the global calibration dataset by Borchers et al. [2016], adjusted for altitude and latitude using the scaling scheme by Lal [1991] and the relationship between Antarctic air pressure and elevation [Stone, 2000]. Some recent production-rate calibrations suggest lower values than that of Borchers et al.

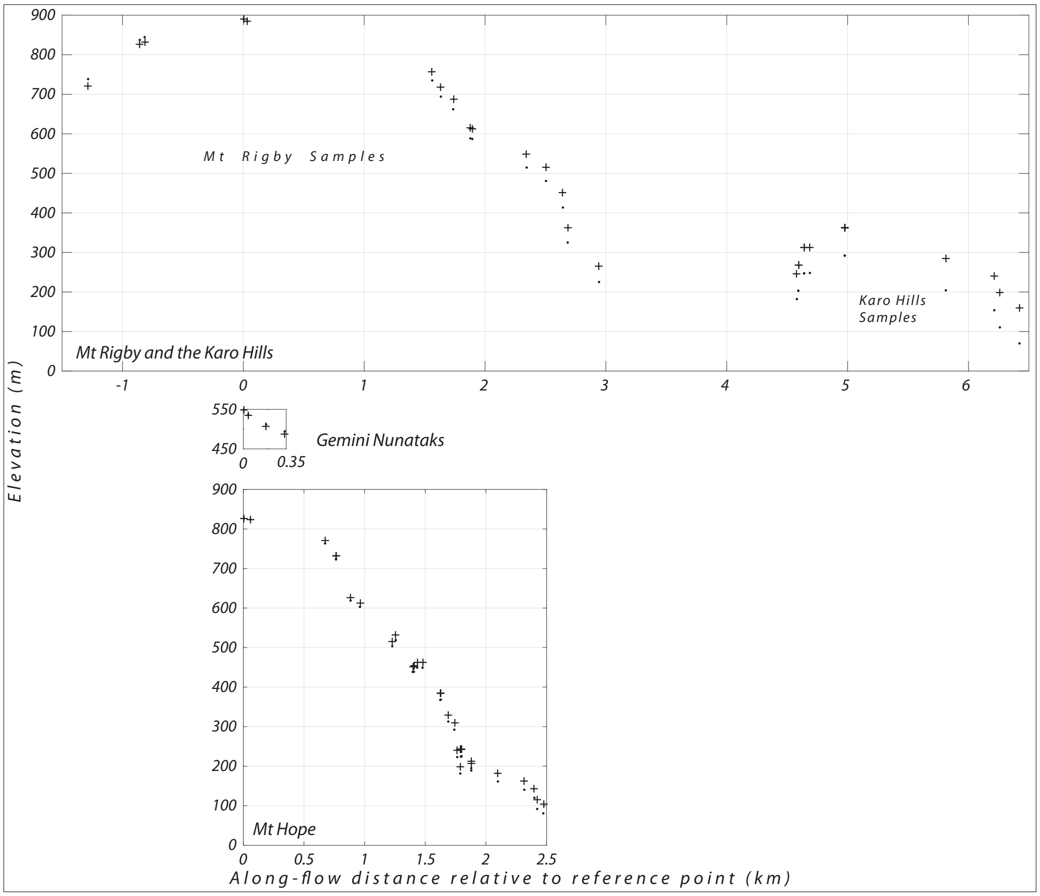

Figure 2.3: Plots of elevation vs along-flow distance for samples from Mt Rigby and the Karo Hills (top), Gemini Nunataks (middle), and Mt Hope (bottom). All plots have the same horizontal and vertical scales. Zero on the abscissas marks the along-flow location of the highest-elevation sample at each site, and is where other samples from that site are projected to. Actual sample elevations are represented by black dots, while crosses represent sample elevations after projection to a common point (i.e. zero on each abscissa).

[2016]. Using other combinations of high-latitude calibration datasets and scaling schemes would increase exposure ages by 1-6%, which would not substantially affect the findings of this research.

For simplicity, production rates are assumed to be constant in time. Effects of paleomagnetic variation should be minimal at the high latitude of our field sites. Sample elevations will have increased during their exposure due to isostatic rebound. There are no relative sea-level (RSL) curves from the southern Ross Sea from which to evaluate the amount and timing of rebound. We therefore used RSL predictions from the Antarctic deglaciation model of Briggs et al. [2014] to estimate the magnitude of this effect on exposure ages. Changes in altitude predicted by the model are largest for samples with the longest exposure histories, deposited during or shortly after the glacial maximum. Incorporating these changes into our calculations would increase exposure ages of glacial maximum samples by ~10%. This is likely an upper limit because the Briggs et al. [2014] model somewhat overestimates LGM ice thickness in the southern Ross Sea. The effect on samples exposed during deglaciation is smaller (diminishing to near zero for late Holocene deposits) though accurate corrections depend on the assumed timing of deglaciation in the model. Because no model to date captures the rapid deglaciation documented here, we have not applied isostatic corrections to the exposure ages. Nonetheless they should be regarded as lower limits by 0-2 kyr.

2.7.4 Exposure Dating Uncertainties

When comparing ^{10}Be exposure ages to one another, we use an internal uncertainty, which incorporates all known sources of laboratory and AMS measurement uncertainty, but excludes uncertainty in the age of the calibration site used to derive the ^{10}Be production rate. The latter represents a bias shared by all of the ages being compared, and cancels out when comparing one exposure age to another. When comparing exposure ages to ages based on other dating methods we incorporate the uncertainty in the calibration site age, giving a larger external error (see above discussion about alternative production rates). For example, external errors are used in this study when comparing exposure ages from Transantarctic Mountain glaciers to ^{14}C ages from the Victoria Land coast. AMS measurement uncertainties propagated into the data used here include both the error associated with the sample analysis, and an error associated with laboratory reproducibility. For samples analyzed prior to 2010, we estimate the latter at $\sim \pm 1\%$, based on replicate sample measurements. Since 2010 we have repeatedly analyzed an internal laboratory standard 04-RDY-139-STR, and the CRONUS-A rock standard [Jull et al., 2015], ^{10}Be-rich samples that can be measured at high precision, to detect any scatter due to laboratory and AMS procedures in excess of calculated concentration errors. We find that our measurements of ^{10}Be concentration in these standards since 2010 scatter more than expected from their analytical precision; calculated analytical errors must be increased by adding a further 2.1% error, in quadrature, to obtain a p-value of 0.3 for these replicates. We have increased the uncertainties of all samples measured since 2010 in the same way.

2.8 Supplementary figures

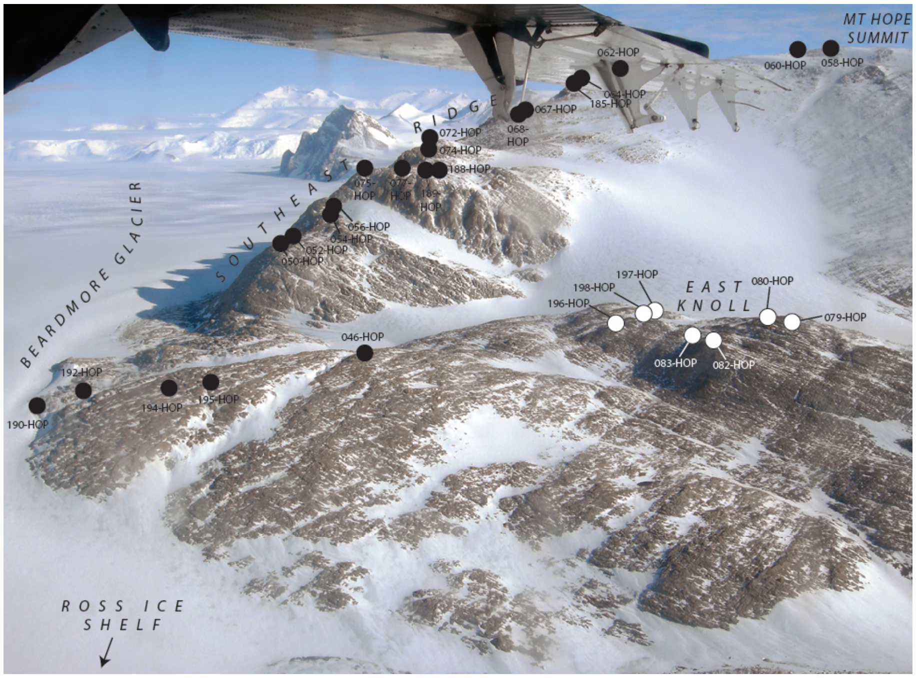

Figure 2.4: Aerial view of Mt Hope and Beardmore Glacier, looking to the south. Glacial erratic samples are represented by black and white circles. The underside of an airplane wing is visible in the top of the photo.

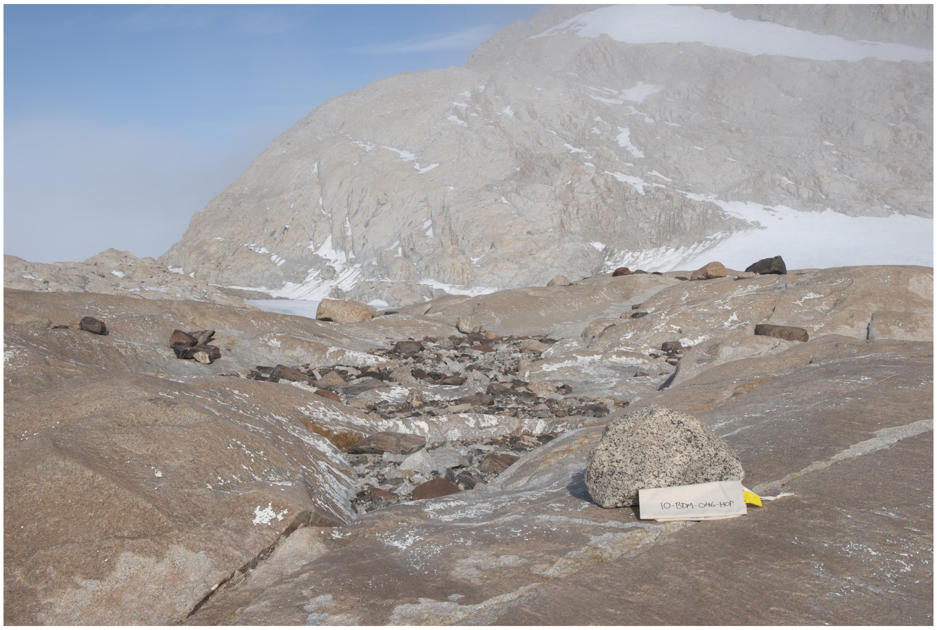

Figure 2.5: Photo of an erratic (sample 10-BDM-046-HOP) resting on glacially-smoothed bedrock on the lower flanks of Mt Hope (Figure 2.4). The southeast ridge rises in the background.

Figure 2.6: Glacial deposits on the northern flank of Mt Kyffin. Minimally-weathered LGM deposits rest on older glacial deposits and felsenmeer surfaces (not visible in this photo).

Figure 2.7: Exposure of ice revealed from beneath LGM glacial debris on Mt Kyffin.

Figure 2.8: View of glacial deposits resting on sculpted bedrock of the southern peak of Gemini Nunataks. The peaks in the distance on the right are located at the glacier mouth. The sample bag in the foreground shows the location of 10-BDM-088-GEM, which was not analyzed. The summit region is visible in the upper left, and is where sample 10-BDM-091-GEM was collected.

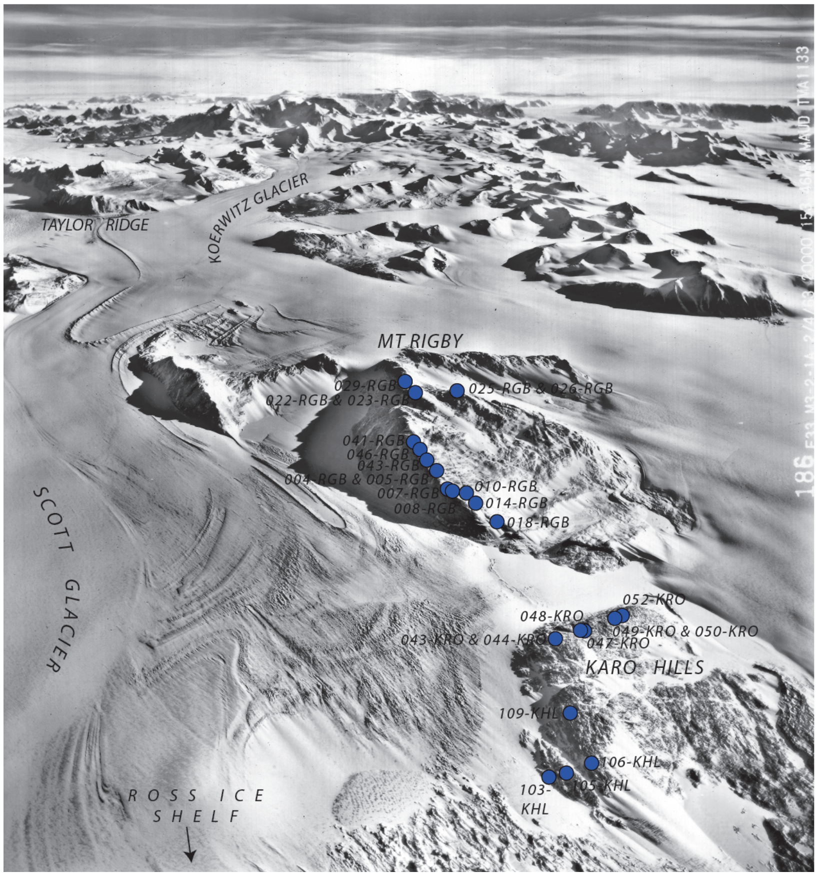

Figure 2.9: Aerial photo of Mt Rigby and the Karo Hills, at the mouth of Scott Glacier. Glacial erratic samples are labeled and are represented by blue circles. Taylor Ridge is located at the confluence of Koerwitz and Scott Glaciers. Only a small portion of the western margin of Scott Glacier is visible in this photo.

Figure 2.10: View looking up the northern ridge of Mt Rigby. The rounded light-colored erratic in the foreground is 07-SCT-004-RGB. Erratics collected on this ridge rest either on bedrock, fractured bedrock, or on older glacial deposits.

Figure 2.11: Photo looking up Scott Glacier from Mt Rigby. Taylor Ridge rises above the ice in the upper-right part of the photo. The foreground shows an unweathered glacial erratic resting on oxidized bedrock (this erratic was deemed too beautiful to sample). An erratic was collected from the bedrock crevice (next to the sample bag). The eastern flank of Mt Rigby, shown in the middle distance of the photo on the right, is also draped with glacial debris. We sampled along ridges, where samples rest stably on bedrock or older glacial deposits, and are unlikely to have moved since deposition.

Figure 2.12: Photo of the glacial deposit at Taylor Ridge. Minimally weathered clasts (grey in the photo), sit on older weathered deposits (brown in the photo).

Chapter 3

WEST ANTARCTIC SITES FOR SUBGLACIAL DRILLING TO TEST FOR PAST ICE-SHEET COLLAPSE

Authors Perry Spector, John Stone, David Pollard, Trevor Hillebrand, Cameron Lewis, Joel Gombiner

Submitted to The Cryosphere

ABSTRACT Mass loss from the West Antarctic Ice Sheet (WAIS) is increasing, and there is concern that an incipient large-scale deglaciation of the marine basins may already be underway. Measurements of cosmogenic nuclides in subglacial bedrock surfaces have the potential to establish whether and when the marine-based portions of the WAIS deglaciated in the past. However, because most of the bedrock revealed by ice-sheet collapse would remain below sea level, shielded from the cosmic-ray flux, drill sites for subglacial sampling must be located in areas where thinning of the residual ice sheet would expose presently subglacial bedrock surfaces. In this paper we discuss the criteria and considerations for choosing drill sites where subglacial samples will provide maximum information about WAIS extent during past interglacial periods. We evaluate candidate sites in West Antarctica and find that sites located adjacent to the large marine basins of West Antarctica will be most diagnostic of past ice-sheet collapse. There are important considerations for drill-site selection on the kilometer scale that can only be assessed by field reconnaissance. As a case study of these considerations, we describe reconnaissance at sites in West Antarctica, focusing on the Pirrit Hills, where in the summer of 2016-2017, an 8 m bedrock core was retrieved from below 150 m of ice.

3.1 Introduction

There is strong but indirect evidence for a diminished West Antarctic Ice Sheet (WAIS) during some past warm interglacial periods of the Pleistocene. Coastal records of former sea-level highstands [see reviews in Dutton et al., 2015], along with geological evidence from Antarctica [Scherer et al., 1998], ice-sheet modeling experiments [e.g. Pollard and DeConto, 2009], and other lines of evidence [e.g. Barnes and Hillenbrand, 2010; NEEM community members, 2013; see review in Alley et al., 2015] suggest large-scale deglaciation of the WAIS within the past ∼1 Myr, which may have occurred as recently as the last interglacial period, ∼125 kyr ago. It has also been suggested that the WAIS, along with the Greenland Ice Sheet and parts of the East Antarctic Ice Sheet, disappeared during the mid-Pliocene (∼3 Myr ago), the last time atmospheric CO_2 concentrations reached modern levels. However, the evidence for this, which largely consists of relative sea-level data and marine oxygen isotope records, has large uncertainties which preclude robust estimates of sea-level and ice-sheet volume during this period [see reviews in Dutton et al., 2015 and Raymo et al., 2017].

Large-scale deglaciation of the WAIS (so-called "collapse") is theorized to occur because much of the ice sheet overlies deep marine basins in a configuration that makes it susceptible to a feedback between marginal retreat, flow acceleration, thinning, and flotation [Weertman, 1974; Schoof, 2007]. Increasing ice loss is presently occurring through these mechanisms in the Amundsen Sea sector of the WAIS (Fig. 3.1) [see review in Scambos et al., 2017], and numerical modeling suggests that an incipient collapse of the ice sheet is underway in this sector [e.g. Joughin et al., 2014]. How much and how quickly future sea level will rise due to WAIS deglaciation remains unknown [Scambos et al., 2017], but continued ice loss could eventually increase global mean sea level by 3-4 m [Bamber et al., 2009]. Knowledge of ice-sheet extent during interglacials warmer and more prolonged than the Holocene would be invaluable for understanding, and potentially predicting, the future stability or instability of the WAIS. Geological observations from West Antarctica which constrain the configuration of the WAIS during former interglacial periods remain scarce because evidence of its limits during these times is concealed beneath the present-day ice sheet.

One potential source of evidence is the presence or absence of long-lived cosmogenic nuclides in subglacial bedrock. Because most cosmic radiation is absorbed by as little as 5-10 m of ice cover, discovering significant concentrations of these nuclides would provide unambiguous evidence for former ice-free conditions and could establish whether the WAIS collapsed during the past few million years. At sites affected by a single collapse, cosmogenic-nuclide measurements can directly date that event. In the case of more complex deglaciation histories, the same data record the cumulative exposure time of the bedrock surface. Although cosmogenic nuclides have the potential to unambiguously indicate past ice-sheet collapse on timescales ranging from the Holocene to the Pliocene, the power of the method depends on careful site selection. In this paper we describe the criteria and considerations for choosing subglacial sampling sites where cosmogenic-nuclide data will provide the maximum amount of information about WAIS extent during past interglacials.

In central Greenland, a bedrock core was opportunistically retrieved from below the full thickness of the ice sheet at the GISP2 drilling site. Concentrations of cosmogenic ^{10}Be and ^{26}Al in the core require periods of prolonged exposure during the Pleistocene when the ice sheet was largely absent [Schaefer et al., 2016; Nishiizumi, 1996]. In contrast to this work, bedrock recovered from below the thick portions of the WAIS would not be capable of providing equivalent information because the bed in these areas is located far below sea level (Fig. 3.1) and would remain submerged, shielded from the cosmic-ray flux, if the ice sheet collapsed. Establishing whether the thick, marine-based portions of the WAIS disappeared in the past will therefore require drilling through adjacent, thinner portions of the ice sheet into subglacial highlands that would be exposed by ice thinning during collapse events.

In the 2016-2017 summer, the first cores of subglacial bedrock from West Antarctica were recovered from the Pirrit Hills and the Ohio Range (Fig. 3.1), which was made possible by recent advances in sub-ice drilling technology [e.g. Goodge and Severinghaus, 2016]. For these as well as future drilling efforts to provide meaningful information about past WAIS configurations, the measurements made on the recovered bedrock must be representative of the past ice-thickness at the drill site, which in turn must be linked to the extent of the broader ice sheet. In Section 2 of this paper, we describe cosmogenic-nuclide considerations that guide drill-site selection. In Section 3, we use an ice-sheet model to predict the areas of the WAIS where significant thinning (and thus exposure of presently subglacial bedrock) would occur during collapse events. In Section 4, we evaluate a group of candidate drill sites throughout West Antarctica. Finally, in Section 5, we describe reconnaissance work at three sites in West Antarctica, with emphasis on the Pirrit Hills, which we present as a case study of drill-site selection on the scale of an individual nunatak.

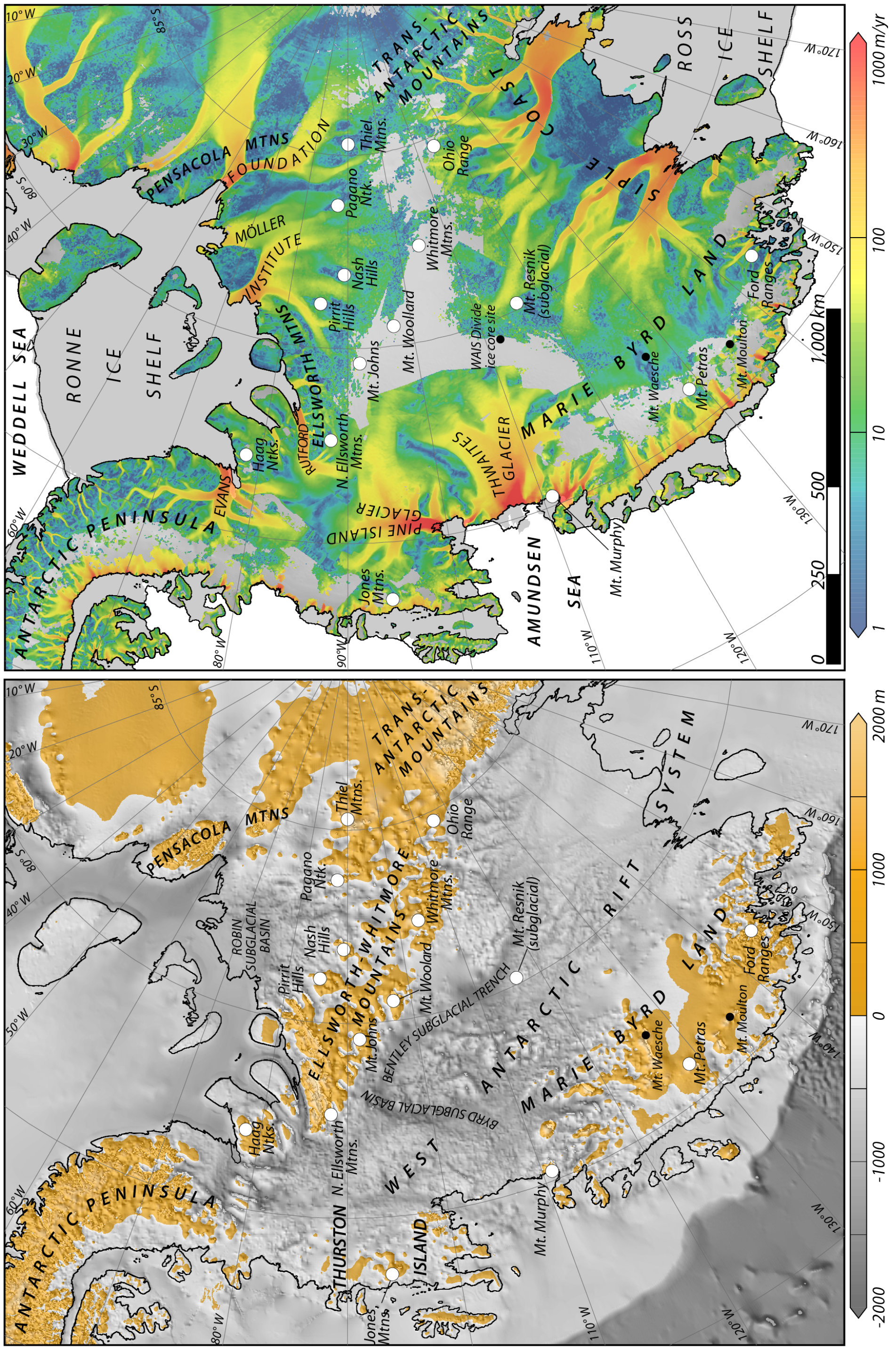

Figure 3.1: Maps of West Antarctica, colored for bedrock elevation [Fretwell et al., 2013] and the velocity of grounded ice [Rignot et al., 2011]. White circles show the locations of possible drill sites discussed in the text. Black circles show the locations of other sites discussed in the text.

3.2 Cosmogenic nuclide considerations for drill site selection

3.2.1 Strategies for subglacial bedrock sampling and analysis

Because subglacial drilling is expensive and time consuming, drill-site selection, drilling operations, and analysis of recovered samples should be designed to maximize the information provided by the inherently limited amount of subglacial bedrock. There are several strategies to accomplish this. At a given drill site, collecting multiple bedrock cores in an elevation transect below the modern ice surface can establish the magnitude of past deglaciations. By locating drill sites near outcropping mountains, elevation transects can be extended up to and above the limits of the thicker, ice-age WAIS, thereby constraining ice-thickness variations over the full glacial-interglacial cycle. Drilling near outcrops also allows the subglacial rock type to be inferred with confidence, which is important as not all lithologies are suitable for cosmogenic-nuclide measurements. Although measuring a single cosmogenic nuclide (e.g. ^{10}Be or ^{36}Cl) in subglacial bedrock samples is enough to detect past exposure, measuring several nuclides that have different half lives yields considerably more information about the glacial history, both in the recent and the distant past. Independent constraints on the most recent period of exposure can potentially be added by (i) collecting and dating the basal ice and (ii) luminescence dating of the subglacial bedrock surface. Because cosmogenic nuclides are primarily produced within the topmost few meters of the bedrock surface, preservation of the record of past exposure requires drill sites to be located in areas where erosion below or above the ice has been minimal. Knowledge of the erosion history, which is required for accurate interpretation of the glacial history, can be gained by analyzing not only surface samples of the subglacial bedrock, but by measuring depth profiles in rock cores that extend several meters below the surface.

3.2.2 Subglacial bedrock lithology

The central portion of West Antarctica is composed of three tectonic and topographic blocks, the Ellsworth-Whitmore Mountains, Marie Byrd Land, and what is known as the Thurston Island region, which are separated by low-lying areas of the West Antarctic Rift System (Fig. 3.1). The portions of the bed that would be above sea level if the WAIS collapsed are primarily located in these three tectonic regions; however there are isolated peaks and plateaus, such as subglacial Mt. Resnik [Behrendt et al., 2007], which rise above sea level from the deep marine basins (Fig. 3.1).

Drilling into these subglacial highlands must target rock types in which useful cosmogenic nuclides can be measured. Commonly measured nuclides (and their half-lives) include ^{10}Be (1.4 Myr), ^{26}Al (0.7 Myr), ^{21}Ne (stable), ^{36}Cl (0.3 Myr), ^{3}He (stable), and ^{14}C (5.7 kyr). If more of these nuclides can be measured, more restrictive time constraints can be placed on exposure episodes that may have occurred in the distant and/or recent past. Because (i) all of these nuclides (except ^{36}Cl) can be measured in quartz, and (ii) their production rates are best known for quartz, quartz-rich rocks would allow the glacial history to be constrained over a large range of timescales. Igneous or metamorphic rocks of granitic composition would permit the greatest variety of analyses because, in addition to containing quartz, they also contain potassium feldspar and (commonly) Cl-rich mica in which ^{36}Cl can be measured. Other analytical strategies could be applied to the volcanic rocks that underlie large areas of the WAIS. For example, cosmogenic ^{3}He, ^{21}Ne, and ^{36}Cl could be measured in basaltic pyroxene, or in a combination of quartz and sanidine from more felsic volcanic rocks. However, the relative abundance of useful minerals such as these is also important because of the small amount of rock that can be retrieved by subglacial drilling [Goodge and Severinghaus, 2016].

The necessity of recovering a suitable rock type implies that it will likely be advantageous to target the subglacial extension of outcropping mountains, where the rock type at depth can be inferred with confidence. Although geophysical surveys can narrow the range of possible lithologies, the precise identity and mineralogy of underlying bedrock generally remains unknown [e.g., Behrendt et al., 1994; Jordan et al., 2013]. In this paper, we largely restrict our consideration of potential drill sites to areas near mountains of granitic composition. Figure 3.1 shows the location of some of the granitic nunataks in West Antarctica. Although this map is not comprehensive, it is generally representative of their geographic distribution. Scattered granitic nunataks outcrop between the Ellsworth Mountains and the southern Transantarctic Mountains, predominately in the Weddell Sea Sector of the WAIS. Granitic nunataks are also located (i) at the base of the Antarctic Peninsula, (ii) in the Thurston Island region, and (iii) along sections of the Marie Byrd Land coast. In addition to granitic sites, in Fig. 1 we also include quartzite peaks of the northern Ellsworth Mountains; the isolated quartzite nunatak of Mt. Johns; and subglacial Mt. Resnik, which, although likely volcanic [Behrendt et al., 2007], is a tempting drill target because (i) it lies upstream of where Scherer et al. [1998] found evidence for a large-scale Pleistocene deglaciation of the WAIS; (ii) its conical form and high relief suggest that it erupted subaerially when the ice sheet was absent [Behrendt et al., 2007]; and (iii) its summit is only ∼330 m below the ice surface [Morse et al., 2002].

3.2.3 Preservation of the cosmogenic-nuclide record

Because the cosmogenic-nuclide record is primarily produced in the topmost few meters of an exposed bedrock surface, its survival requires that the bedrock remain continuously protected from erosion. This is most likely to be the case in areas that are surrounded by slow-flowing ice and where thickening of the ice sheet during past glacial periods such as the LGM was minimal. Other factors which promote cold-based ice are high accumulation rates, low surface temperatures, and a low geothermal heat flux. As discussed in Section 3.4, sites in the WAIS interior are likely to have preserved subglacial bedrock surfaces hundreds of meters below the modern ice level. Preserved subglacial surfaces also likely exist near the ice-sheet margin, however, it may be more difficult to identify these sites with confidence. Although subglacial bedrock samples that have remained continuously uneroded will provide the greatest constraints on the glacial history, samples that have experienced low rates of erosion may also be of use, provided that the erosion history can be estimated. As mentioned above, this can be done by measuring cosmogenic nuclides not only in the subglacial bedrock surface, but also in depth profiles along the length of short (∼3-6 m) bedrock cores [Ploskey and Stone, 2012].

A related concern to bedrock erosion is the possibility that presently subglacial surfaces remained concealed by till, soil, or snow when the ice sheet disappeared in the past. Failure to account for past surface cover would cause the true exposure history to be underestimated. Analysis of the subglacial bedrock core from the GISP2 site in central Greenland suggests that the present-day bedrock surface was covered by a thin layer of material when the ice sheet disappeared during the Pleistocene [Schaefer et al., 2016]. Soil accumulation there is plausible because debris-rich basal ice in the GISP2 and other Greenland ice cores, contain evidence for a vegetated landscape during one or more interglacial periods in the past million years [Willerslev et al., 2007; Bierman et al., 2014; Souchez et al., 2006]. In Antarctica, however, fossil organisms and pollen from sites spanning the continent show that a tundra landscape went extinct around the mid-Miocene, and that the climate has been continuously polar since that time [Lewis et al., 2008; Ashworth and Erwin, 2016; Anderson et al., 2011; Wei et al., 2014]. Although soil is unlikely to have covered drill targets in Antarctica during former interglacial periods, accumulated till is possible. In the vicinity of outcropping mountains where drill sites will probably be located, englacial debris commonly accumulates in blue-ice areas, and subsequent thinning could drape the underlying bedrock with a layer of till. As discussed below in Section 3.5, this concern can be mitigated by locating drill sites above subglacial ridges where the likelihood of till or snow cover is minimal.

3.3 Where will WAIS collapse cause the largest changes?

WAIS collapse is theorized to occur via a feedback in which initial retreat of the grounding line into deeper water causes more ice to flow across grounding line [Weertman, 1974; Schoof, 2007]. This accelerates the flow of the ice sheet upstream, causing it to thin, which in turn causes previously grounded ice to float as the grounding line recedes farther inland. The thinning of upstream grounded ice is important because it is the link between withdrawal of ice from the marine basins and the exposure of presently subglacial bedrock surfaces in the WAIS interior. Therefore, an overarching criterion is that drill sites be located in areas that experience the largest change in ice thickness during collapse events. Recent observations in the Amundsen Sea sector show that thinning induced by grounding-line retreat is greatest near the ice-sheet margin, but remains detectable hundreds of kilometers upstream [Pritchard et al., 2012]. This suggests that although large portions of the WAIS are prone to thinning during deglaciations, some sites will be more or less diagnostic of past ice-sheet collapse.

The geological and glaciological constraints on WAIS configuration during times of reduced ice volume are scant [Scherer et al., 1998; Korotkikh et al., 2011; Mulvaney et al., 2014] and therefore of limited use for assessing the response of candidate drill sites during collapse events. A much more complete record exists for the deglaciation of marine-based ice in the Ross Sea following the LGM, which may provide a useful analog. Withdrawal of ice from the outer Ross Sea, where the ice-sheet was relatively thin, led to moderate thinning of ∼300 m in adjacent areas of northern Victoria Land [Goehring, pers. comm., 2018]. Moderate thinning also occurred at Siple Dome [Waddington et al., 2005; Price et al., 2007], which overlies a broad area of high topography, as well as at the Ohio Range [Ackert et al., 2007], which remains well upstream of the modern grounding line. The greatest thinning (>1 km), however, is recorded at sites in the southern Transantarctic Mountains that directly abut a deep marine basin in the western Ross Sea which lost ∼1.5-2 km of ice [Spector et al., 2017; Bromley et al., 2012]. Collectively, these observations suggest that if the WAIS collapsed during past interglacial periods, the greatest thinning likely occurred at sites directly adjacent to the deep marine basins in West Antarctica that became ice free, such as Bentley Subglacial Trench (Fig. 3.1).

In order to examine the transient response of different parts of the WAIS to collapse events, and thereby identify which areas will be most diagnostic of past deglaciations, we use the Penn State University ice-sheet model (PSU-3D) to simulate the Antarctic Ice Sheet continuously over the past 5 Myr. This time period, from the early Pliocene to the present, covers a large range of glacial-interglacial climates and is comparable to the time period that can be investigated with cosmogenic-nuclide measurements. In comparison, most existing collapse simulations depict only a single deglaciation [e.g. Feldmann and Levermann, 2015] or are equilibrium models [e.g. de Boer et al., 2015] which may not represent ice-sheet behavior during short-lived events such as Pleistocene interglacial periods.

The model we use solves a hybrid combination of the scaled dynamical equations for the flow of grounded and floating ice [Pollard and DeConto, 2009, 2012a,b]. It is similar to that presented in Pollard and DeConto [2009], however it uses basal sliding coefficients derived from inverse calculations, as well as improved parameterizations of ice-shelf calving and sub-ice oceanic melting [Pollard and DeConto, 2012b]. A parameterization by Schoof [2007] allows for reasonably accurate simulations of grounding-line migration on the coarse grids that are required for multi-million year model runs. We use a 40 km horizontal grid, which, although coarse, is comparable to the resolution with which the bed is known in the vicinity of many of the candidate drill sites [Fretwell et al., 2013]. Bedrock deformation in the model is treated as an elastic lithosphere above a viscous asthenosphere that relaxes toward isostatic equilibrium. The model includes two processes that exacerbate retreat during warm climates: (i) hydrofracture of ice shelves due to surface water draining into crevasses and (ii) structural failure of ice cliffs at the grounding line [Pollard et al., 2015].

The model is forced with parameterizations of surface temperature, precipitation, sub-ice-shelf melting, and sea level, which have been described in previous publications [Pollard and

DeConto, 2009, 2012a]. These parameterizations are largely functions of a stacked benthic δ^{18}O record [Lisiecki and Raymo, 2005] and orbital insolation variations [Laskar et al., 2004]. In this run, we add the influence of long-term atmospheric CO_2 decline, by prescribing a linear ramp from 400 ppmv to 280 ppmv CO_2 between 3 Ma and 2 Ma, with corresponding small uniform shifts to atmospheric and oceanic temperatures. This results in generally smaller model ice volumes prior to 3 Myr compared to Pollard and DeConto [2009]. The parameters for the simulation shown in Fig. 3.2 have been calibrated in previous model experiments [e.g. Pollard and DeConto, 2012a,b; Pollard et al., 2016]. Because many of the parameters related to the climate forcing, as well as other aspects of the model physics, are uncertain, and alternative values can affect the size of the ice sheet during interglacial and glacial periods as well as its rate of change, we use this simulation as a guide to how ice thickness at candidate drill sites responds to deglaciation of the marine basins rather than an accurate depiction of the ice sheet through time.

The model is sampled every 5000 years, which sufficiently captures the ice-sheet's variations and results in minimal aliasing. The modeled ice sheet transitions rapidly between expanded and contracted configurations on orbital frequencies that reflect the climate forcing (Fig. 3.2). The simulated ice sheet was smaller than present prior to ~2.7 Myr ago, at which time its average size began to increase, and collapsed configurations with little or no marine-based ice in West Antarctica became less frequent. Some warm periods of the Pleistocene resulted in full deglaciation of the marine basins, leaving small ice sheets on areas of high topography, as shown in Fig. 3.2b. During other interglacial periods, thinning and grounding-line retreat were more limited and seaways were unable to link the Amundsen, Ross, and Weddell Seas. Although accumulation rates increase over the residual ice sheet during deglaciations, in most areas this is insufficient to offset the dynamic thinning. Thinning is typically greatest directly upstream of the retreating grounding line, especially in areas adjoining deep marine basins that become ice free, as expected from the considerations described above.

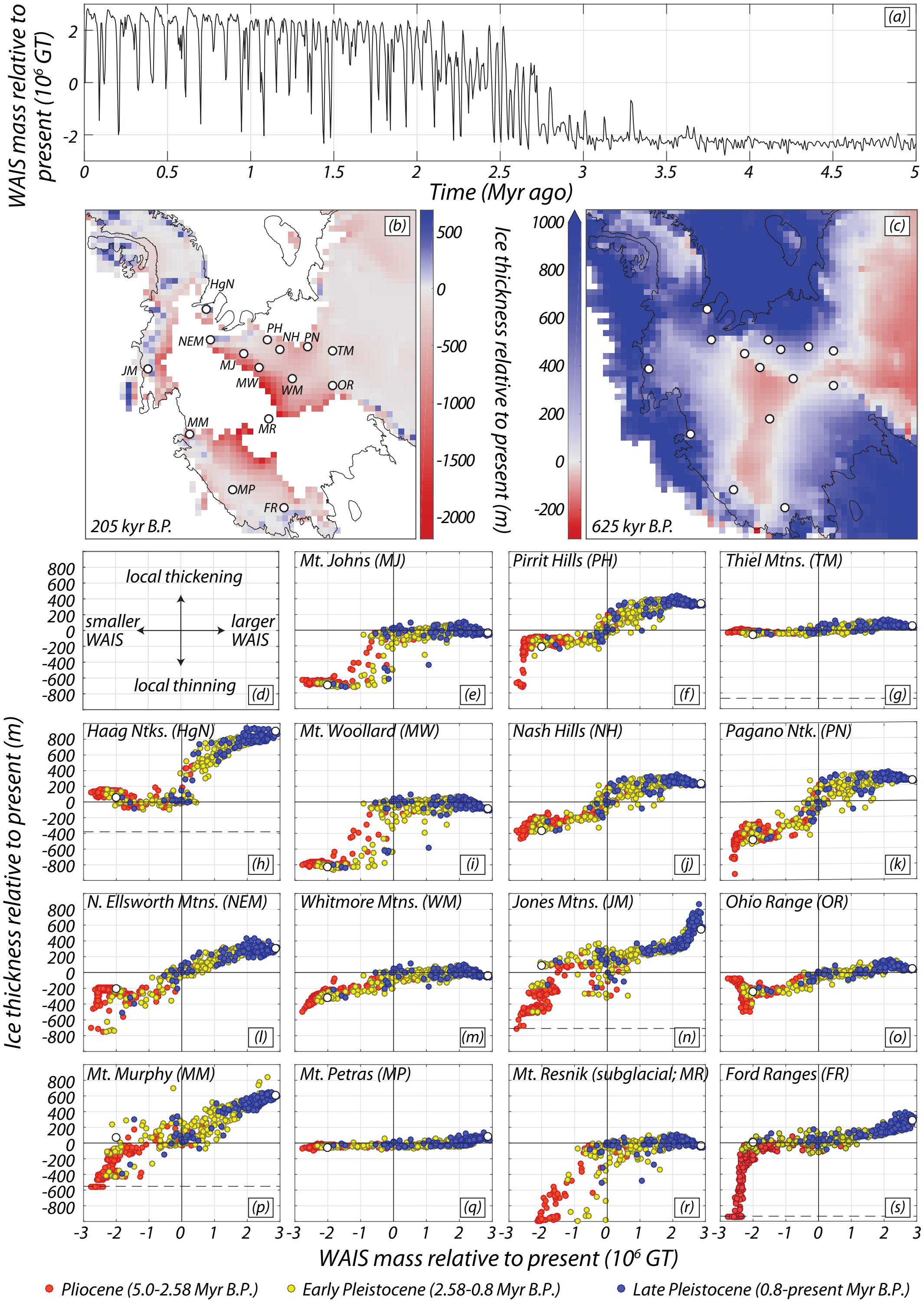

Figure 3.2: See caption on next page.

Figure 3.2: Results of a 5 Myr ice-sheet simulation. **(a)** variations in the mass of the WAIS, where the WAIS is taken to be the portion of the ice sheet between W 180° and W 50°. The maps show the WAIS at its smallest **(b)** and largest **(c)** extents of the past 1 Myr. These occur at 205 and 625 kyr B.P., respectively. The modern grounding line is shown for comparison. The maps are colored to show how much thinner or thicker the ice sheet was at these times relative to present. **(e-s)** the relationship between WAIS mass and local ice thickness at candidate drill sites. Each point represents a single 5000 year model timestep and is colored to distinguish ice sheet-behavior during the late Pleistocene (blue: 0.8 Myr BP - present) from the early Pleistocene (yellow: 2.58-0.8 Myr BP) and Pliocene (red: 5.0-2.58 Myr BP). Horizontal dashed lines on some plots represent complete deglaciation of the site. Note that although the vertical axes are limited to values between -1000 to 1000 m, during large deglaciations Mt Resnik and Pagano Nunatak become completely ice free, and the local ice thins up to ∼2600 m and ∼1700 m, respectively.

3.4 Evaluation of candidate drill sites

In this section we use the ice-sheet model described above and available geologic information to evaluate candidate drill sites in terms of (i) how changes in local ice levels are related to the extent and configuration of the broader ice sheet, and (ii) whether the cosmogenic-nuclide record of past exposure is likely to have remained preserved by cold-based ice cover.

3.4.1 Sensitivity of sites to deglaciation of different parts of the WAIS

During collapse episodes simulated by the ice-sheet model, the grounding line retreats rapidly over deep marine basins, and is ultimately halted once it reaches shallow water. Because further retreat can only occur slowly and in the presence of a warm atmosphere, the ice-sheet margin is commonly pinned to a narrow band that closely follows the perimeter of the highland regions (Figs. 3.1 and 3.2). This is not unique to our simulation; rather it is a robust feature of ice-sheet models forced with interglacial climates [e.g. Bamber et al., 2009; DeConto and Pollard, 2016; Feldmann and Levermann, 2015; de Boer et al., 2015; Golledge et al., 2017]. The model demonstrates that in areas that remain glaciated, thinning occurs as the grounding line approaches, but then stops once the grounding line stabilizes, even if deglaciation continues in other sectors of the WAIS. The implication of this is that the magnitude of thinning at candidate drill sites is most directly controlled by the proximity of the grounding line and the thickness of ice lost from the marine basins immediately downstream, and less by ice-sheet changes elsewhere in West Antarctica.

At sites not adjoined to large marine basins, such as the Ford Ranges and the Jones Mountains, it may be difficult to know whether subglacial evidence of past exposure resulted from large-scale WAIS deglaciation or from modest retreat of the ice-sheet margin locally. In a related way, ice thinning at the Pirrit Hills, Nash Hills, and Pagano Nunatak is likely to be controlled most strongly by deglaciation of Robin Subglacial Basin, which underlies Institute and Möller Ice Streams (Fig. 3.1). Therefore, these sites may not be as sensitive to the presence or absence of grounded ice in the much larger basins of the Amundsen and Ross Sea sectors of the WAIS. A potential caveat to this is that our simulation, as well as others using the PSU-3D ice-sheet model [e.g. DeConto and Pollard, 2016], suggests that the large marine basins deglaciate in unison, implying that evidence for deglaciation from one sector could be extrapolated to other areas in West Antarctica. At sites on the periphery of the large basins in the Ross and Amundsen Sectors (i.e. Mt. Murphy, Mt. Resnik, the Ohio Range, the Whitmore Mountains, Mt. Woollard, Mt. Johns, and the northern Ellsworth Mountains), ice levels will likely be diagnostic of whether full collapse of the WAIS has occurred in the past.

3.4.2 Magnitude, timing, and frequency of thinning

The areas where the model predicts large drawdowns, not only during the most severe interglacial periods (which occur during the Pliocene in the simulation) but also during briefer warm periods of the Pleistocene, are the most likely areas to find evidence of past deglaciation in the form of previously exposed subglacial bedrock. The two sites that exhibit the greatest and most consistent ice loss are Mt. Woollard and Mt. Johns, which thin by up to ∼800 m during the Pliocene, the early Pleistocene, and the late Pleistocene (Fig. 3.2e, i). The frequency of deglaciation at these sites is perhaps not surprising as they are located at the head of the Thwaites Glacier catchment, where (i) there is concern at present about the stability of the grounding-line [e.g. Scambos et al., 2017], and (ii) there are no major topographic obstacles to impede the grounding line until it reaches the Ellsworth-Whitmore Mountains. The large magnitude of deglaciation at these sites results from their proximity to Bentley Subglacial Trench, where more than 3 km of ice would be lost during large deglaciations. Most of the other sites in the Ellsworth-Whitmore Mountains are predicted to thin consistently and significantly during collapse episodes; however, the greatest thinning is commonly restricted to the prolonged warm climates of the Pliocene, and does not occur, or does so only rarely, during the briefer Pleistocene interglacial periods (Fig. 3.2).

Almost no thinning is predicted at Mt. Petras or the Thiel Mountains, which are not located upstream of deep marine basins that are vulnerable to deglaciation, and thus are not expected to experience dynamic thinning as a result of WAIS collapses. At Mt. Moulton, a peak ∼175 km from Mt. Petras, ice has been found in an ablation area which dates to the last interglacial period, and as far back as ∼500 kyr B.P. [Korotkikh et al., 2011; Dunbar et al., 2008; Wilch et al., 1999]. Although the presence of this ice does not require continuous glaciation of other portions of Marie Byrd Land, it is consistent with the simulation of stable ice levels shown in Fig. 3.2q. Minimal thinning is also predicted at Haag Nunataks, which is surprising because, in contrast, this site is surrounded by marine basins that deglaciate during collapse episodes. The site is unique, however, in that during simulated collapse events it is located within a small ice cap that is represented by as few as 6 grid cells (Fig. 3.2b). Unlike the majority of the WAIS, these cells exhibit high spatial variability, with adjacent cells thinning and thickening, respectively, at times (which cancel out to produce the modest response shown in Fig. 3.2h). This example serves as a cautionary reminder that model results should not be over-interpreted, especially in areas where inadequate grid resolution results in spatial patterns of thinning and thickening that do not vary smoothly.

As shown in Fig. 3.2c, one possible complication predicted by the model is modest thinning in the WAIS interior during glacial periods [Steig et al., 2001]. This is potentially important at the Whitmore Mountains, Mt. Woollard, and Mt. Johns because bedrock surfaces, covered by less than ~100 m of ice, may have been exposed not only during collapse events, but also when the ice sheet was larger. Although Mt. Resnik is also located in the region expected to thin, its summit is ~330 m below the surface [Morse et al., 2002] and would likely remain fully ice-covered. The thinning is caused by reduced accumulation over the ice-sheet interior due to the decreased ability of the cold glacial atmosphere to carry moisture. Although similar thinning has been simulated previously [e.g. Golledge et al., 2012], most models of the LGM, including ones using the PSU-3D ice-sheet model, depict thicker-than-present ice [e.g. Briggs et al., 2014]. The only existing geologic constraints come from exposure dating at Mt. Waesche and the Ohio range, sites on the margin of the region predicted to thin. These data indicate that ice was modestly thicker at ~10 kyr B.P. [Ackert et al., 1999, 2007]; however, because this is several thousand years after accumulation rates began to rise in West Antarctica [Fudge et al., 2016], the data do not preclude thinner ice prior to ~10 kyr B.P. Although lower ice levels during glacial periods could complicate the search for evidence of past ice-sheet collapse, determining whether ice levels in the WAIS interior were, in fact, lower during the LGM would be significant in its own right. Because thinning in the interior is expected to be less than ~200 m (Fig. 3.2c), it would likely be possible to drill to deeper depths to encounter bedrock that may have only been exposed during collapse episodes.

3.4.3 Preservation of subglacial bedrock surfaces

The ice-sheet model could, in theory, be used to predict erosion at candidate drill sites; however, the 40 km grid resolution is too coarse for this purpose, given that drill sites will likely be located near nunataks where topographic relief is high. Even if the model was run at higher resolution, insufficient knowledge of the geothermal heat flux and other factors that influence basal conditions would preclude accurate erosion predictions. Instead we use the model as a guide to the relationship between three factors: ice thickness, surface velocity, and basal velocity (Fig. 3.3). Thickness and surface velocity are known or easily measured, while basal velocity, a strong indicator of erosion or preservation, is generally unknown or difficult to infer from measurements. Figure 3.3 shows that at the depths of interest for subglacial drilling in West Antarctica (up to ~1 km), significant glacial erosion is unlikely in areas where the surface velocity is less than ~10 m yr^{-1}. Such areas are common in the ice-sheet interior, as well as in some areas near the margin (Fig. 3.1). This result is consistent with other ice-sheet model experiments investigating the distribution of subglacial erosion in Antarctica [Jamieson et al., 2010].

Although slow flowing ice is present near many of the candidate drill sites shown in Fig. 3.1, the lowest velocities occur at the ice divides in the interior, near sites such as the Whitmore Mountains and Mt. Woollard. At these interior sites, where (i) surface temperatures are very low, and (ii) ice either thickened modestly during glacial periods [Ackert et al., 2007, 1999; Section 3.5] or potentially thinned in some areas (Fig. 3.2), subglacial drill targets, to depths of at least a few hundred meters, have likely remained continuously frozen. This is supported by field observations and exposure dating at the Pirrit Hills, Ohio Range, Nash Hills, and Whitmore Mountains [Mukhopadhyay et al., 2012; Ackert et al., 2007; Section 3.5] which show that bedrock surfaces near the modern ice level are commonly weathered and have exposure ages of hundreds of thousands of years, implying that preserved bedrock surfaces likely extend below modern ice levels.

Sites near the modern ice-sheet margin, such as Haag Nunataks, Mt. Murphy, and the Jones Mountains, are predicted to thicken by up to ~800-1000 m during glacial periods (Fig. 3.2), which suggests that bedrock surfaces there may be vulnerable to erosion beneath thick ice that is sliding at its base. Geologic constraints on former highstands are not available at these sites; however field observations from a site near Mt. Murphy indicate that ice was at least ~300 m thicker than present during the LGM [Johnson et al., 2008]. Of all the candidate sites that are located near the coast, the most extensive investigation of former ice cover has been conducted at the Ford Ranges [Stone et al., 2003; Sugden et al., 2005], a group of peaks which extend ~100 km inland from the modern grounding line (Fig. 3.1) and span multiple grid cells in the ice-sheet model. The model predicts moderate thickening during glacial periods at the upstream edge of the Ford Ranges (Fig. 3.2s), but considerably more near the modern grounding line (up to ∼900 m; not shown in Fig. 3.2), which is consistent with geologic constraints on LGM ice levels [Stone et al., 2003]. Sugden et al. [2005] reported evidence of wet-based glacial erosion on the lower flanks of many of the peaks in the Ford Ranges, especially those closest to the modern grounding line. Therefore, if uneroded subglacial bedrock surfaces exist here, they will most likely be found at shallow depths near the inland peaks, where past thickening was more limited and ice velocities are lower.

In contrast to the evidence for glacial erosion, it should be noted that other sites near the ice-sheet margin, such as the Pensacola Mountains (Fig. 3.1), show evidence for surface preservation by cold-based ice cover [Balco et al., 2016; Bentley et al., 2017]. Additionally, radar data over ice rises around the perimeter of Antarctica indicate that the majority of them are currently frozen to their beds [Matsuoka et al., 2015]. Although this was not necessarily the case during past glacial periods, the radar data suggest that cold-based ice may, in fact, be common near slow-flowing areas of the ice-sheet margin. Taken together, these observations indicate that although preserved subglacial bedrock surfaces likely exist at some coastal sites, it may be challenging to predict their locations with confidence.

3.4.4 Bedrock lithology

With the possible exception of Mt. Resnik, which is fully ice covered, the sites shown in Figs. 3.1 and 3.2 all have quartz-bearing bedrock that would allow for measurements of a wide range of cosmogenic nuclides. However, at some sites, the exposed rock also includes lithologies in which the ability to make cosmogenic-nuclide measurements would be limited, or, in some cases, impossible. These sites are the Nash Hills (see Section 3.5), Mt. Petras [Spiegel et al., 2016], the Jones Mountains [Rutford and McIntosh, 2007], and Mt. Johns [Storey and Dalziel, 1987]. Drilling at these sites may therefore remain risky unless the

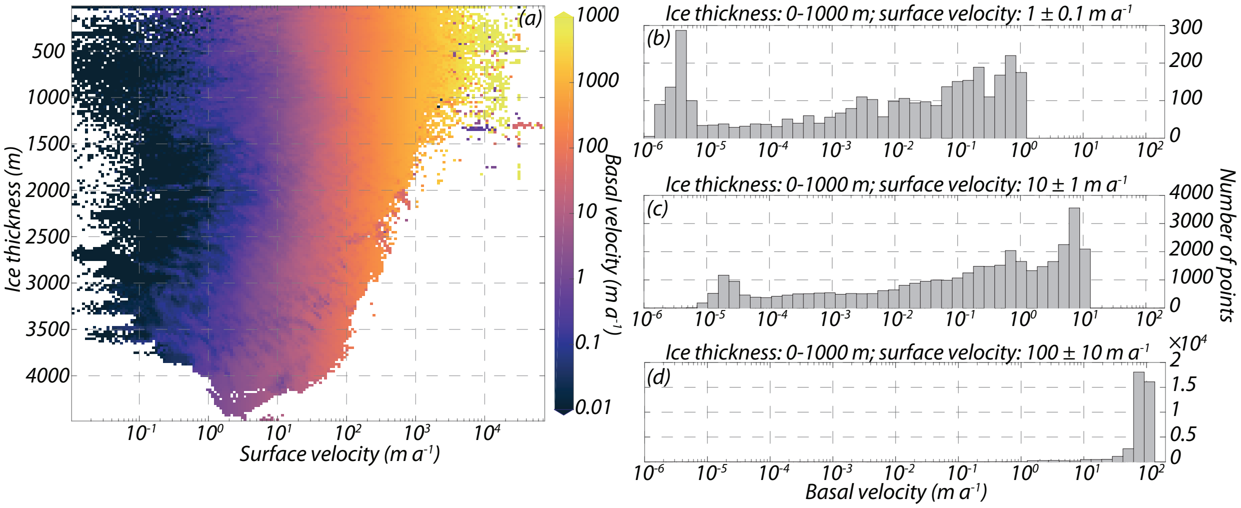

Figure 3.3: **(a)** The relationship between surface velocity, ice thickness, and basal velocity, as predicted by the 5 Myr ice-sheet model. Results for the full ice sheet are binned by surface velocity and ice thickness, and each bin is colored by its average basal velocity. This averaging hides considerable variability in the actual range of basal velocities within each bin. Therefore, in panels **(b-d)**, we provide histograms of basal velocity for points in the model where the ice is less than 1000 m thick, for surface velocities of ~1, ~10, and ~100 m/yr. At depths relevant to subglacial drilling, significant subglacial erosion is unlikely in areas where the surface velocity is less than ~10 m/yr (see Fig. 3.1).

subglacial distribution of rock types can be determined.

3.5 Drill site reconnaissance

As discussed in Section 3.2 there are advantages to drilling in the neighborhood of exposed nunataks. However, the effects of nunataks on the local ice flow and meteorology cannot be captured at the scale of the ice-sheet model used in Sections 3.3 and 3.4, introducing considerations that need to be addressed by field reconnaissance. Fieldwork prior to drilling also allows for (i) sampling of exposed bedrock to test its antiquity with cosmogenic-nuclide measurements, (ii) determining the limits of glacial-to-present ice-sheet fluctuation, (iii) examining weathering features for evidence of rock surface preservation, and (iv) locating potential drill sites using ice-penetrating radar.

In 2012-13 we visited three sites in West Antarctica - the Pirrit Hills, Nash Hills, and Mt. Seelig in the Whitmore Mountains - to evaluate their potential for subglacial drilling. These three sites were selected as lying as closely as possible to a single flowline, with the (perhaps optimistic) idea of subglacial drilling along such a transect. In the end, most reconnaissance work was carried out in the Pirrit Hills; time constraints and problems with radar equipment limited exploration at the other two sites. Nonetheless: (i) Brief reconnaissance at the Nash Hills revealed rock types not suitable for cosmogenic-nuclide measurements and complicated bedrock structure that will require geophysical surveying to locate drill sites above subglacial granite. (ii) At the Whitmore Mountains, long-lived cosmogenic-nuclide measurements (which will be described in a forthcoming publication) show evidence of prolonged exposure and limited ice-thickness changes. This, combined with the implication from the model that modest thinning may occur here during glacial periods (see Fig. 3.2, Section 3.4), discouraged us from selecting this site for initial subglacial drilling. (iii) Like the Nash Hills, the Pirrit Hills rise from the ice sheet approximately half way from divide to grounding line, where regional ice flow velocities are less than 5 m yr^{-1} [Rignot et al., 2011]. Here we were able to obtain evidence of low bedrock erosion, sizable glacial-interglacial fluctuations in ice cover, and radar profiles that revealed potential drill sites. Based on these and other factors discussed below, we chose to drill at two sites near Harter Nunatak, a minor outcrop ∼5 km north of the Pirrit Hills massif.

3.5.1 Evidence for exposure and preservation of subglacial bedrock surfaces

At the Pirrit Hills, minimally weathered glacial deposits were found up to ∼330 m above the modern ice surface, marking the LGM highstand. This is similar to the thickening predicted by the ice-sheet model (Fig. 3.2f). Despite this evidence for thicker ice, there is almost no indication of recent glacial erosion. Bedrock surfaces are oxidized, and, in places, exhibit case hardening, wind polish, and cavernous weathering pits (Fig. 3.5). Weathered surfaces occur both high on mountain flanks as well as near the modern ice surface, where they commonly

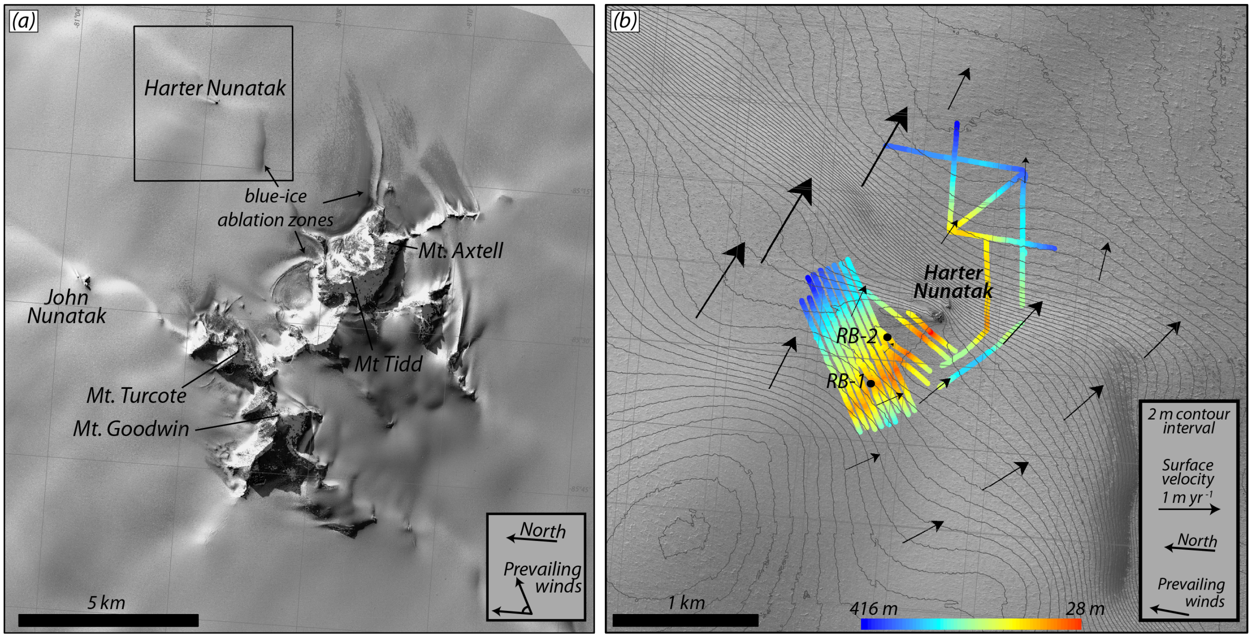

Figure 3.4: **(a)** WorldView satellite imagery of the Pirrit Hills. Black box shows the location of panel **(b)**. **(b)** Map of Harter Nunatak (center) and the surrounding area. Elevation contours are derived from WorldView satellite imagery. Colors represent ice thickness as measured with radar surveys. Arrows represent ice velocity and were measured by repeat stake surveys. The ice velocity measured closest to the RB-2 drill site is ∼0.25 m yr^{-1}. Changes in ice-surface elevation were also measured at these stakes.

intersect and appear to descend below the ice. Similar evidence for lower ice levels in the past has been found in other parts of East and West Antarctica [Mercer, 1968; Lilly et al., 2010; Mukhopadhyay et al., 2012]. Although these observations demonstrate that ice levels were lower in the past; they neither establish the magnitude nor the timing of thinning.

We collected two samples of weathered bedrock from Harter Nunatak (Figs. 3.4, 3.6) for analysis of cosmogenic ^{10}Be and ^{26}Al to determine the exposure, ice-cover, and erosional history of the nunatak. Analytical methods are described in the supplementary information. Cosmogenic nuclide data for other samples collected from the Pirrit Hills will be described in a subsequent publication. Data from these samples require minimum cumulative exposure of ∼630-650 kyr and minimum cumulative ice cover of ∼350-460 kyr (Fig. 3.6). Together with the geomorphic observations, this indicates that (i) the ice at the Pirrit Hills has been both thinner and thicker than present for prolonged periods in the past ~1 Myr, and (ii) during this time, bedrock surfaces have remained preserved by the polar climate and cold-based ice cover.

Firn temperatures in the vicinity of the Pirrit Hills are approximately -26°C and the ice is undoubtedly frozen to bedrock within a few hundred meters of the surface. Increasing ice thickness by ~330 m during the LGM is unlikely to have raised basal temperatures to near-melting. As discussed below, ice surface velocities at the site where we ultimately decided to drill are < 1 m yr^{-1}. Given the expected relation between surface velocity, ice thickness, and basal velocity shown in Fig. 3.3, this suggests that uneroded bedrock surfaces likely extend hundreds of meters below the modern ice level.

3.5.2 Local meteorology, accumulation and ablation

As noted above, mean annual temperature in the region of the Pirrit Hills is approximately -26°C. Firn depths vary from zero over blue-ice areas to at least ~36 m, as measured in access holes for subglacial drilling described below. One-year ice-motion stakes placed around Harter Nunatak in 2015 and re-surveyed in 2016 (Fig. 3.4) showed changes in the ice surface of ± 0.4 m, comparable to the height of sastrugi in the area. Given these values, accumulation in the vicinity of the nunatak appears to be low, suggesting that the firn and ice column overlying the targeted drill sites accumulated upstream, but nearby.

Regionally, snow-bearing winds descend the ice sheet and cross the Pirrit Hills from southwest to northeast. Snow has accumulated into an embankment upwind of the Pirrit Hills, which rises over a distance of ~5-10 km to the level of the col between Mt. Tidd and Mt. Goodwin (Fig. 3.4a). The ice surface drops ~600 m across this obstruction to the northeast, where the massif is bordered by a 1-2 km wide blue-ice ablation zone. This geometry results from descending warm, turbulent, foehn-like winds that ablate the ice surface in the lee of the mountains [cf. Bintanja, 1999]. Any changes in wind direction during collapse events could modify this pattern of accumulation and ablation, and potentially induce ice-thickness changes comparable to amounts expected from dynamical thinning (Fig. 3.2). Atmospheric modeling suggests that surface winds near the Pirrit Hills may vary slightly in direction and magnitude during collapse events [Scherer et al., 2016]; however a fundamental reconfiguration of accumulation and ablation areas appears unlikely.

At smaller scales around the Pirrit Hills, obstructions such as minor peaks and low bedrock ridges can reverse the spatial pattern of snow erosion and deposition, with wind scoops on the upwind side and aprons of snow and ice in the lee. The ridge shown in Fig. 3.5d exhibits a combination of such features. Their distribution around bedrock uncovered by small-scale deglaciation is difficult to predict, and could confuse cosmogenic nuclide records by shielding rock above, or exposing rock below the regional ice sheet surface. When drilling to shallow bedrock these potential complications are probably best avoided by targeting the crests of subglacial ridges.

3.5.3 Selected drill sites near Harter Nunatak

The subglacial topography northeast of the Pirrit Hills appears to be that of a large cirque, its central basin flanked by subglacial ridges descending from Mts. Tidd and Turcotte and re-emerging at Harter and John Nunataks respectively (Fig. 3.4). Regional ice flow crosses these ridges obliquely from west to east, producing steep, locally-crevassed slopes along much of their length, precluding drilling into the underlying bedrock. However, in the course of radar reconnaissance in 2013 we circled both outlying nunataks and identified a subglacial ridge extending northwest of Harter Ntk. Unlike the major ridges radiating from the Pirrit Hills massif, this ridge lies roughly parallel to ice flow and is overlain by a featureless firn surface dipping gently towards the nunatak. As shown in Fig. 3.4, the ridge is asymmetric with steeply dipping southwest and gently dipping ($\sim 20^\circ$) northeast flanks. This ridge became the chosen target for two drillholes in 2016-17. Radar methods and additional survey data are given in the Supplementary Information.

The trend of the ridgecrest (Fig. 3.4) is almost perpendicular to the prevailing wind direction. Combined with the steepness of the upwind face, this might be expected to lead to a lee-side ablation zone in any deglaciation that removed hundreds of meters of regional ice, mimicking the gross morphology of ice surfaces around the Pirrit Hills discussed above. However, smaller deglaciations that only exposed tens of meters of the ridgecrest may have left a lee-side snowbank, similar to that downwind of Harter Nunatak at the present day. In siting a shallow subglacial drillhole here, we therefore aimed to drill into crest of the ridge itself.

During the 2016-2017 summer, we planned to drill at two sites above this ridge with ice thickness of 100 m and 200 m, respectively. The target for the 100 m borehole was the ridge crest at site RB-1 shown in Fig. 3.4b. Because we were unable to image deeper portions of the ridgecrest, we sited the second borehole northeast of the crest, above the gently-dipping ridge flank. Circulation of drilling fluid in the RB-1 borehole hydrofractured the basal ice when the hole was within 10 m of the bed, forcing the borehole to be abandoned. Because the ice flow at this site is oblique to the ridge, it is possible that the basal ice is subject to extensional stresses, which could facilitate brittle failure. To maximize the likelihood of reaching the bed, we moved the drill to site RB-2 (Fig. 3.4b), which is upstream of the ridgecrest with respect to ice flow. The firn surface here dips toward the ridge, suggesting that the basal ice may be in a state of compression and more resistant to fracturing. A subglacial bedrock core was successfully recovered at this site from a depth of 150 m. If past ice levels at this site are representative of regional ice levels, the measurements on the bedrock core should provide constraints on whether Robin Subglacial Basin, below Institute and Möller Ice Streams, deglaciated in the past. Because we were unable to recover bedrock from a shallower site, the measurements will not necessarily be able to detect deglaciations in which less than 150 m of thinning occurred.

3.6 Conclusions

Measurements of cosmogenic nuclides in bedrock retrieved from below the WAIS have the potential to establish whether and when marine-based portions of the ice sheet deglaciated in the past. The potential of this method, however, requires that drill sites meet three basic criteria: (i) local ice levels must be drawn down significantly during collapse events; (ii) the subglacial bedrock must contain minerals in which useful cosmogenic nuclides can be measured; and (iii) the cosmogenic-nuclide record, which is primarily produced in the top few meters of exposed bedrock, must remain continuously protected from erosion. These criteria are also applicable to subglacial drilling projects testing whether marine basins in East Antarctica deglaciated in the past. Sites that are expected to be most indicative of past ice-sheet extent are located adjacent to deep marine basins, such as Bentley Subglacial Trench, where maximum ice loss would occur during a collapse event. Because ice levels at each of the potential drill sites discussed above are sensitive to the deglaciation of different sectors of the WAIS, subglacial samples from multiple sites will ultimately be required to fully determine the configuration of the ice sheet during past interglacial periods.

The Pirrit Hills are located in the Weddell Sea sector, midway between the grounding line and the divide. Ice-sheet modeling suggests that deglaciation of Robin Subglacial Basin induces thinning of a few hundred meters at the Pirrit Hills. Field observations and cosmogenic-nuclide measurements indicate that ice levels at this site have, indeed, been lower in the past, and multiple lines of evidence suggest that uneroded bedrock extends hundreds of meters below the modern ice surface. Ice-penetrating radar surveys revealed a gently plunging subglacial ridge extending from nearby Harter Nunatak, and, in the 2016-2017 summer, an 8 m bedrock core was extracted from the ridge from below 150 m of ice. If ice levels at the drill site are representative of the region, measurements on the core should constrain past drawdowns of grounded ice in the Weddell Sector of the ice sheet.

3.7 Acknowledgments

Support for this work was provided through US National Science Foundation (NSF) grants 1142162 and 1341728, and the United States Antarctic Program. P.S. received funding from the NSF Graduate Research Fellowship Program. We thank Maurice Conway and Paul Koubek for assistance in the field, Seth Campbell for guidance in collection and processing of radar data, Taryn Black and Mika Usher for field and laboratory assistance, and the Polar Geospatial Center for providing satellite imagery and digital elevation models.

3.8 Supplementary information

3.8.1 ^{10}Be and ^{26}Al measurements

Samples were prepared for ^{10}Be/^{9}Be and ^{26}Al/Al measurements at the University of Washington. For each sample, we crushed and sieved the rock at 250-500 microns, and purified quartz using surfactants and dilute HF etching [Kohl and Nishiizumi, 1992]. Samples were then dissolved in HF, after which total Al concentrations were measured on aliquots of the solution via inductively coupled plasma optical emission spectrometry. Be and Al were isolated using ion-exchange chromatography [Ditchburn and Whitehead, 1994], and Be and Al isotope ratios were measured at the Lawrence Livermore National Laboratory Center for Accelerator Mass Spectrometry (LLNL-CAMS). Be isotope ratios were measured relative to the ICN 01-5-4 Be standard, assigned a ^{10}Be/^{9}Be ratio of 2.851×10^{-12} [Nishiizumi et al., 2007]. Be-10 and Al-26 production rates by spallation are based on the global calibration dataset by Borchers et al. [2016], adjusted for altitude and latitude using the scaling scheme of Lal [1991] and the relationship between Antarctic air pressure and elevation [Stone, 2000]. Production rates by muons are calculated using the method of Heisinger et al. [2002a,b].

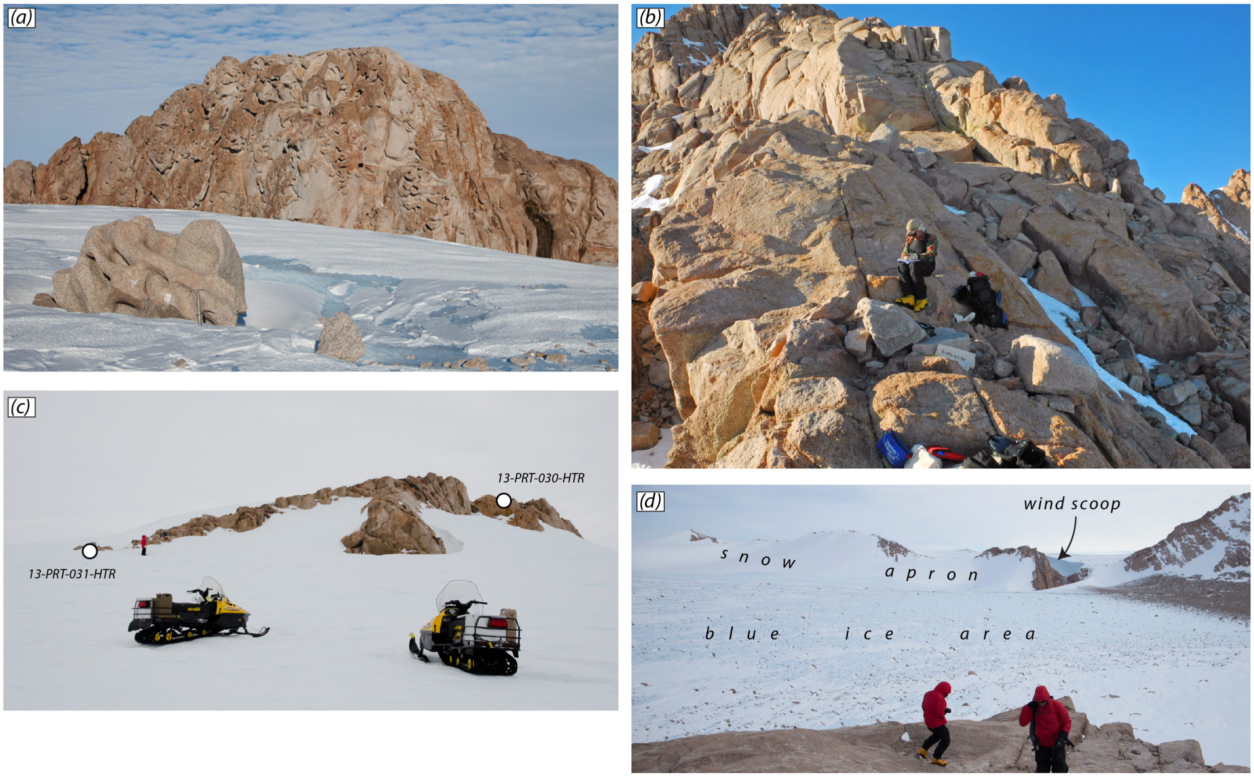

Figure 3.5: **(a)** Bedrock ridge located southeast of Mt. Axtell at the Pirrit Hills (Fig. 3.4). The granite is oxidized and displays large cavernous weathering pits (ice axe in foreground for scale). Such weathering features are common at the Pirrit Hills, both on higher mountain flanks and intersecting the modern ice surface as shown here. **(b)** Photo looking up the NE ridge of Mt Axtell. Glacially-deposited boulders rest on the more oxidized bedrock of the ridge. The depositional limit is ∼15 m above the boulders in the foreground. **(c)** Photo of Harter Nunatak, showing the location of bedrock samples collected for cosmogenic-nuclide measurements. **(d)** Back side of the bedrock ridge shown in panel A. The ridge is orthogonal to the surface winds. Ice levels on the upwind side of the ridge are ∼90-130 m higher than at the blue-ice ablation zone in the lee. The ridge is directly flanked by a wind scoop on its upwind side (not visible in panel **(a)**) and a snow apron on its downwind side.

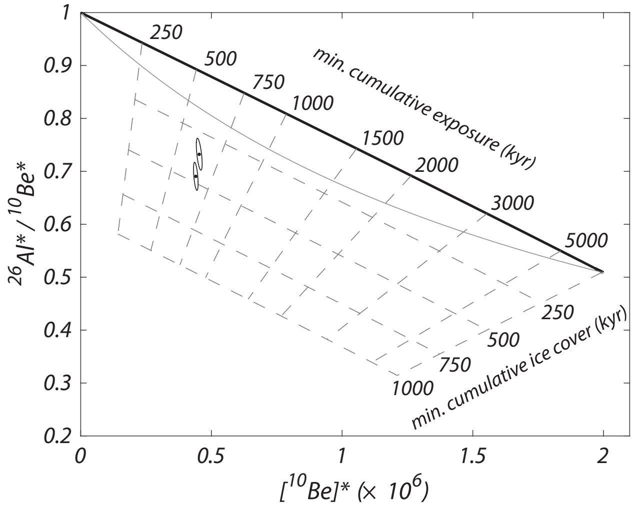

Figure 3.6: ^{10}Be and ^{26}Al data for the bedrock samples from Harter Nunatak shown in Fig. 3.5c. Nuclide concentrations are normalized to the surface production rate for each sample ($N^* = N/P$, where N is the ^{10}Be or ^{26}Al concentration and P is the local production rate of that nuclide). Ellipses represent 1 σ uncertainty regions. Continuously exposed and uneroded surfaces will plot along the black line near the top. Continuously exposed and eroding surfaces will plot between the black line and the solid gray line. Samples plotting below the solid gray line, such as those from Harter Nunatak, require at least one episode of ice cover following prior exposure. Dashed contours show lower limits on the cumulative exposure and cumulative ice cover experienced by the samples.

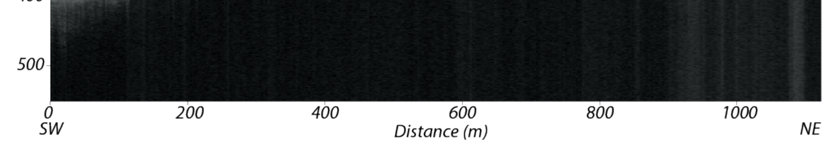

Figure 3.7: Unmigrated radar profile collected with the CReSIS accumulation radar showing the location of the 150 m RB-2 borehole to the bed. Profile is oriented perpendicular to the ridge.

Sample	Latitude	Longitude	Elevation (m)	Thickness (cm)	Density (g cm^{-3})	Horizon correction	[Be-10] (10^5 atoms g^{-1})	[Al-26] (10^5 atoms g^{-1})
13-NTK-030-HTR	-81.10278	-85.14707	1296.8	3.25	2.53	0.999	75.2 ± 1.3	384.9 ± 8.8
13-NTK-031-HTR	-81.10242	-85.14913	1290.1	1.75	2.58	0.998	73.6 ± 0.97	354.9 ± 7.8

Table 3.1: Sample information and cosmogenic-nuclide concentrations. Errors ($\pm 1\sigma$) include laboratory procedural uncertainties and individual AMS measurement errors.

3.8.2 Ice-penetrating radar surveys

We used a radar built by the Center for Remote Sensing of Ice Sheets (CReSIS) with a center frequency of 750 MHz. This radar has a cross-track antenna array consisting of two widely-spaced transmitters and eight receivers designed to identify and locate off-nadir reflections. After processing, a full tomographic reconstruction of the subglacial topography was constructed. However, prior to the 2016-17 subglacial drilling season at the Pirrit Hills, ice-thickness errors were discovered in this reconstruction, and so the bed at the drill site was re-surveyed with a Geophysical Survey Systems Inc. (GSSI) SIR-4000 control unit and a 100 MHz monostatic transceiver. These data are shown in Fig. 3.4b. The survey consisted of parallel lines spaced 50 m apart and oriented obliquely to the subglacial ridge, as well as other exploratory lines around Harter Nunatak. The survey was conducted by towing the antenna on foot at a pace less than 0.5 m $\sec^{-1}$. The data were processed using GSSI RADAN software. Distance and elevation corrections were applied to the data. To reduce noise, the data were stacked and a bandpass filter was applied. To calibrate radar wave propagation velocities and thereby improve ice-thickness estimates, we measured firn density to a depth of 38 m and used the relationship of Kovacs et al. [1995] to estimate how the real dielectric constant varied with depth. We extrapolated the depth-density relationship to deeper depths by fitting the data using a firn-densification model [Herron and Langway, 1980]. Drilling at the RB-2 site (Fig. 3.4b) encountered the bed at a depth of 150 m, confirming ice-thickness estimates from radar surveys of 152 ± 10 m.

3.8.3 Strain and accumulation measurements

Sixteen stakes were arranged in a grid around Harter Nunatak, and two additional stakes were placed over the subglacial ridge (Fig. 3.4b). Stakes were installed and surveyed in December 2015, and measurements were repeated in December 2016. Stake positions were surveyed with a Trimble 5700 GPS receiver with a Zephyr Geodedic antenna. No base station was used for the first survey; the second survey was able to use a POLENET GPS station located on Harter Nunatak as a base station. Mean velocity uncertainty is 0.23 m yr^{-1}.

Change in snow surface height was measured at each stake. Over the one-year period, height change varied from -39 cm yr^{-1} to +43 cm yr^{-1}, with a mean of -5 cm yr^{-1}. There is no apparent spatial pattern to the results, which are comparable to the amplitude of sastrugi in the area.

Chapter 4

MIOCENE TO HOLOCENE GLACIAL HISTORY OF WEST ANTARCTIC NUNATAKS

Authors Perry Spector, John Stone, Greg Balco, Mika Usher, Taryn Black, Trevor Hillebrand, Nicolas Young, Joerg Schaefer

ABSTRACT We describe glacial-geologic observations and cosmogenic-nuclide measurements from three isolated groups of nunataks in West Antarctica: the Whitmore Mountains, Nash Hills, and Pirrit Hills. Our objectives are to investigate (i) the development and preservation of alpine landscapes at these sites, and (ii) past ice-level fluctuations on timescales ranging from thousands to millions of years. Alpine landscapes at these sites developed more than ~12.3 Myr B.P., likely during warm climates of the mid-Miocene. Topographic benches at the Pirrit Hills are vestiges of cirque floors, and they also formed during or prior to this time. These benches lie near a trimline; ice levels do not appear to have reached this limit within the past several million years. This trimline may be an extension of a prominent erosional trimline that has been mapped throughout the Ellsworth Mountains. Saturated concentrations of cosmogenic ^{26}Al and ^{10}Be in bedrock surfaces from the Whitmore Mountians require extremely low weathering and erosion rates during the early-middle Pliocene, a time when it is hypothesized that the West Antarctic Ice Sheet disappeared. By analogy to similarly ancient landscapes in the Dry Valleys, this implies that the West Antarctic Ice Sheet is unlikely to have fully deglaciated during the early-middle Pliocene.

Glacial deposits and ^{26}Al/^{10}Be ratios of bedrock samples show that the lower flanks of the Pirrit Hills have been repeatedly covered by cold-based ice during Pleistocene glacial periods. In contrast, there is no evidence for higher ice levels at the Whitmore Mountains; however

brief episodes of thicker ice cannot be ruled out. At these sites, weathered bedrock surfaces containing very high cosmogenic-nuclide concentrations intersect the modern ice level, implying lower ice levels in the past. At the Pirrit Hills, located closest to the ice-sheet margin, this must have occurred during past interglacial periods, while at the Whitmore Mountains, which are located at the divide, this primarily occurred during Pleistocene glacial periods as well as during pre-Pleistocene times. During the last ice age, ice thickened at the Pirrit Hills by ∼330 m, which appears to be relatively representative of at least some prior Pleistocene highstands. The most recent highstand was sustained until at least ∼14 kyr B.P., and the majority of the thinning to the modern ice level has occurred since the mid-Holocene.

4.1 Introduction

Reconstructing the evolution of the West Antarctic Ice Sheet (WAIS) to its present-day configuration is important for predicting the ice sheet's future behavior and contribution to sea level. Although geological, marine, and glaciological data document how the ice sheet has receded from its maximum configuration during the last ice age, there are few direct observational constraints on ice thickness and extent for previous time periods. In this paper, we describe glacial-geologic observations and cosmogenic-nuclide measurements from three nunatak groups in the interior of West Antarctica: the Whitmore Mountains, Nash Hills, and Pirrit Hills (Figure 4.1). Although small, these sites provide the only constraints on the glacial history within a large area of West Antarctica. The primary objectives of this paper are to investigate (i) the development and preservation of alpine landscapes at these sites, and (ii) past ice-level fluctuations, both on thousand to million year timescales.

4.2 Field sites and glacial geology

The Whitmore Mountains and the Nash and Pirrit Hills are granitic peaks which lie along a transect from the divide to midway down the flank of the ice sheet (Figure 4.1). The

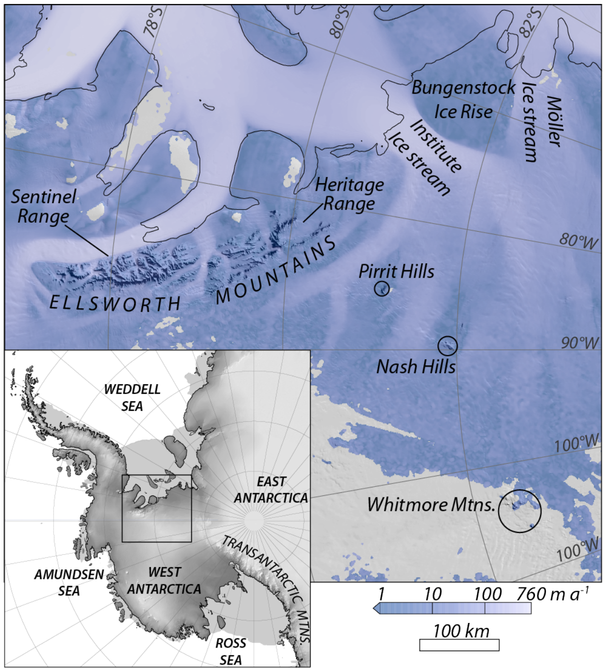

Figure 4.1: Map of West Antarctica and the region around the Pirrit Hills, Nash Hills, and Whitmore Mountains. Ice surfaces are derived from the RAMP2 DEM [Liu et al., 2001] and the MODIS mosaic [Haran et al., 2013], ice velocities are from Rignot et al. [2011], and the grounding line location is from Mouginot et al. [2017].

Whitmore Mountains emerge at an elevation of ∼2200 m from the divide between the Ross and Weddell Sea sectors. The Nash and Pirrit Hills are located at elevations of ∼1600 and ∼1300 m, respectively, in slow-flowing areas of the Institute Ice Stream catchment. We visited these sites in the summer of 2012-2013. The majority of time was spent at the Pirrit Hills; one day of fieldwork was spent at each of the other sites. The Pirrit Hills were again visited during the 2016-17 summer.

4.2.1 Pirrit Hills

The Pirrit Hills consist of a few major and several minor peaks, linked by arêtes and buttressed by steep spurs (Figure 4.2). The spurs divide cirque basins with steep headwalls; cirque floors are concealed by the present-day ice sheet.

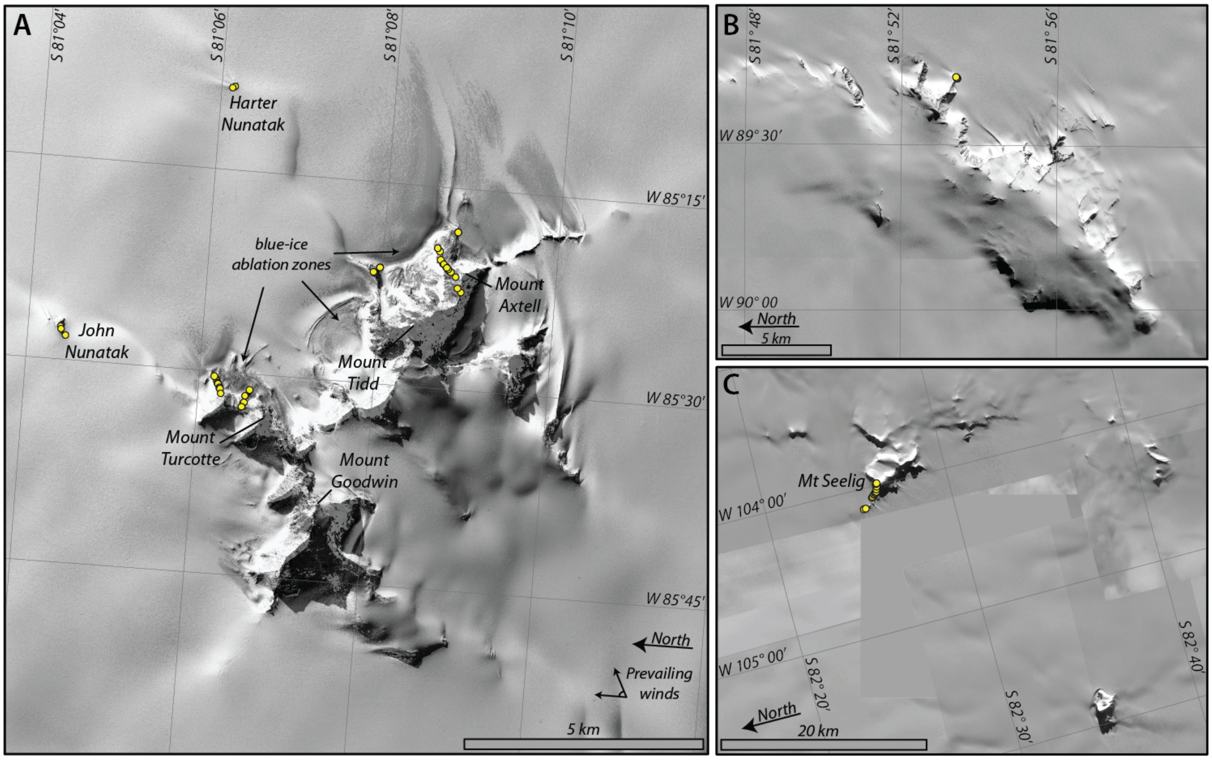

Figure 4.2: WorldView satellite imagery (copyright DigitalGlobe, Inc.) of (A) the Pirrit Hills, (B) the Nash Hills, and (C) the Whitmore Mountains. Yellow circles show the locations of rock samples.

Katabatic winds flow from SW to NE over these mountains and have deposited a ramp of snow on their upwind side that rises over a distance of ~5-10 km to the saddle between Mt. Tidd and Mt. Turcotte (Figure 4.2). Northeast of here, where the winds are forced to descend, warm, and become turbulent, there is a ~1-2 km wide blue-ice ablation zone, which sits ~600 m below the saddle. The ablation is compensated by upward ice flow, which transports englacial debris to the surface where it accumulates in sheets and moraine ridges. The debris onlaps the base of the mountains, a result of ice-sheet thinning during the late Pleistocene. Sparse deposits occur on the narrow bedrock ridges of Mts. Axtell, Tidd, and Turcotte that rise above the modern ablation zone. The highest deposits were found on the NE ridge of Mt. Axtell, ~330 m above the modern ice surface (Figures 4.3 and 4.4A). The deposit is more abundant here than lower on the ridge, with debris covering most of the area, albeit limited, where accumulation is possible. The deposits are typically lightly weathered, in contrast to the more heavily-weathered bedrock on which they rest. They consist of lithologies found at the Pirrit Hills, implying short transport distances prior to deposition, which is consistent with the limited evidence for englacial transport shown by many clasts.

Bedrock surfaces below this limit, as well as on the upper mountain flanks, are typically oxidized, and case hardening, wind polish, and weathering pits are common (Figure 4.4A). Surfaces high in the Pirrit Hills generally display more advanced stages of weathering, however, in some places this distinction is subtle. Weathered bedrock is common near the modern ice level, and there are several locations where oxidized surfaces with cavernous weathering pits intersect and appear to descend below the surface (Figure 4.4C). Above the depositional limit, evidence for recent glacial erosion is absent, while below there are isolated instances of anomalously fresh joint surfaces, which suggest bedrock slab entrainment by past ice cover (Figure 4.15).

At the Pirrit Hills, almost all of the exposed bedrock is steep, however, there are two benches on opposite sides of the Hills which display relatively subdued topography. One is directly below the summit of Mt. Axtell (a subsidiary peak of Mt. Tidd; Figure 4.3), the other is located on the buttress west of Mt. Goodwin (Figure 5). As shown in Figure 4.13, the benches have concave forms and are, in fact, vestiges of former cirque floors that are missing most of their headwalls and flanks. We describe these features in more detail below, and in Section 5.2 we discuss their relation to a prominent trimline in the Ellsworth Mountains to the north.

Figure 4.3: Photographs of Mts. Axtell and Tidd at the Pirrit Hills. Top panel shows the view from the northeast. Mt. Tidd is the high peak. Mt. Axtell is the small peak that rises from the bench; it is concealed by the two highest circles. Circles show the location of bedrock and erratic samples. The ridge where we sampled and the steep skyline ridge below the bench have considerably smoother profiles than the ridge between the bench and Mt. Tidd. Patches of glacial debris are visible at the base of the mountains where they overlie stagnant ice. Lower panel shows the view of Mt. Axtell and the bench from the summit of Mt. Tidd. Numbers correspond to sample names in the format "13-NTK-XXX-PRT". Sample 13-NTK-013-PRT was collected from the upper limit of glacial deposits.

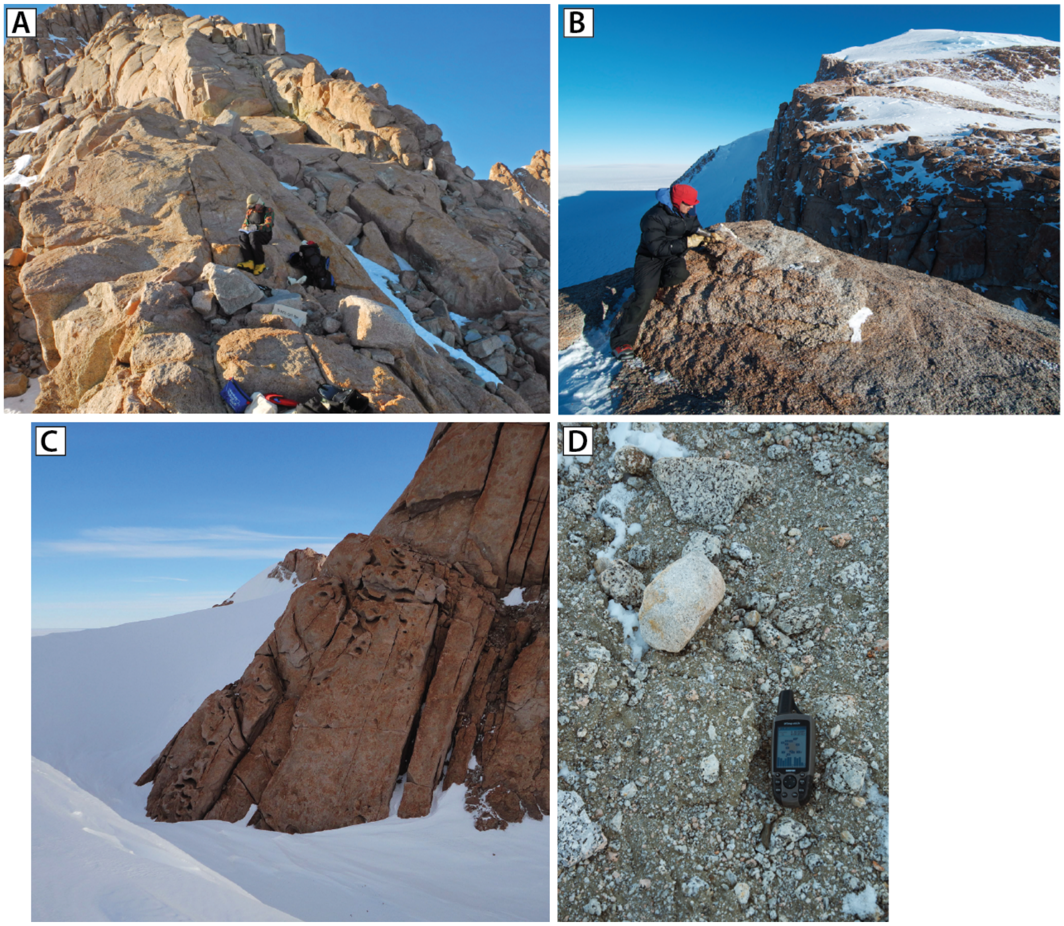

Figure 4.4: (A) View looking up the NE ridge of Mt. Axtell, Pirrit Hills. The granite ridge crest is generally a few meters wide, oxidized, and, in places displays evidence of granular disintegration and exfoliation. The depositional limit is ∼15 m above the bounders in the foreground. The lightly weathered, flat-topped boulder below the geologist is sample 13-NTK-019-PRT; bedrock sample 13-NTK-012-PRT was collected a few meters above and left of the geologist. (B) View looking up the NW ridge of Mt. Seelig in the Whitmore Mountains. Sample 13-NTK-041-WHT (236 m height) was collected from the bedrock knob in the foreground. The surface has patches of heavy oxidation and has weathered by granular disintegration. The sites of other bedrock samples are visible in the background near the cliff edge. (C) Oxidized granite of John Nunatak, Pirrit Hills, displaying cavernous weathering pits that appear to descend below the ice surface (foreground outcrop is ∼10 m wide). (D) Glacial till from Mt. Seelig (handheld GPS visible in lower right of image), composed of gravel- to cobble-sized clasts embedded in fine-grained material. Although the majority of the clasts are granitic, dark metasedimentary clasts are also present (not shown). The light-colored granite cobble is sample 13-NTK-046-WHT.

The Axtell bench is composed of two cirque basins bisected by the ridge of Mt. Axtell, while the Goodwin bench is composed of a single basin (Figure 4.13). These surfaces are truncated on most sides by steep cliffs, which, in turn, are the headwalls of other, lower elevation cirques that have been largely engulfed by the modern ice sheet. The steep ridges descending from these benches have relatively smooth profiles (Figures 4.3, 4.5, and 4.6). The only exception is the small ridge shown in the lower right of Figure 4.5 which consists of three broad crenulations. In contrast, the ridge linking the Axtell bench with Mt. Tidd displays several sharp pinnacles (Figure 4.3), and the ridge rising from the Goodwin bench has a serrated crest with delicate spires, the tallest of which we estimate to be ∼5-7 m in height (Figure 4.6). Glacial deposits are absent on the benches, and the bedrock surfaces are the most heavily weathered of any observed at the Pirrit Hills. The granite is oxidized, and in places exhibits gritty exfoliation sheets, case hardening, and delicate tafoni structures. Grus and/or felsenmeer has accumulated in low-lying areas between joint-bound bedrock blocks that have rounded into knobs and ribs (Figure 4.17).

Figure 4.5: Aerial view of Mt. Goodwin from the northwest. The gently-sloping bench is visible on the right side of the image. The apparent white skyline consists of cloud banks.

4.2.2 Nash Hills

The Nash Hills form an elongate, southeast-facing scarp from which sharp spurs project to the southeast and divide cirque basins (Figure 4.2). Most of the topography is covered by

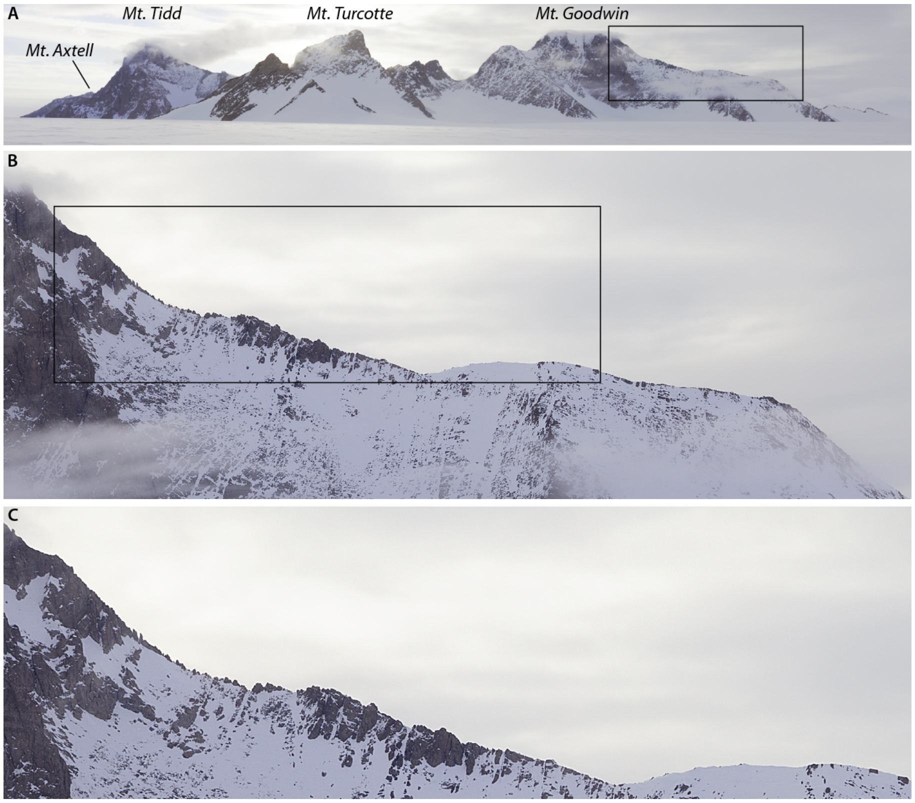

Figure 4.6: (A) View of the Pirrit Hills from the northwest. Panels B and C show the smooth skyline of the Goodwin bench and the ridge below, in contrast to the serrated ridge above the bench. The tallest pinnacles are estimated to be 5-7 m in height.

the modern ice sheet. We briefly visited the tips of two spurs located a few kilometers south of S 81°52' (Figure 4.2). As shown in Figure 4.7, one of the spurs has a coarsely-rounded form on the scale of tens of meters. Evidence of recent glacial erosion was not observed. Bedrock surfaces, down to the modern ice level, are weathered and vary from gritty to smooth, resulting from granular exfoliation and wind polishing. The more northern of the two spurs (Figure 4.2) adjoins a small ablation zone where glacial debris is accumulating at present. This debris onlaps the tip of the spur and extends at least 60 m above present ice levels (higher elevations were not visited). The debris was not examined in detail, but it appears to be considerably less weathered than the bedrock surfaces on which it rests.

Figure 4.7: The tip of the southern of the two spurs visited at the Nash Hills, where bedrock samples were collected.

4.2.3 Mt. Seelig, Whitmore Mountains

The Whitmore Mountains are a group of largely snow covered peaks organized in a semicircular pattern (Figure 4.2). Cirques and arêtes are perceptible but, as with the Nash Hills, most of the landscape has been engulfed by the present-day ice sheet. We briefly visited the northwest ridge of Mt. Seelig (Figures 4.2 and 4.8), where heavily weathered bedrock surfaces are superimposed on the alpine landscape. The bedrock surfaces are most akin to surfaces found on the upper flanks of the Pirrit Hills. The granite is oxidized, displaying weathering pits, wind polish, and evidence of granular disintegration (Figure 4.4B). There is no evidence for glacial erosion since the development of the weathered surfaces, nor are there ablation deposits such as those described above at the Pirrit Hills. Even if ice levels were higher in the past, the absence of ablation deposits would not be a surprise as these mountains are located very close to the divide and there is little upstream area from which to source debris. The only evidence for past ice cover is a small patch (several square meters) of indurated glacial till found ~150 m above the present ice surface. The till is composed of poorly-sorted granite clasts embedded in a matrix of fine-grained material (Figure 4.4D). Some of the cobbles have coarsely-smoothed forms. Sparse metasedimentary clasts were also present in the till, and, notably, at least one was striated. Outcrops of metasedimentary rock have been documented elsewhere on Mt. Seelig and in the Whitmore Mountains [Webers et al., 1982], implying that the till could have been derived locally.

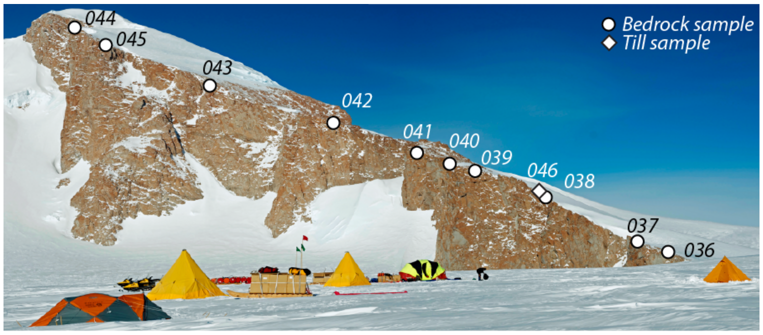

Figure 4.8: The northwest ridge of Mt. Seelig, showing sample locations. View is to the south. Numbers correspond to sample names in the format “13-NTK-XXX-WHT”.

4.3 Methods

4.3.1 Sample Collection

At the Pirrit Hills, we sampled elevation transects of glacial deposits to identify the timing and magnitude of the most recent highstand and to chronicle the subsequent thinning (Figure 4.3). Cosmogenic ^{10}Be in these samples has accumulated since their initial exposure in the ablation zones on the northeast side of the Pirrit Hills. Anomalously young exposure ages can result from post-depositional erosion of the rock surface or shielding by snow or till. To remove the possibility of post-depositional shielding, we sampled isolated deposits resting in stable positions on narrow, windswept bedrock ridges. To minimize the likelihood of erosion, we preferentially selected lightly-weathered rocks retaining evidence of glacial modification. As shown below, analysis of bedrock samples demonstrates that subaerial erosion rates at this site are very low. The majority of the glacial deposits we sampled have exposure ages older than other deposits collected nearby from higher elevations, in some cases older by hundreds of thousands of years. This indicates that much of the glacial debris at the Pirrit Hills has been repeatedly exposed during interglacial periods and recycled from older deposits. Because our sampling considerations eliminate the possibility of anomalously young ages, we interpret the youngest ages as dating deposition and the older ages as the result of prior cosmic-ray exposure.

While a single nuclide (e.g. ^{10}Be) provides a lower limit on the cumulative exposure, paired nuclides (e.g. ^{26}Al-^{10}Be or ^{10}Be-^{21}Ne) give additional information about the glacial history. In exposed rock surfaces, these nuclides are produced in fixed ratios but decay at different rates (^{10}Be $t_{1/2} \approx 1.4$ Myr; ^{26}Al $t_{1/2} \approx 0.7$ Myr) or are stable (e.g. ^{21}Ne). Because cosmic radiation is largely attenuated by thin ice cover (5-10 m), subsequent burial of a surface during a glacial highstand will halt production, causing radionuclide concentrations to decrease as a function of their half-lives. Therefore nuclide pairs including at least one radionuclide can be used to identify samples that have experienced past ice cover [Lal and Arnold, 1985; Klein et al., 1986; Lal, 1991]. This method relies on the assumption that samples have experienced minimal erosion, especially subglacial erosion, which can erase or modify the signals of past exposure and ice cover.

To examine the long-term history of exposure and ice cover, we collected samples from stable bedrock features displaying evidence for slow subaerial weathering, such as case hardening and oxidation. Where possible, we collected elevation transects of bedrock above the modern ice surface (Figures 4.3 and 4.8) in order to identify past highstands and compare exposure and ice cover at different altitudes. As for the glacial deposits, we preferentially sampled from windswept ridges and rises where the likelihood of past shielding is minimized. It should be noted, however, that some samples from Mt. Seelig in the Whitmore Mountains were collected near small ice fields (Figures 4.4B and 4.8), and past shielding of these samples may be possible.

We also measured ^{14}C ($t_{1/2} \approx 5.7$ kyr) in five samples from Mt. Axtell: the two highest glacial deposits and three bedrock surfaces above the depositional limit. Our aims were to determine (i) whether the LGM highstand was above the depositional limit, and (ii) whether the deposits were exposed prior to the LGM.

Sample elevations were determined from drift-corrected barometric measurements, benchmarked to a network of geodetic GPS observations. Elevation accuracy is typically 3-4 m based on repeat measurements. A vertically-oriented fisheye photo was taken at each sample site to measure the degree to which the sample has been shielded from the cosmic-ray flux by the surrounding topography.

4.3.2 Cosmogenic-nuclide measurements

Quartz was separated from crushed rock samples and purified using surfactants, heavy-liquid separation, and repeat etching in dilute HF. Al and Be were extracted from quartz aliquots by HF dissolution and column chromatography [Ditchburn and Whitehead, 1994] at the University of Washington Cosmogenic Nuclide Lab. For most samples, isotope ratios of Be and Al were measured at the Lawrence Livermore National Laboratory Center for Accelerator Mass Spectrometry (LLNL CAMS). Al isotope ratios for samples 13-NTK-044-WHT and 13-NTK-045-WHT were measured at the Purdue Rare Isotope Measurement Laboratory (PRIME Lab). Be isotope ratios were measured relative to the ICN 01-5-4 standard, assuming a nominal ^{10}Be/^{9}Be value of 2.851×10^{-12} [Nishiizumi et al., 2007]. Al isotope ratios were measured relative to the 01-4-2 standard, assuming a nominal ^{26}Al/Al value of 3.096×10^{-11} [Nishiizumi, 2004]. Carrier and process blanks for different sample batches had between $7.3 \pm 6.9 \times 10^{4}$ atoms ^{26}Al and $2.6 \pm 1.2 \times 10^{5}$ atoms ^{26}Al. For all samples, the blanks had less than 0.2% of the total number of ^{26}Al atoms measured. Carrier and process blanks for different sample batches had between $1.1 \pm 0.4 \times 10^{4}$ atoms ^{10}Be and $1.4 \pm 0.1 \times 10^{5}$ atoms ^{10}Be. For bedrock samples, the blanks had less than 0.1% of the total number of ^{10}Be atoms measured. For glacial deposits, the blanks had up to 4% of the total number of ^{10}Be atoms measured.

Neon was released from quartz aliquots at the Berkeley Geochronology Center by step-heating the grains in Ta packets with a 75 W, 810 nm diode laser. Neon isotopes were measured on a MAP-215 mass spectrometer using an ^{39}Ar spike to correct for the isobaric ^{40}Ar^{++} interference on mass 20 [Balco and Shuster, 2009b]. Many of our samples are slightly enriched in ^{22}Ne relative to published estimates of the atmospheric-cosmogenic mixing relation [Niedermann et al., 1993; Vermeesch et al., 2015; Schäfer et al., 1999; see Figure 4.18]. This may, in part, be because these prior estimates were based on samples with much lower ^{21}Ne and ^{22}Ne concentrations. However, some of our samples, such as those from Harter Nunatak, have much higher ^{22}Ne concentrations than would be expected from two-component mixing and appear to contain both non-cosmogenic ^{21}Ne and ^{22}Ne. In an attempt to correct for the non-cosmogenic ^{21}Ne in our samples, we subtract the mean ^{21}Ne concentration measured in a shielded rock core, recovered from beneath 150 m of ice near Harter Nunatak at the Pirrit Hills. This rock core does not appear to have been exposed at the surface in the past, as will be discussed in a forthcoming publication. We apply this correction to all of our ^{21}Ne measurements, which are on bedrock samples from either the Pirrit Hills or the Whitmore Mountains, both sites composed of Jurassic granite of the Ellsworth-Whitmore terrane [Craddock et al., 2016]. The amount subtracted is $10.4 \pm 3.0 \times 10^6$ atoms g^{-1}. This makes little difference for the samples with very high ^{21}Ne concentrations from the Whitmore Mountains and the upper portions of the Pirrit Hills, but the subtracted concentration is typically ~11-17% of measured ^{21}Ne in samples from the lower flanks of the Pirrit Hills, and in one case is 44%.

C-14 samples were prepared at Lamont-Doherty Earth Observatory following the methods of Lifton et al. [2001] and Pigati [2004], and C isotope ratios were measured at LLNL CAMS. Blanks had up to 1.7×10^5 atoms ^{14}C, and measurements of the CRONUS-A standard material were consistent with previously-reported values [Young et al., 2014].

4.3.3 Production rate calculations

We compute nuclide production rates using the method of Lifton et al. [2014], which is based on models of cosmic-ray fluxes in the atmosphere. As described below, we calibrate spallation production rates for ^{10}Be and ^{26}Al locally using samples from the Whitmore Mountains that are saturated with respect to ^{10}Be and ^{26}Al. Atmospheric pressure at sample sites is calculated using the relation between elevation and Antarctic atmospheric pressure of Stone [2000]. The method of Lifton et al. [2014] requires a time-dependent reconstruction of the paleomagnetic field, and we use (i) a dipole approximation of the reconstruction of Pavón-Carrasco et al. [2014] for the past 14 kyr, (ii) a hybrid of the GLOPIS-75 [Laj et al., 2004] and PADM2M [Ziegler et al., 2011] reconstructions for 14 kyr B.P. to 2000 kyr B.P., and (iii) the mean of the hybrid reconstruction for times prior to 2000 kyr B.P. Production rates for ^{21}Ne are calculated using the ^{21}Ne/^{10}Be production ratio of Balco and Shuster [2009b,a]. Production rates for ^{14}C are calibrated with measurements of the CRONUS-A standard material [Jull et al., 2015]. Production by muons is calculated using the method of Balco [2017]. Muon interaction cross sections for ^{21}Ne are from Fernandez-Mosquera et al. [2010].

In Section 4.5.1, we discuss previously published exposure ages from other Antarctic sites derived from ^{3}He measurements in pyroxene. We re-calculate these ages using the method of Lifton et al. [2014] and calibration data from Borchers et al. [2016]. We assume that muons do not contribute to ^{3}He production.

Reference spallation production rates for ^{10}Be and ^{26}Al based on published calibration datasets [e.g. Borchers et al., 2016] cause ^{10}Be concentrations of several of the bedrock samples reported in this paper to appear closer to saturation than the ^{26}Al concentrations of the same samples. This is an impossible result, and it suggests that the ^{26}Al/^{10}Be production ratio is overestimated. Rather than rely on published calibration datasets, we calibrate ^{10}Be and ^{26}Al production rates locally by assuming that three of the bedrock samples from the Whitmore Mountains (13-NTK-037-WHT, 13-NTK-042-WHT, and 13-NTK-043-WHT) have saturated ^{10}Be and ^{26}Al concentrations. Radionuclide concentrations saturate when production and decay are balanced (i.e., $N_{sat} = P/\lambda$, where N is the nuclide concentration, P is the production rate, and λ is the decay rate), which can only occur in samples that have experienced prolonged exposure and negligible erosion. Saturated concentrations are no longer time dependent and only provide lower limits on exposure duration. These three samples from the Whitmore Mountains have extremely high ^{10}Be and ^{26}Al concentrations (Table S1), and commonly-used scaling methods [Stone, 2000; Lifton et al., 2014] and calibration data [Borchers et al., 2016] predict that (i) these samples have ^{10}Be and ^{26}Al concentrations at or beyond saturation, and (ii) samples 13-NTK-042-WHT and 13-NTK-043-WHT, in which ^{21}Ne has been measured, have ^{21}Ne exposure ages ranging from 9.7 to 15.1 Myr. For reference, radionuclide concentrations in non-eroding rock surfaces will reach 98% of saturation in a period of time equal to $4/\lambda$, which is 8.0 Myr for ^{10}Be and 4.1 Myr for ^{26}Al. For the samples in this paper, using the local calibration changes ^{10}Be and ^{26}Al production rates by $\sim +2\%$, and $\sim -4.5\%$ relative to those calculated from the calibration datasets of Borchers et al. [2016].

4.4 Results

4.4.1 LGM-to-present ice thinning

At the Pirrit Hills, ^{10}Be exposure ages of glacial deposits range from ~1000 kyr to ~4 kyr (Figure 4.9). Although these rocks were all deposited during the last glacial cycle, 11 of the 18 samples analyzed have apparent ages greater than 67 kyr B.P. and are the result of prior cosmic-ray exposure. The remaining samples are all younger than 20 kyr B.P. The exposure age of a cobble sampled from the depositional limit on the NE buttress of Mt. Axtell, ~330 m above the modern ice surface, indicates that ice reached its highstand by 17.6 ± 0.5 kyr B.P. A boulder sampled ~14 m below the limit has an age of 14.1 ± 0.4 kyr B.P., demonstrating that ice levels persisted near the highstand for at least ~3.5 kyr, which is consistent with abundance of debris here. In comparison, the scarcity of deposits lower on the bedrock ridges suggests that thinning from the highstand occurred relatively rapidly. This thinning is constrained by only two samples from Mt. Tidd (Figure 4.9); other samples from Mts. Axtell and Turcotte appear to be pre-exposed. By 6.7 ± 0.2 kyr B.P., ice levels had lowered ~140 m from the highstand. Another 110 m of thinning occurred in the subsequent ~2.6 kyr, bringing ice levels to within 80-90 m of the modern ice surface.

As mentioned above, we measured ^{14}C in the two highest glacial deposits and three bedrock surfaces above the depositional limit to determine (i) whether the LGM highstand was above the depositional limit, and (ii) whether the deposits were exposed prior to the LGM. Concentrations of ^{14}C in the five samples are all more than 20% above saturation (Figure 4.19). It appears that there are large, unexplained measurement errors, and we do not consider these measurements further. Refer to the supplementary information for details.

At the Nash Hills, glacial deposits extend at least 60 m above present ice level, however, whether these were deposited during the LGM or a prior glacial period is unknown. We found no evidence for thicker ice in the past at the Whitmore Mountains.

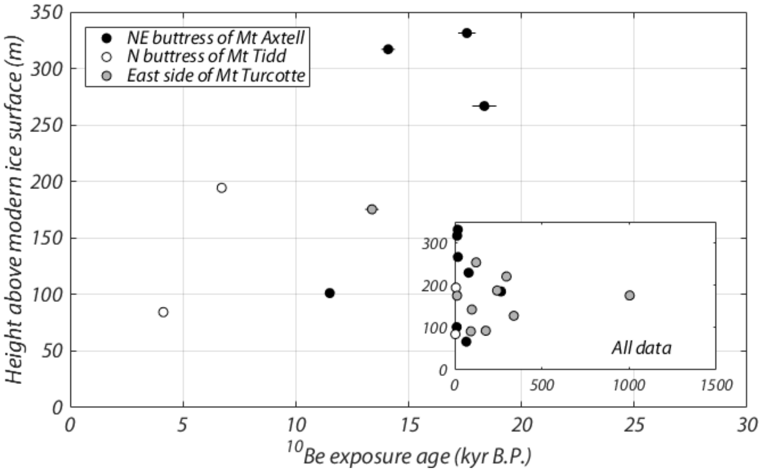

Figure 4.9: ^{10}Be exposure age of glacial deposits from the Pirrit Hills plotted against their height above the modern ice surface. Inset shows the apparent exposure age of all glacial deposits analyzed from the Pirrit Hills.

4.4.2 Long-term exposure, ice cover, and erosion

Pirrit Hills

The three samples collected from the bench of Mt. Axtell have minimum exposure ages from ^{26}Al, ^{10}Be, and ^{21}Ne of ∼2.2-7.2 Myr (Figures 4.11A) and apparent erosion rates less than 0.8 m Myr^{-1}. The large age variation given by the three nuclides suggests that ^{26}Al and ^{10}Be concentrations have reached steady states in which production is balanced by decay and very low rates of erosion, but ^{21}Ne concentrations may still be increasing (Balco et al., 2014). The samples lie near the end of the steady exposure region in Figure 4.10C and 4.10D, requiring prolonged exposure. The sample which lies slightly below this region (height of 464 m) can be explained by continuous exposure and the removal of as little as ∼5 cm of overlying material. Combined with the observation of heavily weathered surfaces, these data suggest that the bench has experienced uninterrupted exposure for the past several million years, although brief ice cover cannot be ruled out. As has been pointed out for other Antarctic bedrock samples with exposure-dominated histories [e.g. Balco et al., 2014; Mukhopadhyay et al., 2012], these data are compatible with, for example, thousands of years of cold-based ice cover during the LGM or earlier Pleistocene glacial periods, however, there is no evidence in support of such a scenario.

Most bedrock samples collected below the Axtell bench have considerably lower exposure ages (Figures 4.11A and 4.11D). Ages are limited to ∼1.3 Myr at Mt. Axtell and ∼2.3 Myr at Mt. Turcotte, and they generally decrease toward the modern ice level, as expected because most of these samples were collected below the depositional limit and have been previously ice covered. The highest sample from Mt. Turcotte and 4 samples from Mt. Axtell deviate from this trend, demonstrating that they have been preferentially eroded relative to other samples nearby. These samples could be concordant with monotonically increasing age-elevation transects if they were recently eroded by up to a few tens of centimeters, which, for one sample, is supported by geomorphic evidence (Figure 4.15). Many of the samples show disequilibrium nuclide ratios, in other words they lie below the steady exposure regions in Figures 4.10C and 4.10D, and thus require some combination of ice cover and subglacial erosion. The fact that all samples have exposure ages exceeding 0.2 Myr, combined with the geomorphic evidence for surface preservation, suggests that disequilibrium ratios are primarily due to past ice cover rather than erosion.

Although the exact chronology of exposure and ice cover experienced by samples below the Axtell bench cannot be determined, lower limits on the cumulative ice cover are provided by two-stage exposure-burial scenarios. Figure 4.11 (panels B, C, F, G, I, J) shows that both the duration and the proportion of time ice covered decrease with elevation as expected. There are large differences in ice-cover estimates from different nuclide pairs (e.g. ^{26}Al-^{10}Be versus ^{10}Be-^{21}Ne). A surface which has experienced only a single glaciation will yield identical ice-cover estimates for different nuclide pairs. Multiple cycles of exposure and ice cover will cause these estimates to diverge because radionuclides "forget" some of their prior burial during periods of exposure. These results demonstrate that the lower portion of the Pirrit Hills, especially below $\sim$150 m, has experienced many cycles of exposure and ice cover during the Pleistocene.

The ice-cover calculations assume zero erosion, which, as discussed above, is not valid for all samples. Eroded samples will have overestimated ice cover. One instance of this is the samples from the Axtell bench (above 400 m), which, despite showing no evidence for past ice cover, have non-zero values in Figure 4.11B and 4.11C. Additionally, the four samples from Mt. Axtell at heights between 230 m and 270 m have overestimated ice cover; these samples were identified above as having experienced some amount of past erosion. This implies an even greater contrast in ice cover above and below $\sim$150 m.

Nash Hills

The three bedrock samples from the Nash Hills must have experienced nearly identical glacial histories as they were collected from the same bedrock spur (Figure 4.7), all within ∼35 m of the modern ice surface. As described above, glacial deposits were found at least 60 m above the modern ice level at the Nash Hills, establishing that these bedrock samples have been previously ice covered. Two samples have ^{10}Be exposure ages of ∼1.2 Myr and ∼1.5 Myr, while the third has an age of ∼0.3 Myr (Figure 4.11K) and has clearly been eroded, which is consistent with field observations (Figure 4.16). Assuming that the other two samples have remained uneroded, their ^{26}Al and ^{10}Be concentrations indicate that they have been ice covered at least ∼7% and ∼12% of the time. These samples provide similar estimates of exposure and ice cover to bedrock samples collected near the modern ice surface at the Pirrit Hills, which is not surprising as the sites are only located ∼100 km apart.

Whitmore Mountains

The bedrock samples from Mt. Seelig in the Whitmore Mountains have extremely high exposure ages, similar to and exceeding those from the upper flanks of the Pirrit Hills (compare Figures 4.11A and 4.11N). The samples show little to no relationship between exposure age and elevation. For a given nuclide, age differences between samples results from small variations in surface preservation. Ages also vary significantly for different nuclides measured in the same sample. As mentioned above, many samples have ^{26}Al and ^{10}Be concentrations at or near saturation, which limits apparent exposure ages to ∼4.1 and ∼8.0 Myr, respectively.

These samples show no indication of higher ice levels in the past and are consistent with millions of years of uninterrupted exposure. The samples which lie slightly below the steady erosion line in Figures 4.10A and 4.10B do not require ice cover and can be explained by removal of as little as ∼5 cm of overlying rock. As for the samples from the Axtell bench, the samples from Mt. Seelig are compatible with, for example, thousands of years of cold-based ice cover during the LGM or earlier Pleistocene glacial periods.

The till found on Mt. Seelig would appear to indicate that the ice sheet has been at least $\sim$150 m thicker in the past. However, as discussed below, the till was likely deposited below a local mountain glacier or small ice cap long ago, and thus its presence does not bear on more recent variations in ice-sheet thickness. Although the till has a minimum exposure age of $\sim$1.6 Myr, it appears to be a vestige of a larger deposit which has been mostly eroded away, suggesting that it is likely much older than this age. The till has ^{10}Be and ^{26}Al concentrations implying slow erosion for a sufficient length of time to bring the concentrations to near a steady state (Figure 4.10A). If this scenario is correct, the till was deposited $3.9^{+\mathrm{inf}}_{-1.0}$ Myr B.P.

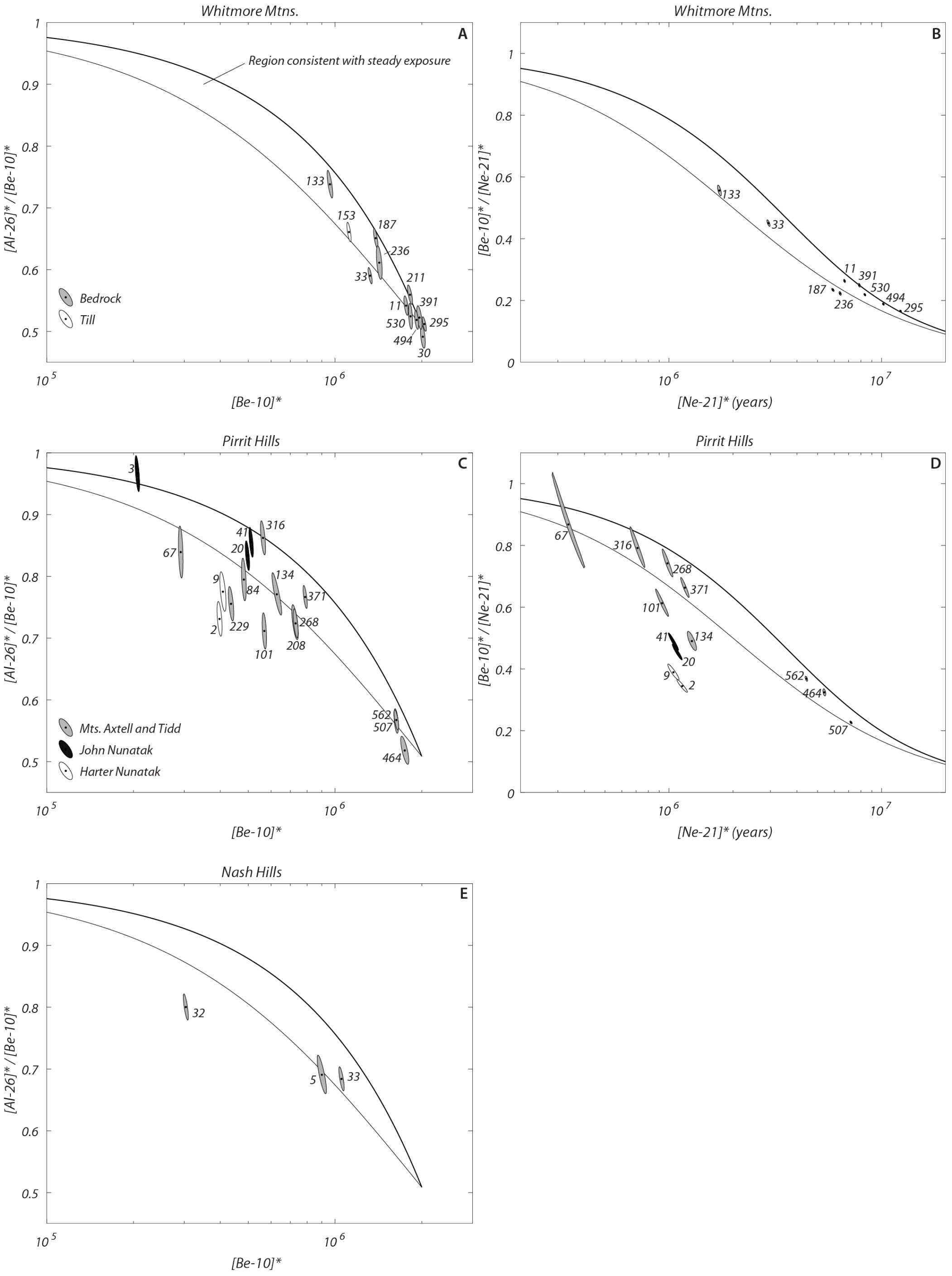

Figure 4.10: See caption on next page.

Figure 4.10: ^{26}Al-^{10}Be (left) and ^{10}Be-^{21}Ne (right) diagrams for the Whitmore Mountains (top), Pirrit Hills (middle), and Nash Hills (bottom). All data is for bedrock surfaces except for the till from the Whitmore Mountains. Nuclide concentrations are normalized to the surface production rate for each sample ($N* = N/P$, where N is the nuclide concentration and P is the local production rate), to remove the effect of differences in altitude, latitude, shielding, etc. between samples. Ellipses represent 1σ uncertainty regions and are labeled with sample height above the modern ice surface. Continuously exposed and uneroded surfaces will plot along the upper black line. Continuously exposed and eroding surfaces will plot in the region bounded by the bold line and the thinner line below. Samples plotting significantly below this region require at least one episode of ice cover following prior exposure. Dashed contours show lower limits on the cumulative exposure and cumulative ice cover experienced by the samples.

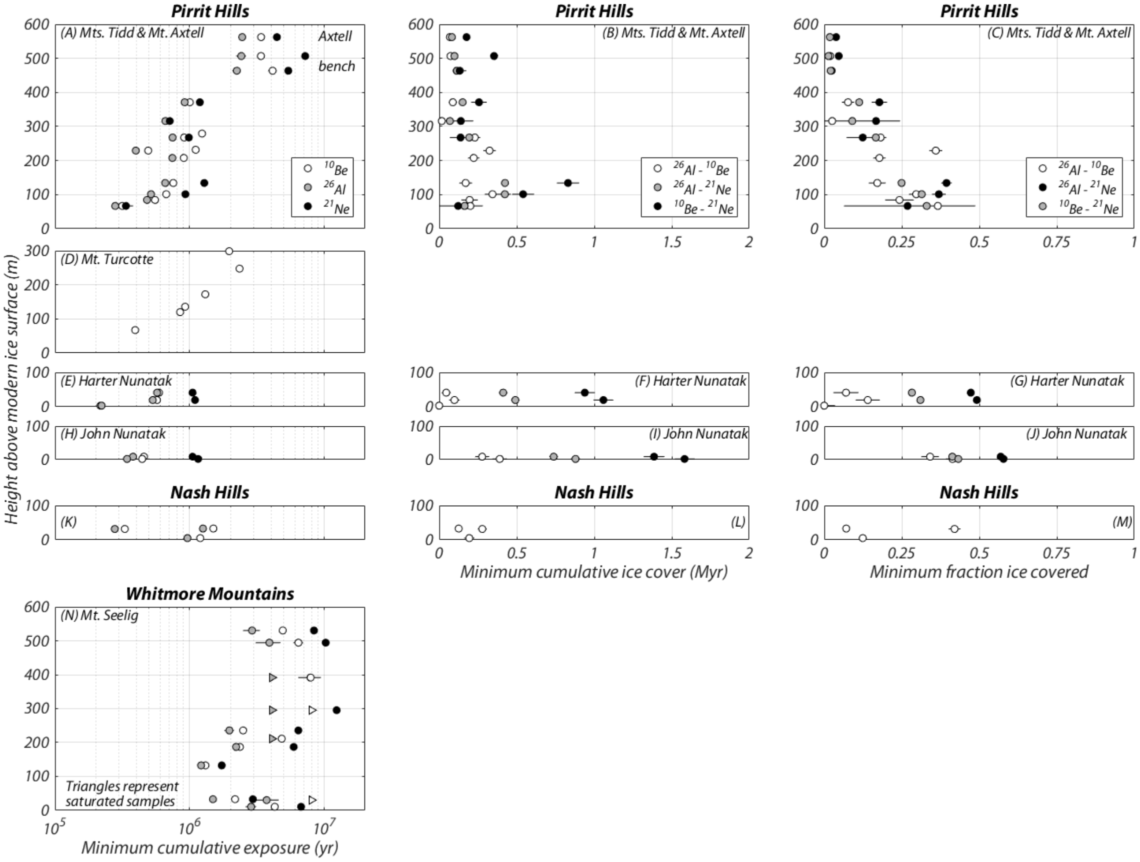

Figure 4.11: Relationships between sample height above modern ice surface and cumulative exposure age (left column), cumulative ice cover duration (middle column), and fraction of time ice covered (right column). The data plotted are for bedrock samples from the Pirrit Hills, Nash Hills, and Whitmore Mountains. Ages are lower limits on the true exposure and ice cover durations. Ice cover is calculated from two-stage exposure-burial scenarios assuming no erosion. The minor effect of post-LGM exposure has been removed for samples below the depositional limit at the Pirrit Hills. Note that for the sample from the Mt. Seelig collected 392 m above the modern ice surface, the ^{10}Be marker conceals the one for the ^{21}Ne.

4.5 Discussion

4.5.1 Mid-Miocene formation of alpine glacial landscapes

The wet-based glaciers which carved the cirques, arêtes, horns, and spurs which comprise our field sites disappeared prior to the development of the weathered bedrock surfaces that superimpose these features. The oldest of our samples from the Whitmore Mountains demonstrates that this occurred during the mid-Miocene, prior to ∼12.3 Myr B.P. Marine sedimentary records indicate that a global cooling occurred ∼14 Myr B.P. during the mid-Miocene [Zachos et al., 2001; Shevenell et al., 2004]. In Antarctica, this cooling is supported by several lines of evidence [see review in Sugden et al., 2017], which we briefly summarize below.

Fossil organisms and pollen in terrestrial and marine sediments from sites spanning Antarctica show that a tundra environment existed during the mid-Miocene and appears to have become extinct ∼14 Myr ago, replaced by polar conditions that have persisted to the present [Lewis et al., 2008; Ashworth and Cantrill, 2004; Ashworth and Erwin, 2016; Wei et al., 2014; Warny et al., 2009; Anderson et al., 2011]. The recovered taxa suggest mean summer temperatures up to ∼5-10 °C in the Dry Valleys region prior to the cooling [Lewis et al., 2008; Warny et al., 2009]. In the Olympus Range, also located in the Dry Valleys, a shift from wet- to cold-based glaciation has been dated to ∼14 Myr B.P. [Lewis et al., 2008], and implies a cooling of ∼8 °C at this time [Lewis et al., 2007]. This is similar to the 6-7 °C cooling estimated for surface waters in the southwest Pacific [Shevenell et al., 2004].

Ice-sheet simulations forced by warm mid-Miocene climates depict a largely deglaciated West Antarctica, with wet-based glaciers and small ice caps persisting in high-altitude areas such as our field sites [Jamieson et al., 2010; Sugden et al., 2017]. Marine sedimentary records indicate that warm climates existed for at least a few million years prior to the mid-Miocene cooling [e.g. Zachos et al., 2001], which would be a sufficient length of time for alpine landforms to develop at our field sites. These considerations, combined with our results showing that nunatak landforms have remained largely, and in the case of the Whitmore Mountains, completely preserved for the past ∼12 Myr, strongly suggest that the alpine landscapes found in West Antarctica were carved during the mid-Miocene. The simplest explanation of the till from the Whitmore Mountains, which, as described above, is characteristic of wet-based glacial deposits, is that it was deposited at this time.

It is relevant to note that although the bedrock surfaces from the Whitmore Mountains provide some of the oldest exposure ages from Antarctica, other Antarctic rocks have yielded similarly old ages. Ages beyond ∼8 Myr have only been derived from measurements of stable cosmogenic nuclides in minerals which do not suffer from diffusive loss (i.e. ^{21}Ne in quartz and ^{3}He in pyroxene). Figure 12 shows that exposure ages from these nuclides, in rocks sampled from various Antarctic sites, extend up to but not beyond ∼11-13 Myr, consistent with the hypothesis of a change from wet- to cold-based glaciation during the mid-Miocene.

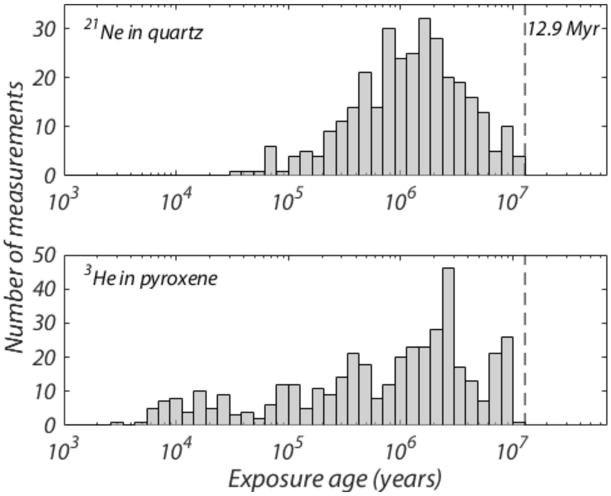

Figure 4.12: Histograms of apparent exposure age derived from measurements of stable cosmogenic ^{21}Ne in quartz (top) and ^{3}He in pyroxene (bottom) in rocks from various sites around Antarctica. The measurements have been compiled in the ICE-D: ANTARCTICA database (http://antarctica.ice-d.org/) and have been recalculated to be consistent with ages in this paper.

4.5.2 Benches in the Pirrit Hills and their relation to the Ellsworth Mountains trimline

As described above, the cirque floors which comprise the Axtell and Goodwin benches have been truncated by headwall retreat of lower-elevation cirques. The simplest explanation for this relationship is that preferential erosion of the lower elevation cirques was facilitated by a cooling climate and potentially also by isostatic uplift during the mid-Miocene or earlier times.

Since the transition from mountain glaciers to a polar ice sheet, the Axtell and Goodwin benches appear to have remained continuously ice free. Therefore, these benches or, more specifically, a level directly below them, represents a long-term trimline separating ancient surfaces above from somewhat younger surfaces below. The actual trimline height is best constrained at Mt. Axtell, where it is bounded by the base of the bench and the LGM depositional limit ∼100 m below. Older glacial deposits have been found above the LGM limit in the Heritage Range to the north [Bentley et al., 2010], suggesting that the actual trimline at the Pirrit Hills is above the depositional limit.

This trimline in the Pirrit Hills appears to be closely related to a prominent erosional trimline in the Ellsworth Mountains, and may be an extension of the same feature. The Ellsworth trimline has been discussed in detail by Denton et al. [1992], and the descriptions below are based on that work. Like the Pirrit Hills, the Ellsworth Mountains exhibit classical features of alpine glacial erosion, which, as discussed above, were likely carved during the mid-Miocene. Throughout the ranges, a trimline is commonly etched into the quartzite ridges which descend from high peaks to the modern ice surface. The trimline separates highly serrated ridgecrests above from smoothed ridges below, similar to the ridges above and below the Axtell and Goodwin benches (Figures 4.3, 4.5, and 4.6). Serrations above the Ellsworth trimline are closely spaced, up to 30 m high, and have commonly weathered into delicate spires. Relic cirque floors near the height of the trimline, such as those at the Pirrit Hills, have not been described. Below the trimline, alpine topography is generally well preserved; however, bedrock ridges commonly display coarsely-smoothed forms and striated surfaces. Glacial deposits are present near ablation zones in the Heritage Range, which comprise the southern half of the Ellsworth Mountains (Figure 4.1), but are scarce in the Sentinel Range to the north.

Trimline elevations vary smoothly over the length of the Ellsworth Mountains, a distance greater than 250 km, in a pattern consistent with a prior ice surface. In the Sentinel Range, the trimline is 400-650 m above the modern ice surface on the western side and 1300-1900 m above on the eastern side. In the Heritage Range, it is commonly higher than the mountain tops, but it has been mapped at the following heights relative to the ice surface west of these mountains: Liberty Hills (∼400 m), Soholt Peaks (∼500 m), and Enterprise Hills (∼500 m). Relative to equivalent ice surfaces at the Pirrit Hills (rather than the ablation zones to their north), the Axtell and Goodwin benches sit at heights of 300-360 m and 270-340 m, slightly lower than the trimline heights in the Heritage Range.

These similarities strongly suggest that the Ellsworth and Pirrit Hills trimlines are, in fact, part of the same feature. An obvious difference, however, is the absence of evidence for wet-based glacial erosion below the trimline at the Pirrit Hills. This difference may be reconciled by the fact that the granite bedrock at the Pirrit Hills is not expected to retain striations or smoothing as well as the resistant quartzite of the Ellsworth Mountains because of granular disintegration. Striations have, however, been observed in sedimentary rocks at Moreland Nunatak (The Polar Rock Repository), a minor peak ∼20 km west of the Pirrit Hills.

Denton et al. [1992] argue that the smoothly-varying elevation of the Ellsworth trimline, the absence of evidence for ice cover above it, and the orientation of striations below indicate that the trimline formed at or near a former ice surface. Building on this, Sugden et al. [2017] suggest that the main phase of trimline erosion occurred during the mid-Miocene, shortly following the cooling described above and the transition from small ice caps and mountain glaciers to an ice sheet covering most of West Antarctica. They reason that striations and other features of glacial-erosion, which in places occur near the height of the trimline, would require a thawed bed below thin ice near the ice-sheet margin, and that the mid-Miocene was the most recent time the climate was sufficiently warm for this to occur. They observe that some glacially-eroded bedrock surfaces and overlying deposits below the trimline in the Heritage Range have ages up to ∼4.0 Myr, which provide a lower limit on trimline erosion (the age of ∼4.0 Myr represents the sum of the minimum exposure and minimum ice-cover ages, and it has been recalculated to be consistent with samples presented in this paper). Our results from the Pirrit Hills are consistent with this hypothesis. The oldest age from below the benches is ∼2.3 Myr, which does not further restrict the age of trimline formation. Improved age constraints could likely be derived from exposure dating of the smoothed and striated bedrock surfaces which lie a short distance below the trimline in the Sentinel Range [Denton et al., 1992].

4.5.3 Limits on Pliocene weathering rates and implications for WAIS extent

The early and middle Pliocene (∼5.3-3.0 Myr B.P.) is the most recent time atmospheric CO_2 concentrations reached modern values (∼400 ppm), and, on the basis of numerous lines of observational evidence [see reviews in Haywood et al., 2009; Dowsett et al., 2010], it appears that the climate was warmer than present. Climate models, forced by mid-Pliocene boundary conditions, simulate global mean surface temperature ∼1.8-3.6 °C warmer than pre-industrial values [Haywood et al., 2013]. It has been suggested that the WAIS was absent during the early and middle Pliocene. The evidence for this largely comes from coastal records of relative sea level and from estimates of global ice volume derived from geochemical measurements on marine sediment cores [e.g. Miller et al., 2012]. There has been recent acknowledgement, however, that both of these methods carry sufficiently large uncertainties so as to prohibit robust estimates of Pliocene sea level or ice volume [see reviews in Dutton et al., 2015 and Raymo et al., 2017].

A deglaciated West Antarctica would entail a warmer and wetter climate, presumably with attendant increases in rock weathering and erosion rates. This would appear to conflict with the evidence for long-term preservation of surfaces and landscapes that date to the mid-Miocene (see discussion above). One way to examine whether these reconstructions are plausible is to ask the question: how low would bedrock surface erosion rates need to be during the early-middle Pliocene in order to produce the saturated ^{26}Al and ^{10}Be concentrations we observe at the Whitmore Mountains? To answer this question we posit the following three-stage scenario. First, by 5.3 Myr B.P. bedrock surfaces have been exposed and completely uneroded for a sufficient length of time that ^{26}Al and ^{10}Be concentrations have reached saturation. Second, between 5.3 and 3.0 Myr B.P. bedrock surfaces remain exposed but they erode steadily at a rate ϵ (g cm^{-2} a^{-1}) due to the warmer and wetter climate. Finally, between 3.0 Myr B.P. and the present, bedrock surfaces continue to be exposed, but there is zero erosion. At the end of this scenario, the nuclide concentrations N_i (where the subscript i represents either ^{26}Al or ^{10}Be) are given by the following equation:

$$N_i^* = \underbrace{\frac{1}{\lambda_i}\exp\left[-\left(\lambda_i+\frac{\epsilon}{\Lambda}\right)t_1-\lambda_i t_2\right]}_{\text{pre-Pliocene exposure}} + \underbrace{\frac{1}{\lambda_i+\frac{\epsilon}{\Lambda}}\left(1-\exp\left[-\left(\lambda_i+\frac{\epsilon}{\Lambda}\right)t_1\right]\right)\exp\left[-\lambda_i t_2\right]}_{\text{early-middle Pliocene exposure}} + \underbrace{\frac{1}{\lambda_i}\left(1-\exp\left[-\lambda_i t_2\right]\right)}_{\text{post-mid-Pliocene exposure}}$$

where λ is the decay constant (a^{-1}), Λ is the attenuation length for spallogenic production (taken to be 150 g cm^{-2}), and t_1 and t_2 are the exposure durations during and after the early-middle Pliocene, respectively. Nuclide concentrations are normalized to surface production rates ($N^* = N/P$). If we assume that concentrations can be considered saturated if they are within 2% of actual saturation ($N_{sat} \approx 0.98P/\Lambda$), then Pliocene erosion rates must have remained below 37 cm Myr^{-1} and 4 cm Myr^{-1} for saturated ^{26}Al and ^{10}Be concentrations, respectively.

These are extraordinarily low erosion rates by global standards [Portenga and Bierman, 2011], and they are incompatible with a considerably warmer and wetter climate at the Whitmore Mountains during the early-middle Pliocene. If the marine-based portions of the WAIS disappeared at this time, the Whitmore Mountains would be located within ~75 km of the coast, allowing for isostatic rebound [Fretwell et al., 2013]. Such a setting may be akin to high-elevation sites in the Dry Valleys, where there are also landscapes dating to the mid-Miocene [e.g. Sugden et al., 1999]. The fact that these sites in the Dry Valleys are located ~50-100 km from open water at the present suggests that we cannot rule out deglaciation of the marine basins of West Antarctica during the early-middle Pliocene on the basis of saturated concentrations at the Whitmore Mountains. However, the preservation of such ancient surfaces in the Dry Valleys appears to require the continuous presence of a polar East Antarctic Ice Sheet immediately to the west, which delivers cold, dry air to these sites [Marchant et al., 2013; Marchant and Denton, 1996; Denton et al., 1993]. Saturated concentrations at the Whitmore Mountains may therefore place a similar requirement on early-middle Pliocene ice in West Antarctica. If the West Antarctic marine basins deglaciated at this time, it appears likely that the Whitmore Mountains remained embedded within a remnant of the WAIS that persisted over the high topography of the Ellsworth-Whitmore Mountains. Such a scenario is, in fact, supported by most ice-sheet model simulations that are forced with Pliocene boundary conditions [Pollard and DeConto, 2009; Scherer et al., 2016; de Boer et al., 2015; Golledge et al., 2017; Spector et al., submitted]. This suggests that reconstructions depicting zero West Antarctic ice during the Pliocene [e.g. Dowsett et al., 2016] are incorrect or overly simplistic.

4.5.4 Higher and lower ice levels in the past

LGM to present changes

At the Whitmore Mountains, there is no indication of higher ice levels in the past. However, at the Ohio range, located only 280 km to the SW, exposure ages of 2 erratics collected near depositional limits indicate that the ice level was ∼125 m higher ∼13-10 kyr B.P. [Ackert et al., 2007]. This suggests that ice may have also been higher for a period during the last glacial-interglacial transition at the Whitmore Mountains.

The LGM highstand of ∼330 m at the Pirrit Hills is consistent with ice-sheet model simulations [Spector et al., submitted], which imply that the grounding line was located in the outer Weddell Sea at this time. Although the thinning history is only constrained by 4 samples (Figure 4.9), it closely matches records from the southern Heritage Range, ∼110 km to the northwest (Figure 4.1). At the Marble, Patriot, and Independence Hills, fresh glacial deposits extend up to 230-475 m above present ice levels and mark the LGM highstand [Hein et al., 2016; Bentley et al., 2010]. Exposure ages of these deposits, which have been recalculated to be consistent with samples in the paper, indicate that ice remained at or near its limit until ∼9.5-8.5 kyr B.P. and that the majority of the thinning to the modern ice level occurred between 6 and 3 kyr B.P. (compare to Figure 4.9). A notable feature of the chronologies from the Pirrit Hills and the Heritage Range is the rapid thinning to the modern ice level during the mid-Holocene and the apparent lack of change since ∼4-3 kyr B.P. This is consistent with significant changes in flow direction and the position of the grounding line, discussed below, that appear to have occurred in the Weddell Sea sector during the middle to late Holocene.

As shown in Figure 4.1, Bungenstock Ice Rise is located just upstream from the Weddell Sea grounding line ∼200-300 km from the Pirrit Hills. Radar-detected stratigraphy within the ice rise shows surface-conformable layers in the upper half of the ice column but disrupted layers below; this transition appears to mark the onset of a stable ice rise [Siegert et al., 2013]. The surface of the ice rise displays E-W oriented lineations, implying that ice from the Pirrit Hills used to flow over this feature, rather than being routed north via Institute Ice Stream as occurs at present [Siegert et al., 2013; Winter et al., 2015; see Figure 4.1]. One hypothesis for this switch is that the grounding line retreated inland of its present position and subsequently re-advanced during the late Holocene due to isostatic rebound, allowing the ice rise to re-ground [Siegert et al., 2013; Winter et al., 2015; Matsuoka et al., 2015]. There is considerable evidence in support of this scenario, both in the Weddell and Ross Sea sectors. Early work showed that Crary Ice Rise in the Ross Sea sector re-grounded ∼1.1 kyr B.P. [Bindschadler et al., 1990]. Recently, Kingslake et al. [2017] documented (i) the presence of radiocarbon in subglacial till below the Siple and Gould Coasts, and (ii) radar evidence for ice-shelf re-grounding in the Weddell Sea. These authors also reported ice-sheet model experiments which depict grounding-line overshoot and re-advance. In the Weddell Sea sector, a late-Holocene retreat-advance scenario is able to reconcile GPS-measured uplift rates and models of glacial-isostatic adjustment, which disagree when a monotonic Holocene recession is assumed [Bradley et al., 2015].

Institute and Möller Ice Streams appear to be underlain by wet, deformable sediment [Bingham and Siegert, 2007], which would allow changes at the grounding line to be rapidly propagated upstream. Therefore, retreat of the grounding line past its present position would be expected to cause dynamic thinning at the Pirrit Hills and the Heritage Range. A modern analogue of this behavior is the retreat in the Amundsen Sea sector, which has caused thinning hundreds of kilometers upstream of the grounding line in recent decades [Pritchard et al., 2012]. The rapid mid-Holocene thinning at the Pirrit Hills and Heritage Range suggests significant changes in the position of the grounding line at this time. The timing of the grounding line changes discussed in the previous paragraph are not yet sufficiently well constrained to determine whether they are synchronous with the observed thinning. The apparent absence of thinning at the Pirrit Hills and the Heritage Range during the late-Holocene is predicted by, and therefore consistent with, the grounding-line retreat-advance scenario.

Pre-LGM highstands

The absence of evidence for past ice cover on the Axtell bench strongly suggests that ice has not thickened by more than ∼430 m at the Pirrit Hills. It appears that bedrock samples below but within ∼150 of this level have been repeatedly ice covered (Figures 4.11B, C), suggesting that the LGM highstand of ∼330 m is likely to be representative of at least some prior Pleistocene highstands. Whether this amount of thickening is typical of Pleistocene glacial periods is less apparent. As mentioned above, bedrock samples near the modern ice surface (including those from John and Harter Nunataks) have spent a much greater proportion of time ice covered than samples from higher elevations (Figures 4.11C, G, J). Although this trend is expected, the difference could, in part, have resulted from lower highstands that only covered the base of the Pirrit Hills.

Lower ice levels in the past

Weathered bedrock commonly intersects and appears to descend below the modern ice surface at our field sites (Figure 4.4C), which was first recognized by Mercer [1968] as evidence for thinner ice in the past. Samples of this bedrock, collected less than 10 m above the ice, have exposure ages up to ∼1.2 Myr at the Pirrit and Nash Hills and ∼6.8 Myr at the Whitmore Mountains (Figures 4.11H, K, N), implying that ice levels have been lower than present for extended periods in the past. The amount of past thinning cannot be known without bedrock samples from below the ice.

As discussed above, it is likely that ice levels were lower than present at the Pirrit and Nash Hills during the late Holocene. Although we cannot rule out the possibility that this was the only time ice was thinner at these sites, this appears implausible. The simplest explanation for weathered bedrock surfaces with high cosmogenic-nuclide concentrations at the modern ice level is that such episodes of thinning have repeatedly occurred during Pleistocene interglacial periods.

At the Whitmore Mountains we can rule out the possibility of prolonged periods of thicker-than-present ice in the past, as discussed in Section 4.4.2. Therefore, the null hypothesis here is that the ice level has (i) never been lower and (ii) rarely, if ever, been higher than present during the past ∼6.8 Myr. The WAIS divide ice core, located ∼350 km away, indicates that accumulation rates were considerably lower for tens of thousands of years during the last glacial period than since ∼15 kyr B.P. [Buizert et al., 2015]. East Antarctic ice cores show similar patterns and indicate that reduced accumulation rates are a consistent feature of Pleistocene glacial periods [e.g. Parrenin et al., 2007]. Therefore, for the null hypothesis to be correct, these accumulation rate changes would need to be perfectly balanced by dynamic ice-thickness changes related to the position of the grounding line downstream, a scenario which appears exceedingly unlikely [Steig et al., 2001; Cuffey et al., 2016]. This strongly suggests that ice levels in the WAIS interior have commonly been lower than present during

Pleistocene glacial periods when accumulation rates were reduced [c.f. Steig et al., 2001]. The exposure age of ∼6.8 Myr suggests that ice levels may also have been lower for considerable portions of the Pliocene and earlier times.

4.6 Conclusions

Alpine landscapes at the Whitmore Mountains, Nash Hills, and Pirrit Hills were carved by mountain glaciers more than ∼12.3 Myr B.P., likely during warm climates of the mid-Miocene. Topographic benches at the Pirrit Hills, which are, in fact, the floors of former cirque basins, formed during or prior to this time. A short distance below these benches marks a trimline, above which there is no evidence for ice cover in the past several million years. This appears to be an extension of the prominent erosional trimline in the Ellsworth Mountains to the north.

These alpine landscapes have been exceptionally well preserved by the polar climate and, in some cases, cold-based ice cover. Saturated concentrations of cosmogenic ^{26}Al and ^{10}Be in bedrock surfaces from the Whitmore Mountians require extremely low weathering and erosion rates during the early-middle Pliocene, a time when it is hypothesized that the West Antarctic Ice Sheet disappeared. By analogy to similarly ancient landscapes in the Dry Valleys, this implies that the West Antarctic Ice Sheet is unlikely to have fully deglaciated during the early-middle Pliocene.

Cosmogenic-nuclide measurements in bedrock surfaces from the Pirrit Hills indicate that the lower flanks of these mountains have been repeatedly covered by cold-based ice during Pleistocene glacial periods. In contrast, there is no evidence for higher ice levels at the Whitmore Mountains; however brief episodes of thicker ice cannot be ruled out. At these sites, as well as the Nash Hills, weathered bedrock surfaces containing very high cosmogenic-nuclide concentrations intersect the modern ice level, implying lower ice levels in the past. At the Pirrit Hills, located closest to the ice-sheet margin, this must have occurred during past interglacial periods, while at the Whitmore Mountains, which are located at the divide, this primarily occurred during Pleistocene glacial periods as well as during pre-Pleistocene times. During the last ice age, ice thickened at the Pirrit Hills by ∼330 m, which appears to be relatively representative of at least some prior Pleistocene highstands. The most recent highstand was sustained until at least ∼14 kyr B.P., and the majority of the thinning to the modern ice level has occurred since the mid-Holocene.

4.7 Acknowledgements

Support for this work was provided by US National Science Foundation (NSF) grants OPP-1142162 and OPP-1341728, and the United States Antarctic Program. P.S. received funding from the NSF Graduate Research Fellowship Program. We thank Maurice Conway and Tom Schaefer for their assistance with field work. Danielle Lemmon and Jessica Badgeley assisted with lab work. Robert Finkle, Susan Zimmerman, and Tom Brown, assisted with AMS measurements. Geospatial support for this work provided by the Polar Geospatial Center under NSF OPP awards 1043681 & 1559691.

4.8 Supplementary information

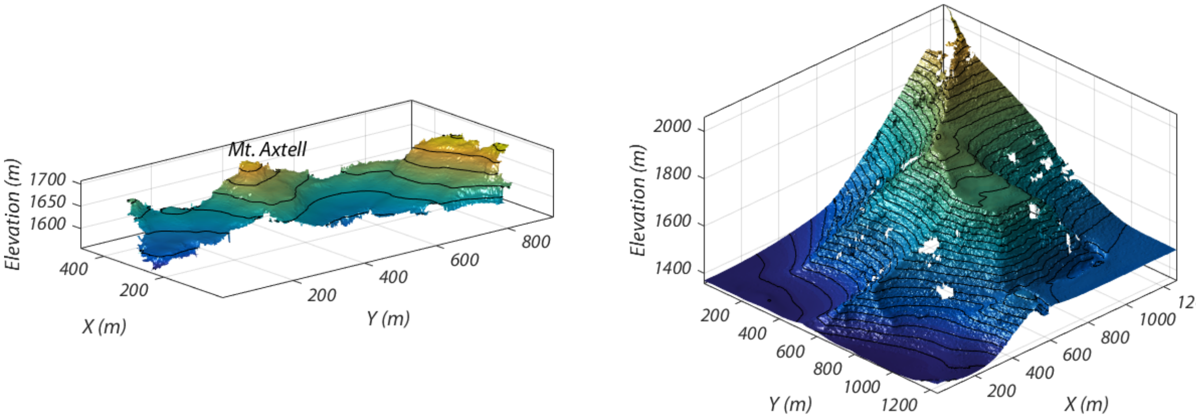

Figure 4.13: 3D renderings of the relic cirque floors which comprise the Axtell bench (left) and the Goodwin bench (right) derived from DEMs created by the Polar Geospatial Center from DigitalGlobe, Inc. satellite imagery. The top panel only shows the Axtell bench surface; the surrounding cliffs are too steep for their elevations to be calculated from stereo imagery. Contour interval in both panels is 20 m.

Figure 4.14: Photo looking north at the southern tip of John Nunatak and the location of sample 13-NTK-003-JHN (collected near the person on the right). This feature has a coarsely-smoothed form in contrast to most other bedrock features at the Pirrit Hills.

Figure 4.15: View looking up the northeast ridge of Mt. Axtell, Pirrit Hills. Sample 13-NTK-008-PRT was collected next to the white bag. The area within a few meters of the sample is less weathered than most bedrock surfaces on this ridge. Additionally, it is roughly planar and contiguous with bedrock joints, in contrast to the convex knobs and ribs seen in the foreground and background. These observations suggest removal of a bedrock slab by overriding ice.

Figure 4.16: The site at the Nash Hills where sample 13-NTK-032-NSH was collected. The bedrock was sampled next to the rock hammer. The ledge below the sample site is the edge of an exfoliation slab which used to extend and cover sample 13-NTK-032-NSH.

Figure 4.17: The concave surface of the Goodwin bench. In the foreground and midground, joint-bound bedrock blocks have been rounded into knobs and ribs. The aligned boulders are tors oriented parallel to the bedrock joints.

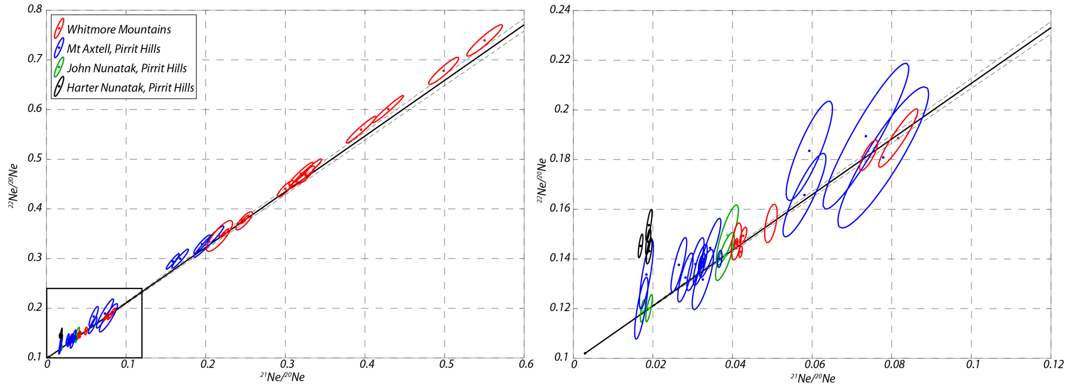

Figure 4.18: Neon isotope ratios measured in samples from the Pirrit Hills and Whitmore Mountains.

Sample information and ^{26}Al, ^{10}Be, and ^{21}Ne concentrations

This information is given in the supplement Ch4_DataTable.xlsx.

Cosmogenic ^{14}C concentrations

Full results of the ^{14}C measurements are given the supplement Ch4_C14_results.xlsx.

The ^{14}C results are unreliable for three reasons. First, the five samples all have concentrations at least 20% higher than expected saturation concentrations (Figure 4.19). There are other Antarctic samples that appear to be oversaturated with respect to ^{14}C [Borchers et al., 2016; Balco et al., 2016], which has been attributed to some combination of (i) unrecognized error in ^{14}C measurements or production-rate estimates and (ii) complex geologic scenarios [Balco et al., 2016]. Second, if the glacial deposits are indeed ^{14}C saturated, they are expected to have ^{10}Be exposure ages of at least ∼30 kyr (the exposure duration required to reach ^{14}C saturation), however they have ^{10}Be exposure ages of ∼18 and ∼14 kyr B.P. We have no reason to suspect unrecognized ^{10}Be error in these samples. Third, the glacial deposits have substantially higher ^{14}C concentrations than two of the three bedrock samples collected from higher elevations from weathered surfaces (Figure 4.19). Although these results could, in part, arise from underestimated ^{14}C production rates, it appears that there is unrecognized measurement error. One potential ^{14}C contaminant is laurylamine, a surfactant used on these samples for mineral separation. Although quartz separates were thoroughly etched in warm HF following laurylamine exposure, it may be possible that this was insufficient to purify the quartz.

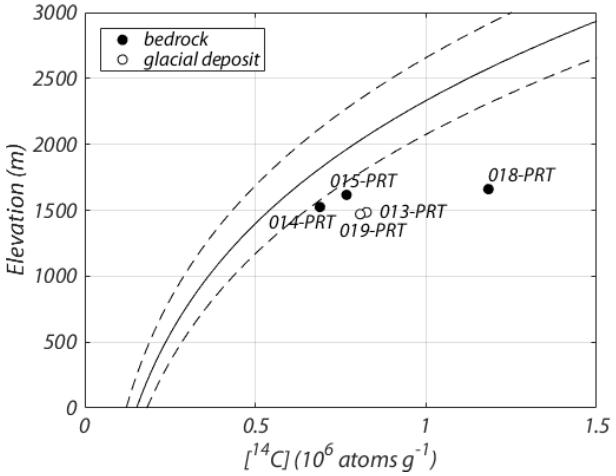

Figure 4.19: Plot of ^{14}C concentration as a function of elevation for samples from the Pirrit Hills. Solid black line represents saturation concentrations, and dashed lines represent 20% above and below saturation.

BIBLIOGRAPHY

R. P. Ackert, D. J. Barclay, H. W. Borns, P. E. Calkin, M. D. Kurz, J. L. Fastook, and E. J. Steig. Measurements of past ice sheet elevations in interior west antarctica. *Science*, 286 (5438):276–280, 1999.

R. P. Ackert, S. Mukhopadhyay, B. R. Parizek, and H. W. Borns. Ice elevation near the west antarctic ice sheet divide during the last glaciation. *Geophysical Research Letters*, 34(21), 2007.

R. P. Ackert Jr, S. Mukhopadhyay, D. Pollard, R. M. DeConto, A. E. Putnam, and H. W. Borns Jr. West antarctic ice sheet elevations in the ohio range: geologic constraints and ice sheet modeling prior to the last highstand. *Earth and Planetary Science Letters*, 307 (1-2):83–93, 2011.

R. Alley, D. Blankenship, S. Rooney, and C. Bentley. Sedimentation beneath ice shelvesthe view from ice stream b. *Marine Geology*, 85(2-4):101–120, 1989.

R. B. Alley, S. Anandakrishnan, K. Christianson, H. J. Horgan, A. Muto, B. R. Parizek, D. Pollard, and R. T. Walker. Oceanic forcing of ice-sheet retreat: West antarctica and more. *Annual Review of Earth and Planetary Sciences*, 43:207–231, 2015.

J. B. Anderson, S. Warny, R. A. Askin, J. S. Wellner, S. M. Bohaty, A. E. Kirshner, D. N. Livsey, A. R. Simms, T. R. Smith, W. Ehrmann, et al. Progressive cenozoic cooling and the demise of antarcticas last refugium. *Proceedings of the National Academy of Sciences*, 108(28):11356–11360, 2011.

J. B. Anderson, H. Conway, P. J. Bart, A. E. Witus, S. L. Greenwood, R. M. McKay, B. L. Hall, R. P. Ackert, K. Licht, M. Jakobsson, et al. Ross sea paleo-ice sheet drainage and deglacial history during and since the lgm. *Quaternary Science Reviews*, 100:31–54, 2014.

J. T. Andrews, E. W. Domack, W. L. Cunningham, A. Leventer, K. J. Licht, A. T. Jull, D. J. DeMaster, and A. E. Jennings. Problems and possible solutions concerning radiocarbon dating of surface marine sediments, ross sea, antarctica. *Quaternary Research*, 52(2): 206–216, 1999.

A. C. Ashworth and D. J. Cantrill. Neogene vegetation of the meyer desert formation (sirius group) transantarctic mountains, antarctica. *Palaeogeography, Palaeoclimatology, Palaeoecology*, 213(1-2):65–82, 2004.

A. C. Ashworth and T. L. Erwin. Antarctotrechus balli sp. n.(carabidae, trechini): the first ground beetle from antarctica. *ZooKeys*, (635):109, 2016.

G. Balco. Production rate calculations for cosmic-ray-muon-produced 10be and 26al benchmarked against geological calibration data. *Quaternary Geochronology*, 39:150–173, 2017.

G. Balco and D. L. Shuster. 26al–10be–21ne burial dating. *Earth and Planetary Science Letters*, 286(3-4):570–575, 2009a.

G. Balco and D. L. Shuster. Production rate of cosmogenic 21ne in quartz estimated from 10be, 26al, and 21ne concentrations in slowly eroding antarctic bedrock surfaces. *Earth and Planetary Science Letters*, 281(1-2):48–58, 2009b.

G. Balco, J. O. Stone, N. A. Lifton, and T. J. Dunai. A complete and easily accessible means of calculating surface exposure ages or erosion rates from 10be and 26al measurements. *Quaternary geochronology*, 3(3):174–195, 2008.

G. Balco, J. O. Stone, M. G. Sliwinski, and C. Todd. Features of the glacial history of the transantarctic mountains inferred from cosmogenic 26al, 10be and 21ne concentrations in bedrock surfaces. *Antarctic Science*, 26(06):708–723, 2014.

G. Balco, C. Todd, K. Huybers, S. Campbell, M. Vermeulen, M. Hegland, B. M. Goehring, and T. R. Hillebrand. Cosmogenic-nuclide exposure ages from the pensacola mountains adjacent to the foundation ice stream, antarctica. *American Journal of Science*, 316(6): 542–577, 2016.

J. L. Bamber, R. E. Riva, B. L. Vermeersen, and A. M. LeBrocq. Reassessment of the potential sea-level rise from a collapse of the west antarctic ice sheet. *Science*, 324(5929): 901–903, 2009.

D. K. Barnes and C.-D. Hillenbrand. Faunal evidence for a late quaternary trans-antarctic seaway. *Global Change Biology*, 16(12):3297–3303, 2010.

C. Baroni and B. L. Hall. A new holocene relative sea-level curve for terra nova bay, victoria land, antarctica. *Journal of Quaternary Science*, 19(4):377–396, 2004.

J. Behrendt, C. Finn, D. Morse, and D. Blankenship. One hundred negative magnetic anomalies over the west antarctic ice sheet (wais), in particular mt. resnik, a subaerially erupted volcanic peak, indicate eruption through at least one field reversal. *Antarctica: A Keystone in a Changing World–Online Proceedings of the 10tth ISAES, edited by AK Cooper and CR Raymond et al., USGS Open-File Report*, 1047, 2007.

J. C. Behrendt, D. D. Blankenship, C. A. Finn, R. E. Bell, R. E. Sweeney, S. M. Hodge, and J. M. Brozena. Casertz aeromagnetic data reveal late cenozoic flood basalts (?) in the west antarctic rift system. *Geology*, 22(6):527–530, 1994.

M. J. Bentley, C. J. Fogwill, A. M. Le Brocq, A. L. Hubbard, D. E. Sugden, T. J. Dunai, and S. P. Freeman. Deglacial history of the west antarctic ice sheet in the weddell sea embayment: Constraints on past ice volume change. *Geology*, 38(5):411–414, 2010.

M. J. Bentley, C. Ó. Cofaigh, J. B. Anderson, H. Conway, B. Davies, A. G. Graham, C.-D. Hillenbrand, D. A. Hodgson, S. S. Jamieson, R. D. Larter, et al. A community-based geological reconstruction of antarctic ice sheet deglaciation since the last glacial maximum. *Quaternary Science Reviews*, 100:1–9, 2014.

M. J. Bentley, A. Hein, D. Sugden, P. Whitehouse, R. Shanks, S. Xu, and S. Freeman. Deglacial history of the pensacola mountains, antarctica from glacial geomorphology and cosmogenic nuclide surface exposure dating. *Quaternary Science Reviews*, 158:58–76, 2017.

P. R. Bierman, L. B. Corbett, J. A. Graly, T. A. Neumann, A. Lini, B. T. Crosby, and D. H. Rood. Preservation of a preglacial landscape under the center of the greenland ice sheet. *Science*, 344(6182):402–405, 2014.

R. A. Bindschadler, E. P. Roberts, and A. Iken. Age of crary ice rise, antarctica, determined from temperature-depth profiles. *Annals of Glaciology*, 14:13–16, 1990.

R. G. Bingham and M. J. Siegert. Radar-derived bed roughness characterization of institute and möller ice streams, west antarctica, and comparison with siple coast ice streams. *Geophysical Research Letters*, 34(21), 2007.

R. Bintanja. On the glaciological, meteorological, and climatological significance of antarctic blue ice areas. *Reviews of Geophysics*, 37(3):337–359, 1999.

B. Borchers, S. Marrero, G. Balco, M. Caffee, B. Goehring, N. Lifton, K. Nishiizumi, F. Phillips, J. Schaefer, and J. Stone. Geological calibration of spallation production rates in the cronus-earth project. *Quaternary Geochronology*, 31:188–198, 2016.

S. L. Bradley, R. C. Hindmarsh, P. L. Whitehouse, M. J. Bentley, and M. A. King. Low post-glacial rebound rates in the weddell sea due to late holocene ice-sheet readvance. *Earth and Planetary Science Letters*, 413:79–89, 2015.

R. D. Briggs, D. Pollard, and L. Tarasov. A data-constrained large ensemble analysis of antarctic evolution since the eemian. *Quaternary Science Reviews*, 103:91–115, 2014.

G. R. Bromley, B. L. Hall, J. O. Stone, and H. Conway. Late pleistocene evolution of scott glacier, southern transantarctic mountains: implications for the antarctic contribution to deglacial sea level. *Quaternary Science Reviews*, 50:1–13, 2012.

C. Buizert, K. Cuffey, J. Severinghaus, D. Baggenstos, T. Fudge, E. Steig, B. Markle, M. Winstrup, R. Rhodes, E. Brook, et al. The wais divide deep ice core wd2014 chronology-part 1: Methane synchronization (68-31 ka bp) and the gas age-ice age difference. *Climate of the Past*, 11(2):153, 2015.

A. E. Carlson and P. U. Clark. Ice sheet sources of sea level rise and freshwater discharge during the last deglaciation. *Reviews of Geophysics*, 50(4), 2012.

P. U. Clark, J. Mitrovica, G. Milne, and M. Tamisiea. Sea-level fingerprinting as a direct test for the source of global meltwater pulse ia. *Science*, 295(5564):2438–2441, 2002.

H. Conway, B. Hall, G. Denton, A. Gades, and E. Waddington. Past and future grounding-line retreat of the west antarctic ice sheet. *Science*, 286(5438):280–283, 1999.

J. P. Craddock, M. D. Schmitz, J. L. Crowley, J. Larocque, R. J. Pankhurst, N. Juda, A. Konstantinou, and B. Storey. Precise u-pb zircon ages and geochemistry of jurassic granites, ellsworth-whitmore terrane, central antarctica. *Geological Society of America Bulletin*, pages B31485–1, 2016.

K. M. Cuffey, G. D. Clow, E. J. Steig, C. Buizert, T. Fudge, M. Koutnik, E. D. Waddington, R. B. Alley, and J. P. Severinghaus. Deglacial temperature history of west antarctica. *Proceedings of the National Academy of Sciences*, 113(50):14249–14254, 2016.

B. de Boer, A. Dolan, J. Bernales, E. Gasson, N. Golledge, J. Sutter, P. Huybrechts, G. Lohmann, I. Rogozhina, A. Abe-Ouchi, et al. Simulating the antarctic ice sheet in the late-pliocene warm period: Plismip-ant, an ice-sheet model intercomparison project. *The Cryosphere*, 9:881–903, 2015.

R. M. DeConto and D. Pollard. Contribution of antarctica to past and future sea-level rise. *Nature*, 531(7596):591–597, 2016.

G. H. Denton, J. G. Bockheim, R. H. Rutford, and B. G. Andersen. Glacial history of the ellsworth mountains, west antarctica. *Geological Society of America Memoirs*, 170: 403–432, 1992.

G. H. Denton, D. E. Sugden, D. R. Marchant, B. L. Hall, and T. I. Wilch. East antarctic ice sheet sensitivity to pliocene climatic change from a dry valleys perspective. *Geografiska Annaler: Series A, Physical Geography*, 75(4):155–204, 1993.

P. Deschamps, N. Durand, E. Bard, B. Hamelin, G. Camoin, A. L. Thomas, G. M. Henderson, J. Okuno, and Y. Yokoyama. Ice-sheet collapse and sea-level rise at the bølling warming 14,600 years ago. *Nature*, 483(7391):559, 2012.

R. G. Ditchburn and N. E. Whitehead. The separation of 10be from silicates. In G. Hancock and P. Wallbrink, editors, *Third Workshop of the South Pacific Environmental Radioactivity Association*, pages 4–7. Australian National University, Canberra, 1994.

H. Dowsett, M. Robinson, A. Haywood, U. Salzmann, D. Hill, L. Sohl, M. Chandler, M. Williams, K. Foley, and D. Stoll. The prism3d paleoenvironmental reconstruction. *Stratigraphy*, 7(2-3):123–139, 2010.

H. Dowsett, A. Dolan, D. Rowley, R. Moucha, A. Forte, J. Mitrovica, M. Pound, U. Salzmann, M. Robinson, M. Chandler, et al. The prism4 (mid-piacenzian) paleoenvironmental reconstruction, 2016.

N. W. Dunbar, W. C. McIntosh, and R. P. Esser. Physical setting and tephrochronology of the summit caldera ice record at mount moulton, west antarctica. *Geological Society of America Bulletin*, 120(7-8):796–812, 2008.

A. Dutton, A. Carlson, A. Long, G. Milne, P. Clark, R. DeConto, B. Horton, S. Rahmstorf, and M. Raymo. Sea-level rise due to polar ice-sheet mass loss during past warm periods. *Science*, 349(6244):aaa4019, 2015.

G. L. Farmer, K. Licht, R. J. Swope, and J. Andrews. Isotopic constraints on the provenance of fine-grained sediment in lgm tills from the ross embayment, antarctica. *Earth and Planetary Science Letters*, 249(1-2):90–107, 2006.

L. Favier, G. Durand, S. L. Cornford, G. H. Gudmundsson, O. Gagliardini, F. Gillet-Chaulet, T. Zwinger, A. Payne, and A. M. Le Brocq. Retreat of pine island glacier controlled by marine ice-sheet instability. *Nature Climate Change*, 4(2):117–121, 2014.

J. Feldmann and A. Levermann. Collapse of the west antarctic ice sheet after local destabilization of the amundsen basin. *Proceedings of the National Academy of Sciences*, 112 (46):14191–14196, 2015.

D. Fernandez-Mosquera, D. Hahm, and K. Marti. Calculated rates of cosmic ray muon-produced ne in subsurface quartz. *Geophysical Research Letters*, 37(15), 2010.

P. Fretwell, H. D. Pritchard, D. G. Vaughan, J. Bamber, N. Barrand, R. Bell, C. Bianchi, R. Bingham, D. Blankenship, G. Casassa, et al. Bedmap2: improved ice bed, surface and thickness datasets for antarctica. *The Cryosphere*, 7(1), 2013.

T. Fudge, B. R. Markle, K. M. Cuffey, C. Buizert, K. C. Taylor, E. J. Steig, E. D. Waddington, H. Conway, and M. Koutnik. Variable relationship between accumulation and temperature in west antarctica for the past 31,000 years. *Geophysical Research Letters*, 43(8): 3795–3803, 2016.

N. R. Golledge, C. J. Fogwill, A. N. Mackintosh, and K. M. Buckley. Dynamics of the last glacial maximum antarctic ice-sheet and its response to ocean forcing. *Proceedings of the National Academy of Sciences*, 109(40):16052–16056, 2012.

N. R. Golledge, Z. A. Thomas, R. H. Levy, E. G. Gasson, T. R. Naish, R. M. McKay, D. E. Kowalewski, and C. J. Fogwill. Antarctic climate and ice-sheet configuration during the early pliocene interglacial at 4.23 ma. *Climate of the Past*, 13(7):959, 2017.

J. W. Goodge and J. P. Severinghaus. Rapid access ice drill: a new tool for exploration of the deep antarctic ice sheets and subglacial geology. *Journal of Glaciology*, 62(236): 1049–1064, 2016.

A. R. W. Halberstadt, L. M. Simkins, S. L. Greenwood, and J. B. Anderson. Past ice-sheet behaviour: Retreat scenarios and changing controls in the ross sea, antarctica. *The Cryosphere*, 10(3):1003, 2016.

B. L. Hall and G. H. Denton. Radiocarbon chronology of ross sea drift, eastern taylor valley, antarctica: Evidence for a grounded ice sheet in the ross sea at the last glacial maximum. *Geografiska Annaler: Series A, Physical Geography*, 82(2-3):305–336, 2000.

B. L. Hall, C. Baroni, and G. H. Denton. Holocene relative sea-level history of the southern victoria land coast, antarctica. *Global and Planetary Change*, 42(1-4):241–263, 2004.

B. L. Hall, G. M. Henderson, C. Baroni, and T. B. Kellogg. Constant holocene southern-ocean 14c reservoir ages and ice-shelf flow rates. *Earth and Planetary Science Letters*, 296 (1-2):115–123, 2010.

T. Haran, J. Bohlander, T. Scambos, T. Painter, and M. Fahnestock. Measures modis mosaic of greenland 2005 (mog2005) image map, version 1. boulder, colorado. nsidc: National snow and ice data center, 2013.

A. Haywood, D. Hill, A. Dolan, B. Otto-Bliesner, F. Bragg, W.-L. Chan, M. Chandler, C. Contoux, H. Dowsett, A. Jost, et al. Large-scale features of pliocene climate: results from the pliocene model intercomparison project. *Climate of the Past*, 9(1):191, 2013.

A. M. Haywood, H. J. Dowsett, P. J. Valdes, D. J. Lunt, J. E. Francis, and B. W. Sellwood. Ipliocene climate, processes and problems. *Philosophical Transactions of the Royal Society of London A: Mathematical, Physical and Engineering Sciences*, 367(1886):3–17, 2009.

A. S. Hein, S. M. Marrero, J. Woodward, S. A. Dunning, K. Winter, M. J. Westoby, S. P. Freeman, R. P. Shanks, and D. E. Sugden. Mid-holocene pulse of thinning in the weddell sea sector of the west antarctic ice sheet. *Nature communications*, 7:12511, 2016.

B. Heisinger, D. Lal, A. Jull, P. Kubik, S. Ivy-Ochs, K. Knie, and E. Nolte. Production of selected cosmogenic radionuclides by muons: 2. capture of negative muons. *Earth and Planetary Science Letters*, 200(3):357–369, 2002a.

B. Heisinger, D. Lal, A. Jull, P. Kubik, S. Ivy-Ochs, S. Neumaier, K. Knie, V. Lazarev, and E. Nolte. Production of selected cosmogenic radionuclides by muons: 1. fast muons. *Earth and Planetary Science Letters*, 200(3):345–355, 2002b.

M. M. Herron and C. C. Langway. Firn densification: an empirical model. *Journal of glaciology*, 25(93):373–385, 1980.

S. S. Jamieson, D. E. Sugden, and N. R. Hulton. The evolution of the subglacial landscape of antarctica. *Earth and Planetary Science Letters*, 293(1):1–27, 2010.

J. S. Johnson, M. J. Bentley, and K. Gohl. First exposure ages from the amundsen sea embayment, west antarctica: The late quaternary context for recent thinning of pine island, smith, and pope glaciers. *Geology*, 36(3):223–226, 2008.

R. Jones, A. Mackintosh, K. Norton, N. Golledge, C. Fogwill, P. Kubik, M. Christl, and S. L. Greenwood. Rapid holocene thinning of an east antarctic outlet glacier driven by marine ice sheet instability. *Nature communications*, 6, 2015.

T. A. Jordan, F. Ferraccioli, N. Ross, H. F. Corr, P. T. Leat, R. G. Bingham, D. M. Rippin, A. le Brocq, and M. J. Siegert. Inland extent of the weddell sea rift imaged by new aerogeophysical data. *Tectonophysics*, 585:137–160, 2013.

I. Joughin, B. E. Smith, and B. Medley. Marine ice sheet collapse potentially under way for the thwaites glacier basin, west antarctica. *Science*, 344(6185):735–738, 2014.

A. T. Jull, E. M. Scott, and P. Bierman. The cronus-earth inter-comparison for cosmogenic isotope analysis. *Quaternary Geochronology*, 26:3–10, 2015.

T. B. Kellogg, D. E. Kellogg, and M. Stuiver. Late quaternary history of the southwestern ross sea: evidence from debris bands on the mcmurdo ice shelf, antarctica. *Contributions to Antarctic research I*, pages 25–56, 1990.

N. S. Khan, E. Ashe, T. A. Shaw, M. Vacchi, J. Walker, W. Peltier, R. E. Kopp, and B. P. Horton. Holocene relative sea-level changes from near-, intermediate-, and far-field locations. *Current Climate Change Reports*, 1(4):247–262, 2015.

J. Kingslake, R. Scherer, T. Albrecht, J. J. Coenen, R. Powell, R. Reese, N. Stansell, S. Tulaczyk, and P. Whitehouse. Extensive holocene ice sheet grounding line retreat and uplift-driven readvance in west antarctica. In *American Geophysical Union*, pages Abstract C11E–01, 2017.

J. Klein, R. Giegengack, R. Middleton, P. Sharma, J. Underwood, and R. Weeks. Revealing histories of exposure using in situ produced 26 al and 10 be in libyan desert glass. *Radiocarbon*, 28(2A):547–555, 1986.

C. Kohl and K. Nishiizumi. Chemical isolation of quartz for measurement of in-situ-produced cosmogenic nuclides. *Geochimica et Cosmochimica Acta*, 56(9):3583–3587, 1992.

E. V. Korotkikh, P. A. Mayewski, M. J. Handley, S. B. Sneed, D. S. Introne, A. V. Kurbatov, N. W. Dunbar, and W. C. McIntosh. The last interglacial as represented in the glaciochemical record from mount moulton blue ice area, west antarctica. *Quaternary Science Reviews*, 30(15):1940–1947, 2011.

A. Kovacs, A. J. Gow, and R. M. Morey. The in-situ dielectric constant of polar firn revisited. *Cold Regions Science and Technology*, 23(3):245–256, 1995.

C. Laj, C. Kissel, and J. Beer. High resolution global paleointensity stack since 75 kyr (glopis-75) calibrated to absolute values. *Timescales of the Paleomagnetic Field*, pages 255–265, 2004.

D. Lal. Cosmic ray labeling of erosion surfaces: in situ nuclide production rates and erosion models. *Earth and Planetary Science Letters*, 104(2-4):424–439, 1991.

D. Lal and J. Arnold. Tracing quartz through the environment. *Proceedings of the Indian Academy of Sciences-Earth and Planetary Sciences*, 94(1):1–5, 1985.

K. Lambeck, H. Rouby, A. Purcell, Y. Sun, and M. Sambridge. Sea level and global ice volumes from the last glacial maximum to the holocene. *Proceedings of the National Academy of Sciences*, 111(43):15296–15303, 2014.

J. Laskar, P. Robutel, F. Joutel, M. Gastineau, A. Correia, and B. Levrard. A long-term numerical solution for the insolation quantities of the earth. *Astronomy & Astrophysics*, 428(1):261–285, 2004.

J. I. Lee, R. M. McKay, N. R. Golledge, H. I. Yoon, K.-C. Yoo, H. J. Kim, and J. K. Hong. Widespread persistence of expanded east antarctic glaciers in the southwest ross sea during the last deglaciation. *Geology*, 45(5):403–406, 2017.

A. Lewis, D. Marchant, A. Ashworth, S. Hemming, and M. Machlus. Major middle miocene global climate change: Evidence from east antarctica and the transantarctic mountains. *Geological Society of America Bulletin*, 119(11-12):1449–1461, 2007.

A. R. Lewis, D. R. Marchant, A. C. Ashworth, L. Hedenäs, S. R. Hemming, J. V. Johnson, M. J. Leng, M. L. Machlus, A. E. Newton, J. I. Raine, et al. Mid-miocene cooling and the extinction of tundra in continental antarctica. *Proceedings of the National Academy of Sciences*, 105(31):10676–10680, 2008.

K. J. Licht. The ross sea's contribution to eustatic sea level during meltwater pulse 1a. *Sedimentary Geology*, 165(3-4):343–353, 2004.

K. J. Licht, A. E. Jennings, J. T. Andrews, and K. M. Williams. Chronology of late wisconsin ice retreat from the western ross sea, antarctica. *Geology*, 24(3):223–226, 1996.

K. J. Licht, J. R. Lederer, and R. J. Swope. Provenance of lgm glacial till (sand fraction) across the ross embayment, antarctica. *Quaternary Science Reviews*, 24(12-13):1499–1520, 2005.

K. J. Licht, A. J. Hennessy, and B. M. Welke. The u-pb detrital zircon signature of west antarctic ice stream tills in the ross embayment, with implications for last glacial maximum ice flow reconstructions. *Antarctic Science*, 26(6):687–697, 2014.

N. Lifton, T. Sato, and T. J. Dunai. Scaling in situ cosmogenic nuclide production rates using analytical approximations to atmospheric cosmic-ray fluxes. *Earth and Planetary Science Letters*, 386:149–160, 2014.

N. A. Lifton, A. T. Jull, and J. Quade. A new extraction technique and production rate estimate for in situ cosmogenic 14c in quartz. *Geochimica et Cosmochimica Acta*, 65(12): 1953–1969, 2001.

K. Lilly, D. Fink, D. Fabel, and K. Lambeck. Pleistocene dynamics of the interior east antarctic ice sheet. *Geology*, 38(8):703–706, 2010.

L. E. Lisiecki and M. E. Raymo. A pliocene-pleistocene stack of 57 globally distributed benthic δ18o records. *Paleoceanography*, 20(1), 2005.

H. Liu, K. Jezek, B. Li, and Z. Zhao. Radarsat antarctic mapping project digital elevation model version 2. *Radarsat Antarctic Mapping Project digital elevation model version 2, Boulder, Colorado USA: National Snow and Ice Data Center. Digital media.*, 2001.

J. Liu, G. A. Milne, R. E. Kopp, P. U. Clark, and I. Shennan. Sea-level constraints on the amplitude and source distribution of meltwater pulse 1a. *Nature Geoscience*, 9(2):130, 2016.

D. Marchant, S. Mackay, J. Lamp, A. Hayden, and J. Head. A review of geomorphic processes and landforms in the dry valleys of southern victoria land: implications for evaluating climate change and ice-sheet stability. *Geological Society, London, Special Publications*, 381(1):319–352, 2013.

D. R. Marchant and G. H. Denton. Miocene and pliocene paleoclimate of the dry valleys region, southern victoria land: a geomorphological approach. *Marine Micropaleontology*, 27(1-4):253–271, 1996.

C. Martín, R. C. Hindmarsh, and F. J. Navarro. Dating ice flow change near the flow divide at roosevelt island, antarctica, by using a thermomechanical model to predict radar stratigraphy. *Journal of Geophysical Research: Earth Surface*, 111(F1), 2006.

K. Matsuoka, R. C. Hindmarsh, G. Moholdt, M. J. Bentley, H. D. Pritchard, J. Brown, H. Conway, R. Drews, G. Durand, D. Goldberg, et al. Antarctic ice rises and rumples: Their properties and significance for ice-sheet dynamics and evolution. *Earth-science reviews*, 150:724–745, 2015.

R. McKay, N. R. Golledge, S. Maas, T. Naish, R. Levy, G. Dunbar, and G. Kuhn. Antarctic marine ice-sheet retreat in the ross sea during the early holocene. *Geology*, 44(1):7–10, 2016.

J. H. Mercer. Glacial geology of the reedy glacier area, antarctica. *Geological Society of America Bulletin*, 79(4):471–486, 1968.

K. G. Miller, J. D. Wright, J. V. Browning, A. Kulpecz, M. Kominz, T. R. Naish, B. S. Cramer, Y. Rosenthal, W. R. Peltier, and S. Sosdian. High tide of the warm pliocene: Implications of global sea level for antarctic deglaciation. *Geology*, 40(5):407–410, 2012.

D. L. Morse, D. D. Blankenship, E. D. Waddington, and T. A. Neumann. A site for deep ice coring in west antarctica: results from aerogeophysical surveys and thermo-kinematic modeling. *Annals of Glaciology*, 35(1):36–44, 2002.

B. Mouginot, B. Scheuchl, and E. Rignot. Measures antarctic boundaries for ipy 2007–2009 from satellite radar, version 2. *Boulder, CO: NASA National Snow and Ice Data Center Distributed Active Archive Center. https://doi. org/10.5067/AXE4121732AD*, 2017.

S. Mukhopadhyay, R. P. Ackert, A. E. Pope, D. Pollard, and R. M. DeConto. Miocene to recent ice elevation variations from the interior of the west antarctic ice sheet: Constraints from geologic observations, cosmogenic nuclides and ice sheet modeling. *Earth and Planetary Science Letters*, 337:243–251, 2012.

R. Mulvaney, J. Triest, and O. Alemany. The james ross island and the fletcher promontory ice-core drilling projects. *Annals of Glaciology*, 55(68):179–188, 2014.

T. Naish, R. Powell, R. Levy, G. Wilson, R. Scherer, F. Talarico, L. Krissek, F. Niessen, M. Pompilio, T. Wilson, et al. Obliquity-paced pliocene west antarctic ice sheet oscillations. *Nature*, 458(7236):322, 2009.

NEEM community members. Eemian interglacial reconstructed from a greenland folded ice core. *Nature*, 493(7433):489–494, 2013.

S. Niedermann, T. Graf, and K. Marti. Mass spectrometric identification of cosmic-ray-produced neon in terrestrial rocks with multiple neon components. *Earth and Planetary Science Letters*, 118(1-4):65–73, 1993.

K. Nishiizumi. Preparation of 26al ams standards. *Nuclear Instruments and Methods in Physics Research Section B: Beam Interactions with Materials and Atoms*, 223:388–392, 2004.

K. Nishiizumi, M. Imamura, M. W. Caffee, J. R. Southon, R. C. Finkel, and J. McAninch. Absolute calibration of 10be ams standards. *Nuclear Instruments and Methods in Physics Research Section B: Beam Interactions with Materials and Atoms*, 258(2):403–413, 2007.

K. e. a. Nishiizumi. In situ produced cosmogenic nuclides in gisp2 rock core from greenland summit. In *Eos, Transactions of the American Geophysical Union*, pages Abstract OS41B–10==, 1996.

B. R. Parizek and R. B. Alley. Ice thickness and isostatic imbalances in the ross embayment, west antarctica: model results. *Global and Planetary Change*, 42(1-4):265–278, 2004.

F. Parrenin, G. Dreyfus, G. Durand, S. Fujita, O. Gagliardini, F. Gillet, J. Jouzel, K. Kawamura, N. Lhomme, V. Masson-Delmotte, et al. 1-d-ice flow modelling at epica dome c and dome fuji, east antarctica. *Climate of the Past*, 3(2):243–259, 2007.

F. J. Pavón-Carrasco, M. L. Osete, J. M. Torta, and A. De Santis. A geomagnetic field model for the holocene based on archaeomagnetic and lava flow data. *Earth and Planetary Science Letters*, 388:98–109, 2014.

A. J. Payne, A. Vieli, A. P. Shepherd, D. J. Wingham, and E. Rignot. Recent dramatic thinning of largest west antarctic ice stream triggered by oceans. *Geophysical Research Letters*, 31(23), 2004.

W. Peltier. Global glacial isostasy and the surface of the ice-age earth: the ice-5g (vm2) model and grace. *Annu. Rev. Earth Planet. Sci.*, 32:111–149, 2004.

W. Peltier, D. Argus, and R. Drummond. Space geodesy constrains ice age terminal deglaciation: The global ice-6g_c (vm5a) model. *Journal of Geophysical Research: Solid Earth*, 120(1):450–487, 2015.

J. S. Pigati. Experimental developments and application of carbon-14 and in situ cosmogenic nuclide dating techniques. 2004.

Z. Ploskey and J. Stone. Cosmogenic nuclide depth profiles as a signal of pleistocene glacial erosion. In *AGU Fall Meeting Abstracts*, 2012.

D. Pollard and R. DeConto. Description of a hybrid ice sheet-shelf model, and application to antarctica. *Geoscientific Model Development*, 5(5):1273, 2012a.

D. Pollard and R. DeConto. A simple inverse method for the distribution of basal sliding coefficients under ice sheets, applied to antarctica. *The Cryosphere*, 6(5):953, 2012b.

D. Pollard and R. M. DeConto. Modelling west antarctic ice sheet growth and collapse through the past five million years. *Nature*, 458(7236):329–332, 2009.

D. Pollard, R. M. DeConto, and R. B. Alley. Potential antarctic ice sheet retreat driven by hydrofracturing and ice cliff failure. *Earth and Planetary Science Letters*, 412:112–121, 2015.

D. Pollard, W. Chang, M. Haran, P. Applegate, and R. DeConto. Large ensemble modeling of the last deglacial retreat of the west antarctic ice sheet: comparison of simple and advanced statistical techniques. *Geoscientific Model Development*, 9(5), 2016.

E. W. Portenga and P. R. Bierman. Understanding earths eroding surface with 10 be. *GsA today*, 21(8):4–10, 2011.

S. Price, H. Conway, and E. Waddington. Evidence for late pleistocene thinning of siple dome, west antarctica. *Journal of Geophysical Research: Earth Surface*, 112(F3), 2007.

H. Pritchard, S. Ligtenberg, H. Fricker, D. Vaughan, M. Van den Broeke, and L. Padman. Antarctic ice-sheet loss driven by basal melting of ice shelves. *Nature*, 484(7395):502, 2012.

M. E. Raymo, R. Kozdon, D. Evans, L. Lisiecki, and H. L. Ford. The accuracy of mid-pliocene δ 18 o-based ice volume and sea level reconstructions. *Earth-Science Reviews*, 2017.

P. J. Reimer, E. Bard, A. Bayliss, J. W. Beck, P. G. Blackwell, C. B. Ramsey, C. E. Buck, H. Cheng, R. L. Edwards, M. Friedrich, et al. Intcal13 and marine13 radiocarbon age calibration curves 0–50,000 years cal bp. *Radiocarbon*, 55(4):1869–1887, 2013.

E. Rignot, J. Mouginot, and B. Scheuchl. Ice flow of the antarctic ice sheet. *Science*, 333 (6048):1427–1430, 2011.

E. Rignot, J. Mouginot, M. Morlighem, H. Seroussi, and B. Scheuchl. Widespread, rapid grounding line retreat of pine island, thwaites, smith, and kohler glaciers, west antarctica, from 1992 to 2011. *Geophysical Research Letters*, 41(10):3502–3509, 2014.

R. Rutford and W. McIntosh. Jones mountains, antarctica: evidence for tertiary glaciation revisited. *Antarctica: a keystone in a changing world. Online Proceedings of the 10th ISAES, United States Geological Survey Open-File Report*, 1047, 2007.

T. Scambos, R. Bell, R. Alley, S. Anandakrishnan, D. Bromwich, K. Brunt, K. Christianson, T. Creyts, S. Das, R. DeConto, et al. How much, how fast?: A science review and outlook for research on the instability of antarctica's thwaites glacier in the 21st century. *Global and Planetary Change*, 2017.

J. M. Schaefer, R. C. Finkel, G. , R. B. Alley, M. W. Caffee, J. P. Briner, N. E. Young, A. J. Gow, and R. Schwartz. Greenland was nearly ice-free for extended periods during the pleistocene. *Nature*, 540(7632):252–255, 2016.

J. M. Schäfer, S. Ivy-Ochs, R. Wieler, I. Leya, H. Baur, G. H. Denton, and C. Schlüchter. Cosmogenic noble gas studies in the oldest landscape on earth: surface exposure ages of the dry valleys, antarctica. *Earth and Planetary Science Letters*, 167(3):215–226, 1999.

R. P. Scherer, A. Aldahan, S. Tulaczyk, G. Possnert, H. Engelhardt, and B. Kamb. Pleistocene collapse of the west antarctic ice sheet. *Science*, 281(5373):82–85, 1998.

R. P. Scherer, R. M. DeConto, D. Pollard, and R. B. Alley. Windblown pliocene diatoms and east antarctic ice sheet retreat. *Nature communications*, 7:12957, 2016.

C. Schoof. Ice sheet grounding line dynamics: Steady states, stability, and hysteresis. *Journal of Geophysical Research: Earth Surface*, 112(F3), 2007.

A. E. Shevenell, J. P. Kennett, and D. W. Lea. Middle miocene southern ocean cooling and antarctic cryosphere expansion. *Science*, 305(5691):1766–1770, 2004.

M. Siegert, N. Ross, H. Corr, J. Kingslake, and R. Hindmarsh. Late holocene ice-flow reconfiguration in the weddell sea sector of west antarctica. *Quaternary Science Reviews*, 78:98–107, 2013.

R. Souchez, J. Jouzel, A. Landais, J. Chappellaz, R. Lorrain, and J.-L. Tison. Gas isotopes in ice reveal a vegetated central greenland during ice sheet invasion. *Geophysical research letters*, 33(24), 2006.

P. Spector, J. Stone, S. G. Cowdery, B. Hall, H. Conway, and G. Bromley. Rapid early-holocene deglaciation in the ross sea, antarctica. *Geophysical Research Letters*, 44(15): 7817–7825, 2017.

C. Spiegel, J. Lindow, P. J. Kamp, O. Meisel, S. Mukasa, F. Lisker, G. Kuhn, and K. Gohl. Tectonomorphic evolution of marie byrd land–implications for cenozoic rifting activity and onset of west antarctic glaciation. *Global and Planetary Change*, 145:98–115, 2016.

E. J. Steig, J. L. Fastook, C. Zweck, I. D. Goodwin, K. J. Licht, J. W. White, and R. P. Ackert. West antarctic ice sheet elevation changes. *The West Antarctic Ice Sheet: Behavior and Environment*, pages 75–90, 2001.

J. O. Stone. Air pressure and cosmogenic isotope production. *Journal of Geophysical Research: Solid Earth*, 105(B10):23753–23759, 2000.

J. O. Stone, G. A. Balco, D. E. Sugden, M. W. Caffee, L. C. Sass, S. G. Cowdery, and C. Siddoway. Holocene deglaciation of marie byrd land, west antarctica. *Science*, 299 (5603):99–102, 2003.

B. Storey and I. Dalziel. Outline of the structural and tectonic history of the ellsworth mountains-thiel mountains ridge, west antarctica. *Gondwana six: structure, tectonics, and geophysics*, pages 117–128, 1987.

G. Stuhne and W. Peltier. Reconciling the ice-6g_c reconstruction of glacial chronology with ice sheet dynamics: The cases of greenland and antarctica. *Journal of Geophysical Research: Earth Surface*, 120(9):1841–1865, 2015.

M. Stuiver. History of the marine ice sheet in west antarctica during the last glaciation: a working hypothesis. *The last great ice sheets*, pages 319–436, 1981.

D. E. Sugden, M. A. Summerfield, G. H. Denton, T. I. Wilch, W. C. McIntosh, D. R. Marchant, and R. H. Rutford. Landscape development in the royal society range, southern victoria land, antarctica: stability since the mid-miocene. *Geomorphology*, 28(3-4):181–200, 1999.

D. E. Sugden, G. Balco, S. G. Cowdery, J. O. Stone, and L. C. Sass. Selective glacial erosion and weathering zones in the coastal mountains of marie byrd land, antarctica. *Geomorphology*, 67(3):317–334, 2005.

D. E. Sugden, A. S. Hein, J. Woodward, S. M. Marrero, Á. Rodés, S. A. Dunning, F. M. Stuart, S. P. Freeman, K. Winter, and M. J. Westoby. The million-year evolution of the glacial trimline in the southernmost ellsworth mountains, antarctica. *Earth and Planetary Science Letters*, 469:42–52, 2017.

C. Todd, J. Stone, H. Conway, B. Hall, and G. Bromley. Late quaternary evolution of reedy glacier, antarctica. *Quaternary Science Reviews*, 29(11):1328–1341, 2010.

P. Vermeesch, G. Balco, P.-H. Blard, T. J. Dunai, F. Kober, S. Niedermann, D. L. Shuster, S. Strasky, F. M. Stuart, R. Wieler, et al. Interlaboratory comparison of cosmogenic 21ne in quartz. *Quaternary Geochronology*, 26:20–28, 2015.

E. Waddington, H. Conway, E. Steig, R. Alley, E. Brook, K. Taylor, and J. White. Decoding the dipstick: thickness of siple dome, west antarctica, at the last glacial maximum. *Geology*, 33(4):281–284, 2005.

S. Warny, R. A. Askin, M. J. Hannah, B. A. Mohr, J. I. Raine, D. M. Harwood, F. Florindo, and S. S. Team. Palynomorphs from a sediment core reveal a sudden remarkably warm antarctica during the middle miocene. *Geology*, 37(10):955–958, 2009.

P. N. Webb, T. E. Ronan, J. H. Lipps, and T. E. DeLaca. Miocene glaciomarine sediments from beneath the southern ross ice shelf, antarctica. *Science*, 203(4379):435–437, 1979.

G. Webers, C. Craddock, M. A. Rogers, and J. Anderson. Geology of the whitmore mountains. In C. Craddock, editor, *Antarctic Geoscience*, pages 841–847. University of Wisconsin Press, Madison, 1982.

J. Weertman. Stability of the junction of an ice sheet and an ice shelf. *Journal of Glaciology*, 13(67):3–11, 1974.

L. Wei, J. Raine, and X. Liu. Terrestrial palynomorphs of the cenozoic pagodroma group, northern prince charles mountains, east antarctica. *Antarctic Science*, 26(1):69–79, 2014.

P. L. Whitehouse, M. J. Bentley, and A. M. Le Brocq. A deglacial model for antarctica: geological constraints and glaciological modelling as a basis for a new model of antarctic glacial isostatic adjustment. *Quaternary Science Reviews*, 32:1–24, 2012.

T. I. Wilch, W. McIntosh, and N. Dunbar. Late quaternary volcanic activity in marie byrd land: Potential 40ar/39ar-dated time horizons in west antarctic ice and marine cores. *GSA Bulletin*, 111(10):1563–1580, 1999.

E. Willerslev, E. Cappellini, W. Boomsma, R. Nielsen, M. B. Hebsgaard, T. B. Brand, M. Hofreiter, M. Bunce, H. N. Poinar, D. Dahl-Jensen, et al. Ancient biomolecules from deep ice cores reveal a forested southern greenland. *Science*, 317(5834):111–114, 2007.

K. Winter, J. Woodward, N. Ross, S. A. Dunning, R. G. Bingham, H. F. Corr, and M. J. Siegert. Airborne radar evidence for tributary flow switching in institute ice stream, west antarctica: Implications for ice sheet configuration and dynamics. *Journal of Geophysical Research: Earth Surface*, 120(9):1611–1625, 2015.

N. E. Young, J. M. Schaefer, B. Goehring, N. Lifton, I. Schimmelpfennig, and J. P. Briner. West greenland and global in situ 14c production-rate calibrations. *Journal of Quaternary Science*, 29(5):401–406, 2014.

J. Zachos, M. Pagani, L. Sloan, E. Thomas, and K. Billups. Trends, rhythms, and aberrations in global climate 65 ma to present. *Science*, 292(5517):686–693, 2001.

L. Ziegler, C. Constable, C. Johnson, and L. Tauxe. Padm2m: a penalized maximum likelihood model of the 0–2 ma palaeomagnetic axial dipole moment. *Geophysical Journal International*, 184(3):1069–1089, 2011.